CHALMERS
UNIVERSITY OF TECHNOLOGY

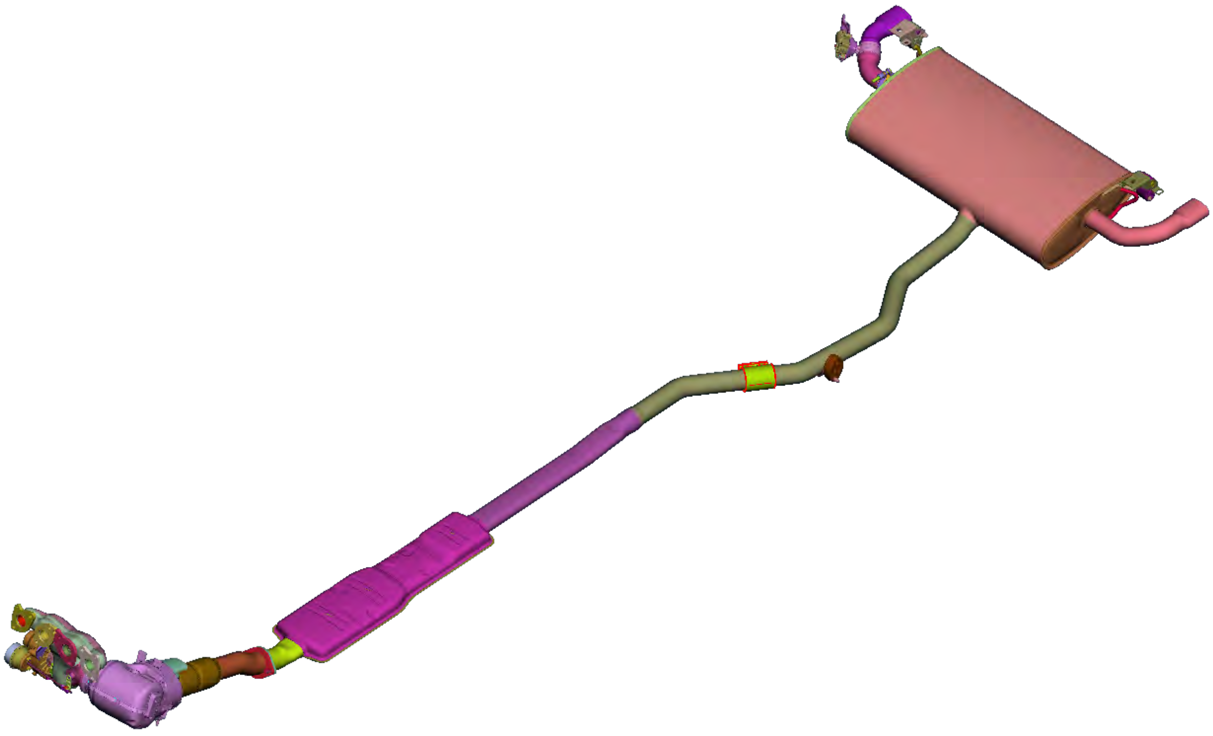

Modelling of breakout noise from automotive mufflers

Master's thesis in Sound and Vibration

DAYASAGAR VALADY SRINIVASAN

Division of Applied Acoustics
Department of Civil and Environmental Engineering
Chalmers University of Technology
Göteborg, Sweden 2016

Master's thesis 2016:BOMX02-16-120

Modelling of breakout noise from automotive mufflers

DAYASAGAR VALADY SRINIVASAN

Department of Civil and Environmental Engineering
Division of Applied Acoustics
Chalmers University of Technology
Göteborg, Sweden 2016

Modelling of breakout noise from automotive mufflers
DAYASAGAR VALADY SRINIVASAN

Supervisor: David Beskow(VCC), Dr. Magnus Knutsson(VCC), Jan Larsson(VCC), Dr. Carsten Hoever(Division of Applied Acoustics, Chalmers)
Examiner: Docent. Patrik Höstmad (Division of Applied Acoustics, Chalmers)

Master's Thesis 2016:BOMX02-16-120
Department of Civil and Environmental Engineering
Division of Applied Acoustics
Chalmers University of Technology
SE-412 96 Gothenburg
Telephone +46 31 772 2200

Cover: Complete exhaust muffler assembly.

Typeset in LaTeX
Printed by Chalmers Reproservice
Gothenburg, Sweden 2016

MODELLING OF BREAKOUT NOISE FROM AUTOMOTIVE MUFFLERS

DAYASAGAR VALADY SRINIVASAN
Department of Civil and Environmental Engineering
Division of Applied Acoustics
Chalmers University of Technology

ABSTRACT

Silencers are used to attenuate the low frequency pressure pulsations that are a result of the gas exchange process in IC-engines in passenger cars. Broad frequency band attenuation can be achieved from a combination of reactive and resistive countermeasures. An undesirable side effect from large silencers is that the shell structure of the silencer can radiate noise. The purpose of this thesis is develop models to simulate this phenomenon, also called breakout noise. The present study aims to develop an acoustic-structure FE model, that includes how an incoming sound wave is transmitted inside the air cavity of a mass produced muffler, transmitted through the shell structure and thereafter radiated into a reflection free environment. Of particular interest is the influence of the connection of the internal baffles to the outer shell and the influence of a temperature field on the system. This FE model ultimately aims to accurately model the physics so as to be used for future vibroacoustic analyses involving the muffler. An FE model that takes into account the temperature dependent coupling conditions is designed. An experimental validation is also conducted and includes measurements in anechoic chamber at cold conditions with loudspeaker excitation as well as measurements in an engine test cell and chassis dynamometer. The thesis work has been successful in assessing the influence of both the baffle-outer shell connections as well as an elevated temperature field.

Keywords: breakout noise, vibroacoustics, automotive mufflers, FE modelling.

Acknowledgements

Firstly, I would like to thank David Beskow at Volvo Car Corporation (VCC) for being a very approachable and knowledgeable supervisor who was always available and ready to discuss my results and sort out my queries. I am indebted to Dr. Magnus Knutsson and Jan Larsson for giving me the opportunity to perform my thesis at VCC, closely overseeing its progress and guiding me along the way with valuable inputs. I am grateful to Linda Bodforss for ensuring a smooth time in the office and attending to whatever needs I had. I thank Mathias Klein for preparing and conducting the entire chassis dynamometer measurements at VCC. I would also like to thank Prof. Leping Feng at KTH for conducting all the measurements at Marcus Wallenberg Laboratory (MWL), Danilo Prelevic for helping with the same and Prof. Mats Åbom for his inputs.

I sincerely appreciate all the assistance and input that I received from Simone, Rikard, Andzrej, Saqib and Anders throughout my time at VCC. I would like to acknowledge all the other masters thesis students at VCC for making my time there even more enjoyable. I am grateful to my classmates Wiktor and Daniel for having read through my thesis and being my kind opponents. I would like to express my gratitude to my supervisor at Chalmers, Dr. Carsten Hoever for all his useful inputs and to Doc. Patrik Höstmad for being my examiner.

Lastly and most importantly, Amma and Appa; words alone cannot describe all your support and sacrifice to get me to where I am today.

Contents

Acknowledgements **vii**

Contents **viii**

List of Figures **xv**

List of Tables **xvii**

1. Background **1**
- 1.1. Introduction to the problem 1
- 1.2. Literature review 1
- 1.3. Mufflers under investigation 3
  - 1.3.1. Front muffler 4
  - 1.3.2. Rear muffler 5

2. Theory **7**
- 2.1. Finite element formulation of acoustic-structure interaction. 7
  - 2.1.1. Model reduction 8
- 2.2. Modelling of sound propagation in porous media 9
  - 2.2.1. Delany-Bazley model 10
- 2.3. Experimental determination of muffler characteristics and boundary conditions 10
  - 2.3.1. Plane wave propagation in ducts 11
  - 2.3.2. Two microphone method 12
  - 2.3.3. Determination of modal damping from vibration data 13

3. Experimental investigation of muffler characteristics. **15**
- 3.1. Cold condition measurements 15
  - 3.1.1. Measurement setup 16
  - 3.1.2. Equipment 19
  - 3.1.3. Sensor location 21
  - 3.1.4. Structural modal damping ratios 22
  - 3.1.5. Fluid modal damping loss factors 23

3.2. Hot condition measurements 24
    3.2.1. Measurement setup 24
    3.2.2. Accelerometer and microphone placement 25
    3.2.3. Engine operating conditions 26

4. Simulation methodology 29
4.1. CAD model generation 29
4.2. Meshing 30
    4.2.1. Muffler interior 30
    4.2.2. Muffler exterior 30
    4.2.3. Muffler structure 31
4.3. Setup physical model 31
    4.3.1. Exterior acoustic domain 32
    4.3.2. Structural domain 33
    4.3.3. Acoustic-structure interaction 34
    4.3.4. Interior acoustic domain 34
4.4. Apply boundary conditions 35
    4.4.1. Structural boundary conditions 35
    4.4.2. Acoustic boundary conditions 36
    4.4.3. Temperature conditions 38

5. Simulation and measurement results and discussion 41
5.1. Experimental investigation - Loudspeaker input 42
    5.1.1. Coherence 42
    5.1.2. Transfer functions 42
5.2. Fluid cavity model of muffler 44
    5.2.1. Influence of acoustic boundary conditions 44
    5.2.2. Determination of flow resistivity 45
    5.2.3. Eigenvalue analysis 46
5.3. Vibroacoustic model 46
    5.3.1. Rear muffler 46
    5.3.2. Front muffler 52
5.4. Modal coupling model 55
5.5. Experimental investigation - Engine operating conditions 56
5.6. Elevated temperature simulation models 60
    5.6.1. Vibroacoustic simulation 60
    5.6.2. Eigenvalue analysis of the structure 62

6. Conclusions 65
6.1. Summary 65

6.2. Conclusions 66
6.3. Recommendations 67
6.4. Future work 68

A. Appendix - Derivations **69**
A.1. Wave propagation in circular ducts. 69
A.2. Experimental determination of boundary conditions. 71
  A.2.1. Inlet velocity 71
  A.2.2. Impedance 72
A.3. Finite Element Model of Acoustic-Structure interaction. 73
  A.3.1. FE model - Structure 73
  A.3.2. FE model - Fluid 73
A.4. Modal damping in structures 76

B. Appendix - Sensorwise results **79**
B.1. Loudspeaker input measurement results. 80
  B.1.1. Sound pressure level transfer functions 80
  B.1.2. Velocity level transfer functions 82
B.2. Simulation results 84
  B.2.1. Sound pressure level transfer functions 84
  B.2.2. Velocity level transfer functions 86
B.3. Engine running condition measurement results 88

Bibliography **93**

List of Figures

1.1. Exhaust system components 4
1.2. CAD representation of front muffler. 4
1.3. CAD representation of rear muffler. 5

3.1. Schematic of measurement setup-Foam plug termination. 17
3.2. Schematic of measurement setup-Rigid termination. 18
3.3. Measurement setup used at MWL, KTH. 20
3.4. Microphone locations around the front muffler. 21
3.5. Microphone locations around the rear muffler. 22
3.6. Accelerometer locations on the front muffler. 22
3.7. Accelerometer locations on the rear muffler. 23
3.8. Damping ratio spectrum 24
3.9. Measurement setup used at VCC. 25
3.10. Sensor locations for hot condition measurements. 26
3.11. Exhaust temperature variation for different engine operating conditions. Trial numbers shown in the legend. 27

4.1. Interior fluid cavity mesh. All compartments not pink in color are the compartments containing the porous material. 30
4.2. Exterior fluid mesh. The infinite element envelop surrounds the external wrap. 31
4.3. Connection curves and connection elements. 32
4.4. Complete simulation setup. The points are the field points where acoustic quantities were evaluated. These points correspond to measurement locations. 32
4.5. Acoustic-Structure interface mapping quality - Rear Muffler. 35
4.6. Nodes on front and rear mufflers with prescribed displacement boundary conditions 36
4.7. Application of radiation boundary conditions for the front muffler. 36
4.8. Application of radiation boundary conditions for the rear muffler. 37
4.9. Exit or termination impedance normalized w.r.t plane wave impedance. . 37
4.10. Inlet impedance normalized w.r.t plane wave impedance. 37

4.11. Incoming wave velocity spectrum 38
4.12. Temperature distribution on the rear muffler shell. 39
4.13. Variation of temperature of various muffler shell regions with fluid temperature. 39

5.1. Coherence spectrum for measured signals. 43
5.2. Measured TFs for the front muffler. 43
5.3. Measured TFs for the rear muffler. 44
5.4. Axial transmission loss for rear muffler 45
5.5. Eigenmodes of rear muffler 47
5.6. Contact region identified by Sol 400. 48
5.7. Transmission loss comparison plots for the rear muffler. 49
5.8. TF comparison plots for the stock rear muffler. SPL TFs are on the right and surface velocity TFs are on the left. 50
5.9. Structural eigenmodes of the rear muffler. 51
5.10. TFs of the front muffler - Influence of porous material. 53
5.11. TFs of the front muffler - Influence of baffle connections. 53
5.12. TFs of the front muffler - Influence of Z-bracket. 55
5.13. Modal coupling model results for the stock rear muffler. 56
5.14. Engine operating conditions - ⅔ POT, 3000-4000 RPM sweep. 57
5.15. Engine operating conditions - WOT, 1250-5500 RPM sweep. 58
5.16. Measured acceleration level plots at Accelerometer ‘*H08*’. 59
5.17. Surface acceleration level TFs with respect to inlet averaged across all 6 accelerometers. 61
5.18. Surface acceleration level TFs with respect to inlet averaged across all 6 accelerometers. 61

B.1. Measured SPL transfer function comparison plots for the rear muffler. . . 80
B.2. Measured SPL transfer function comparison plots for the front muffler. . . 81
B.3. Measured velocity level comparison plots for the rear muffler. 82
B.4. Measured velocity level comparison plots for the front muffler. 83
B.5. SPL comparison plots for the rear muffler for all microphones. 84
B.6. SPL comparison plots for the front muffler for all microphones. 85
B.7. Velocity level transfer function comparison plots for the rear muffler for all accelerometers. 86
B.8. Velocity level transfer function comparison plots for the front muffler for all accelerometers. 87
B.9. 1/3 POT, 3000-4000 RPM 88
B.10. 1/3 POT, 4000-5000 RPM 88
B.11. 1/3 POT, Full RPM 89

B.12. $^2/_3$ POT, 3000-4000 RPM 89
B.13. $^2/_3$ POT, 4000-5000 RPM 90
B.14. $^2/_3$ POT, Full RPM 90
B.15. WOT, 3000-4000 RPM 91
B.16. WOT, Full RPM 91

List of Tables

3.1. Engine operating conditions 27
5.1. Mean eigenfrequency drop due to temperature elevation 62

1. Background

1.1. Introduction to the problem

It is of prime importance in the automotive industry to reduce development time for new vehicle models. In order to achieve this, one must be able to rely more heavily on simulations to speed up the process. The simulation model must therefore be validated to ensure its reliability. It is in this context that the objective of this thesis has been established.

The exhaust line remains one of the most important sources of noise from an automobile. Reliable models exist at VCC to simulate flow and heat related noise phenomena in the exhaust system. However, there exists a requirement to develop a sufficiently detailed and accurate model that can predict the noise radiated from the exhaust muffler's structure, which is excited by the gas pulsations originating from the engine. To accomplish this task is therefore the objective of the thesis.

1.2. Literature review

The problem of simulating the breakout noise from an automotive muffler is one that has been revisited many times in the past and continues to be of interest to the academic and industrial community. Some of the notable ones are mentioned briefly below. Most of the early attempts at simulating the transverse sound transmission through exhaust mufflers, analytically or numerically, have dealt with only the simplest muffler shapes such as a cylinder, at room temperature and devoid of any interior constructions. However, conventional mufflers rarely possess such simplistic shapes as their interior volumes have been maximised while keeping within the packaging constraints.

One of the earlier attempts to simulate the surface radiated noise of exhaust mufflers was done by Brand et al[1]. Vibrations on a simple muffler with a doubled layered outer shell and a single baffle, caused due to a frequency dependent gas pulsation force was analysed through the FE method. The influence of muffler properties such as insulation, stiffness, damping and excitation on the surface velocity levels and the first eigenfrequency of the structure was studied in a parametric analysis. The influence was graded qualitatively into four categories to serve as a preliminary guide during the early design stages. With this model, only the vibration amplitude of the first mode was found to be accurately simulated.

A more exhaustive analysis of breakout noise from mufflers was performed by Narayana et al[2]. A simple circular muffler with a cylindrical shell expansion chamber was considered. The axial transmission loss is defined as the difference between the incident and transmitted power through the muffler when it has anechoic termination. The transverse transmission loss is defined as the difference between the incident power and power transmitted through the muffler shell rather than the exit duct. These two quantities were predicted using FE and BE methods and compared with experimentally obtained results. Further, the effect of various designs of the muffler shell and the end plates on the transverse transmission loss was studied and parametric studies were presented to assist in the muffler design process. Computationally obtained transverse transmission loss spectrum was found to follow the trend of the measured one at mid to higher frequencies but the amplitudes were overestimated throughout the mid-frequencies and underestimated at the higher frequencies.

Approximate analytical methods were used by Chulho et al[3] to determine structural eigenfrequencies of the muffler structure. A typical muffler shape with a large curved area with a low curvature along with high curvature areas on the sides was considered. The large area was considered as a cylindrical panel whose width is optimised by minimising the strain energy. The obtained modeshapes from an FE analysis were used to determine the vibration patterns in the frequency range of interest to design appropriate solutions like stiffening the structure by adding baffles or increasing damping by adding more shell layers. These results were used to diagnose shell implosion issues.

The most detailed study available in academic literature, of radiated shell noise from exhaust mufflers was performed by Junge et al[4]. A production series rear muffler of which the inner structural parts were removed was used for all measurements and analyses which were conducted under ambient conditions without mean flow. First, an experimental modal analysis was carried out to determine modeshapes, eigenfrequencies and modal damping ratios. Then, excitations on the structure due to a pressure input were measured as transfer functions. These results were then compared to an FE-FE coupled fluid-structure model. A model updating procedure was employed to adjust the structural part of the FE model to the results of the experimental modal analysis. The overall physical behavior was found to be reasonably reproduced by the simulation. The magnitudes of the simulation results were slightly higher than those of the experiment. Furthermore, a frequency shift of a few Hertz for the maximum values was observed. Finally the results of the FE computation were used as Neumann boundary data for the solution of the exterior acoustic problem which was solved using a fast multipole BE model.

To the best of the author's knowledge, a comprehensive simulation model that predicts the radiated noise taking into account all the structural features of a complex automotive muffler and the effects of elevated temperature under operating conditions closer to the running conditions of the car, is yet to be found in existing academic literature. This thesis intends to model, with sufficient accuracy, the breakout noise from a mass produced automotive muffler with all internal components such as baffles still attached under room temperature conditions with zero mean flow. This model will be validated using measurements conducted in an anechoic chamber under similar environmental conditions with a loudspeaker input. This validated model will then be used to further investigate the effects of elevated temperature.

1.3. Mufflers under investigation

For the purposes of this thesis, two different mufflers have been used for all analyses:

- Front muffler
- Rear muffler

These mufflers are positioned in the exhaust system of the Volvo XC90 as shown in Figure 1.1.

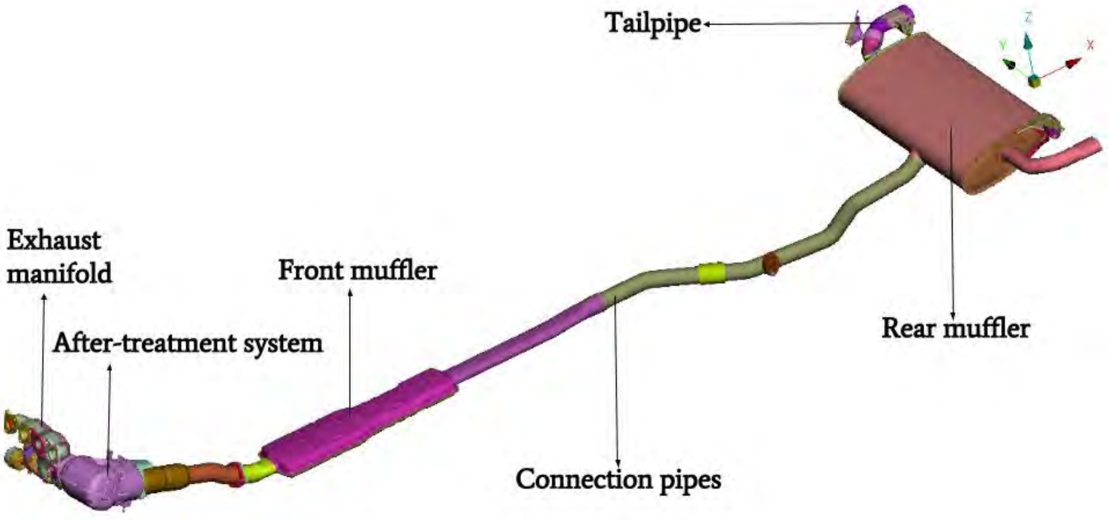

Figure 1.1.: Exhaust system components

1.3.1. Front muffler

The front muffler, shown in Figure 1.2c, is directly connected to the engine on one side and to the rear muffler on the other. Some initial measurements have been conducted at VCC on this muffler's shell noise characteristics and it has been determined that a more detailed analysis is required. This muffler is filled with glass wool of mostly unknown material properties in three of its four chambers. This uncertainty is expected to be one of the challenges while creating a poroacoustic model of this muffler. Measurements on this muffler will only be conducted under cold conditions in the anechoic chamber due to time constraints.

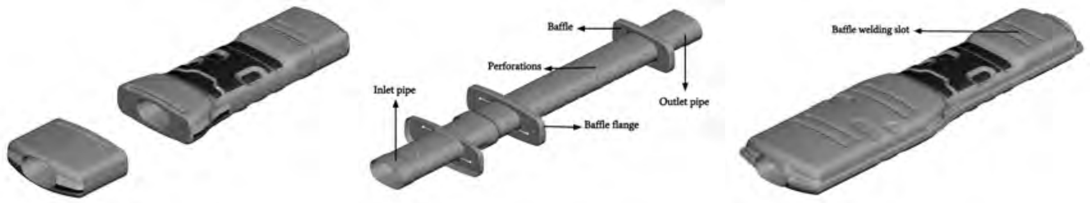

(a) Porous material
(b) Interior parts
(c) Completely assembled part

Figure 1.2.: CAD representation of front muffler.

1.3.2. Rear muffler

The rear muffler, shown in Figure 1.3c, is connected to the front muffler on one side and to the tailpipes on the other. It is made of Ferritic Steel sheet metal crimped, rolled and hemmed together. Unlike the front muffler, it does not contain any glass wool. Large surface areas between the baffles could prove to be efficient radiators of shell noise. Of particular concern is the effect of the baffle-outer shell connections on the radiated noise, especially the elevated temperature conditions that are present under actual operating conditions of the vehicle. In order to further investigate this effect, two versions of this muffler are considered, one which is the stock muffler, i.e where the baffles are in place simply due to an interference fit and frictional forces, and another where the baffles have been spot welded at six points each along its contact region with the outer shell as seen in Figure 1.3d.

(a) Interior parts

(b) Outer shell

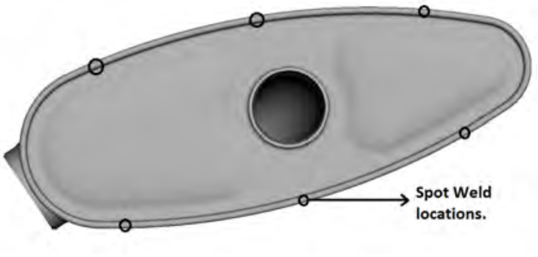

(d) Spot weld locations

(c) Completely assembled part

Figure 1.3.: CAD representation of rear muffler.

2. Theory

In this chapter, some basic theory behind the concepts applied in the thesis work is described briefly.

2.1. Finite element formulation of acoustic-structure interaction.

The commercial software package, MSC ACTRAN, which has been used for all vibroacoustic analyses in this thesis, couples a physical fluid model with a modal model of the structure obtained from NASTRAN. This is referred to as a hybrid vibroacoustic model since one of the two interacting systems is a physical model while the other is a modal model.

The physical structural and fluid FE model equations can be obtained separately as shown in Appendix A. Then, the fluid FE discretization and structural FE discretization from equations (A.37) and (A.31) can be applied to the fluid structure interaction boundary condition terms h_a and h_s.

$$h_s = \sum_{(e)} \int_{\Gamma_{a,i}} \rho_0 \boldsymbol{N}_{a,i}^T (\overrightarrow{\ddot{w}}^T . \overrightarrow{n}_i) \ \mathrm{d}\Gamma_{a,i} \tag{2.1}$$

$$\overrightarrow{h}_a = \sum_{(e)} \int_{\Gamma_s} \boldsymbol{N}_{s,i}^T \overrightarrow{n}_i p \ \mathrm{d}\Gamma_{s,i} \tag{2.2}$$

These terms can then be substituted in the following equations (the expressions for the remaining terms can be found in Appendix A) to result in a simple matrix representation for acoustic-structure interaction shown in (2.5),

$$\boldsymbol{M}_s \overrightarrow{\ddot{u}} + \boldsymbol{C}_s \overrightarrow{\dot{u}} + \boldsymbol{K}_s \overrightarrow{u} + \overrightarrow{h}_{0s} + \overrightarrow{h}_a = 0 \tag{2.3}$$

$$\boldsymbol{M}_a \overrightarrow{\ddot{\mathrm{p}}} + \boldsymbol{C}_a \overrightarrow{\dot{\mathrm{p}}} + \boldsymbol{K}_a \overrightarrow{\mathrm{p}} + \overrightarrow{h}_s + \overrightarrow{h}_{0a} = 0 \tag{2.4}$$

$$\begin{bmatrix} \boldsymbol{M}_s & \boldsymbol{0} \\ \rho_0 \boldsymbol{Q}^T & \boldsymbol{M}_a \end{bmatrix} \begin{Bmatrix} \ddot{\overrightarrow{u}} \\ \ddot{\mathrm{p}} \end{Bmatrix} + \begin{bmatrix} \boldsymbol{C}_s & \boldsymbol{0} \\ \boldsymbol{0} & \boldsymbol{C}_r \end{bmatrix} \begin{Bmatrix} \dot{\overrightarrow{u}} \\ \dot{\mathrm{p}} \end{Bmatrix} + \begin{bmatrix} \boldsymbol{K}_s & \boldsymbol{Q} \\ \boldsymbol{0} & \boldsymbol{K}_a \end{bmatrix} \begin{Bmatrix} \overrightarrow{u} \\ \mathrm{p} \end{Bmatrix} + \begin{Bmatrix} \boldsymbol{h}_{0s} \\ \boldsymbol{h}_{0a} \end{Bmatrix} = 0 \tag{2.5}$$

Where the coupling matrix is given by,

$$\boldsymbol{Q} = \sum_{(e)} \int_{\Gamma_{as,i}} \boldsymbol{N}_{s,i}^T \overrightarrow{n}_i \boldsymbol{N}_{a,i} \, \mathrm{d}\Gamma_{as,i} \tag{2.6}$$

2.1.1. Model reduction

For complicated geometries such as the mufflers under analysis, the computational time increases greatly if the physical model of the structure is used due to the excessively high degrees of freedom. If a frequency response analysis is performed upon the geometry, from Fourier analysis, it is known that the higher order modes affect the behaviour of the system at the lower frequencies to a negligible extent. This fact is exploited when a modal model reduction is performed on the structure to reduce the number of DoFs and to speed up computation.

In an alternative analysis method that is explored, even the fluid model is converted to a modal model. This is done by performing an eigenvalue analysis of the equation (2.4) and extracting the eigenmodes of the muffler interior cavity. However, this means that the radiation boundary conditions cannot be accounted for as it appears in the fluid "damping" term. Therefore, this analysis will use a closed volume to couple with the structure.

A model reduction is performed by transforming the physical coordinates to modal coordinates and then eliminating all the modes present at frequencies higher than twice the highest frequency under consideration. This modal model reduction is performed via the following transformation[5],

$$\overrightarrow{u} = \boldsymbol{\Phi}_{\{n_s \times q\}} \overrightarrow{\eta} \tag{2.7}$$

Where $\overrightarrow{\eta}$ contains the modal participation coefficients or factors, which is a vector containing the contributions of each mode to the operational deformation shape of the structure at frequency ω and $\boldsymbol{\Phi}$ is the modal matrix containing a n_s DOF long eigenvector for q modes. This transformation orthogonalizes or diagonalizes the mass and stiffness matrices as follows,

$$\widetilde{\boldsymbol{M}}_s = \boldsymbol{\Phi}^T \boldsymbol{M}_s \boldsymbol{\Phi} = \mathrm{diag}(\delta_{ij}) \tag{2.8}$$

$$\widetilde{\boldsymbol{K}}_s = \boldsymbol{\Phi}^T \boldsymbol{K}_s \boldsymbol{\Phi} = \mathrm{diag}(\lambda_i \delta_{ij}) \tag{2.9}$$

Here, δ_{ij} is the Kronecker delta function, $\lambda_i = \omega_i^2$ is the i^{th} eigenvalue of the structure and ω_i is the i^{th} eigenfrequency or the resonance frequency of the i^{th} uncoupled mode. If a modal damping model is used, the damping matrix too is assumed to be diagonalized as shown in 2.3.3. In addition to these three matrices, the coupling matrix, $\boldsymbol{Q}$, and the prescribed boundary conditions, $\boldsymbol{h}_{0s}$, are also transformed as follows,

$$\widetilde{\boldsymbol{Q}} = \Phi^T \boldsymbol{Q} \qquad \tilde{\boldsymbol{h}}_{0s} = \Phi^T \boldsymbol{h}_{0s} \tag{2.10}$$

For a more detailed approach to the FE modelling of acoustic-structure interaction, the subsequent transformation of physical coordinates to modal coordinates which is only outlined in this thesis, alternative approaches such as potential formulations and a detailed CALFEM[6] implementation of acoustic-structure interaction, the reader is encouraged to refer to the chapter, '*Fundamentals of Fluid-Structure Interaction*' by Sandberg et al[7].

2.2. Modelling of sound propagation in porous media

As mentioned in Chapter 1, the front muffler contains regions filled with porous glasswool material. Porous materials such as glasswool are made up of an elastic frame surrounded by air. For such materials, a term called porosity, φ, can be defined as follows[8],

$$\varphi = \frac{V_a}{V_T} \tag{2.11}$$

Where the volume of air V_a and the total volume of the porous material V_T are related to the volume of the elastic frame V_b as $V_a + V_b = V_T$. The value of porosity for such materials is often found to be close to unity. In such cases, the most commonly used approach for modelling their acoustical properties is through the use of an equivalent fluid with modified wave number and characteristic impedance. One such model is the Delany-Bazley model, which is available on MSC Actran and is also one of the most commonly used models.

2.2.1. Delany-Bazley model

According to this model, the characteristic impedance Z_c and the complex wave number k for highly porous materials can be expressed empirically as follows,

$$Z_c = \rho_0 c_0 \left[1 + 0.0571X^{-0.754} - j0.087X^{-0.732}\right] \tag{2.12}$$

$$k = \frac{\omega}{c_0}\left[1 + 0.0978X^{-0.700} - j0.189X^{-0.595}\right] \tag{2.13}$$

Where c_0 is the free stream sonic velocity, ω is the angular frequency and ρ_0 is the density of air at room temperature. X is a dimensionless quantity defined as,

$$X = \frac{\rho_0 f}{\sigma} \tag{2.14}$$

σ is the flow resistivity of the porous material defined for a plane wave incident normally on a specimen of the porous material of thickness e.

$$\sigma = \frac{\Delta p}{Qe} \tag{2.15}$$

Where Δp is the pressure differential across the porous material and Q is the air flux through the porous material.

Frequency limits

The Delany-Bazley model has frequency limits for each value of flow resistivity within which the model is sufficiently accurate. These limits are defined, for every value of flow resistivity σ as,

$$\frac{0.01\sigma}{\rho_0} < f < \frac{\sigma}{\rho_0} \tag{2.16}$$

2.3. Experimental determination of muffler characteristics and boundary conditions

The quantities to be determined experimentally are the following:

- Inlet impedance
- Inlet acoustic particle velocity

- Exit impedance
- Modal damping ratios
- Axial transmission loss

Of these, only the axial transmission loss is compared to the corresponding quantity in the simulation model while the remaining properties are in fact input into the simulation model to replicate experimental conditions.

2.3.1. Plane wave propagation in ducts

The experimental determination of muffler properties relies on a fundamental property of sound propagation in ducts; the property that a duct mode becomes non-evanescent and propagates only above a certain cutoff frequency. For circular ducts such as the ones present in the inlet to the mufflers used in this analysis at ambient room temperature with zero mean flow, the following expression (derived in Appendix A), is used for the determination of cutoff frequencies for various modes,

$$\omega_c = \frac{j'_{m\mu} c_0}{R} \tag{2.17}$$

where R is the radius of the duct. Below this critical frequency, a wave cannot propagate since the wavenumber becomes imaginary and the corresponding duct mode, $p_x(x)$ whose expression is given in (A.18), exponentially decays with axial distance. For the ducts present in the exhaust system, $R = 0.031$ m, $\mu = 1$ for a plane wave, $m = 0$ in the presence of no azimuthal modes at all and $m = 1$ for the first azimuthal mode. j'_{01} and j'_{11} are known standard values of 0 and approximately 1.84 respectively. Using these values, it is found that the critical frequency for the propagation of a plane wave is 0 Hz and that of the first circumferential mode is around 3200 Hz. This means that a plane wave propagates at all frequencies and the first circumferential mode starts propagating above a frequency of about 3200 Hz. This frequency is therefore the highest frequency considered in the measurements. Given that a plane wave is the only wave that propagates, (A.18) simplifies to the following,

$$p_x(x) = p_{x0} e^{\pm ikx} \tag{2.18}$$

This equation indicates that the plane wave sound field in a duct below the first cutoff frequency is essentially a linear combination of two waves (i.e the two solutions to the above equation). With this in mind, the pressure at any point can be modelled as the sum of an incident and reflected plane wave as shown below. A reflected wave is present in any finite sized duct due to reflection at the duct termination.

$$p_x(x) = p^+ e^{-ikx} + p^- e^{ikx} \tag{2.19}$$

2.3.2. Two microphone method

Plane wave decomposition

It is clear from the preceding equation that two variables, p^+ and p^-, are required to define the sound field at any point in a uniform duct without mean flow. Therefore two equations involving the two variables are necessary to determine the amplitudes of the incident and reflected waves. In order to obtain the two equations, pressures, p_{x_0} and $p_{x_0+\Delta x}$, at two different microphone positions, say x_0 and $x_0 + \Delta x$ respectively, are recorded[9]. The complex transfer functions at these positions, $H_1(\omega)$ and $H_2(\omega)$ respectively, with respect to the reference signal are also recorded to obtain the corresponding phase data. With this data, the forward and backward travelling wave amplitudes can be determined using the expression below, (refer A.2)

$$\begin{Bmatrix} p^+_{inlet} \\ p^-_{inlet} \end{Bmatrix} = \frac{1}{e^{ik\Delta x} - e^{-ik\Delta x}} \begin{bmatrix} e^{ik\Delta x} & 1 \\ -e^{-ik\Delta x} & 1 \end{bmatrix} \begin{Bmatrix} p_{x_0} \\ p_{x_0+\Delta x} \end{Bmatrix} \tag{2.20}$$

The velocity of the forward travelling wave at the inlet can then be expressed in terms of the plane wave impedance, $Z_0 = \rho_0 c_0$ as follows.

$$v_{inlet} = \frac{p^+_{inlet}}{Z_0} \tag{2.21}$$

Impedance determination

Since the complex impedance boundary conditions at the in- and outlet of the muffler are crucial inputs to the simulation model, it must be calculated accurately. To do so, the complex impedance can be redefined through transfer functions as follows,[9]

$$Z_{inlet} = \frac{S_{p_0 v_0}}{S_{v_0 v_0}} \tag{2.22}$$

where S_{pv} is the cross-spectrum between the pressure and velocity at the inlet and S_{vv} is the auto-spectrum of the velocity at the inlet. This can be expressed as (Appendix

A.2),

$$\frac{Z_{inlet}}{Z_0} = \frac{S_{p^+p^+} + S_{p^-p^-} - 2i\ \mathfrak{Im}(S_{p^+p^-})}{S_{p^+p^+} - S_{p^-p^-} - 2\ \mathfrak{Re}(S_{p^+p^-})} \tag{2.23}$$

Where $S_{p^+p^-}$ is the cross-spectrum between the forward and backward travelling waves in the muffler inlet duct, $S_{p^+p^+}$ is the auto-spectrum of the forward travelling wave and $S_{p^-p^-}$ is the auto-spectrum of the backward travelling wave. These quantities can be computed from the measured transfer functions, $H_1(\omega)$ and $H_2(\omega)$ using a transformation matrix (derived in Appendix). A similar procedure can be employed at the muffler exit to determine the impedance of the termination.

Transmission loss computation

The auto-spectrum of the forward travelling waves in the in- and outlet, can be expressed as $S_{p^+_{in}p^+_{in}}$ and $S_{p^+_{ex}p^+_{ex}}$ respectively. They are determined from the transfer functions at the two microphones at the inlet as well as the outlet and can be used to compute the transmission loss exhibited by the muffler under measurement defined as follows,

$$TL = 10\ \log_{10}\left(\frac{S_{p^+_{in}p^+_{in}}}{S_{p^+_{ex}p^+_{ex}}}\right) \tag{2.24}$$

Frequency limits of the two microphone method

However, as noted by Åbom, Bodén[10], the two microphone method is determined to be least sensitive to errors in input data within the following frequency range,

$$\frac{0.05c_0}{\Delta x} < f < \frac{0.4c_0}{\Delta x} \tag{2.25}$$

Therefore in order to cover the entire frequency range of interest, three microphones have been used providing separation distances of $\Delta x_1 = 45\text{mm}$ and $\Delta x_2 = 180\text{mm}$. Based on the expression shown above, this gives a frequency range rounded off to $f \in \{100\ \text{Hz}, 3200\ \text{Hz}\}$ where the two microphone measurements are reliable.

2.3.3. Determination of modal damping from vibration data

The autospectrum data from accelerometers mounted on the muffler is available at 9 different points. From this data, the average modal damping of the muffler shell structure is determined using the half power bandwidth method detailed in Appendix A. The final relation for the damping ratio, ξ_r for the r^{th} mode in terms of the half power bandwidth $\Delta\omega$ and the resonance frequency of the r^{th} mode, ω_r.

$$\xi_r = \frac{\Delta\omega}{2\omega_r} \tag{2.26}$$

The half power bandwidth frequencies correspond to a 3 dB reduction in the acceleration level in the autospectrum plot.

3. Experimental investigation of muffler characteristics.

Measurement data is required to validate the simulation model for breakout noise from a muffler in order to establish its reliability. This data was obtained through a frequency response measurement conducted on the mufflers in an anechoic environment. The induced vibrations at certain points on the muffler shell structure caused by an acoustic excitation and the subsequently radiated noise at select points in the radiation field around the muffler were the measured quantities chosen for this purpose.

The aforementioned quantities was measured under two completely different conditions:

- **Cold condition measurements**
  For these measurements, a loudspeaker excitation was employed at the inlet of a standalone muffler in the absence of all other parts of the car. These measurements were conducted in an anechoic chamber under room temperature conditions.

- **Hot condition measurements**
  These measurements were performed on the muffler when mounted on the vehicle and therefore the acoustic excitation was the actual gas pulsations from the engine itself. These measurements were made in a semi-anechoic chamber and the local temperature was subject to the operating conditions of the engine.

3.1. Cold condition measurements

The environmental conditions present in the measurement must be easily replicable in a simulation model for the validation process to be meaningful. Since replication of environmental conditions is easier when they are idealized, the cold condition measurements ignores the following effects which are present when the muffler is under actual operating conditions.

- Non-uniform and unsteady temperature profile of the exhaust gases within the muffler.

- Temperature dependent material properties for the muffler shell structure.

- Coupling of purely structural and thermo-mechanical effects present in the muffler shell structure.

- Non-zero mean flow conditions. Though Lee et al[11] have shown experimentally that mean flow does not significantly affect shell radiated noise, the authors have also noted that the result holds only for the simple muffler configuration that they have used.

- Orifice noise and other noise sources from the vehicle.

- Uncertain muffler mounting conditions.

- Uncertain frequency content of gas pulsations from the engine.

These measurements are therefore intended to be the primary source of validation for the simulation models.

3.1.1. Measurement setup

The measurement setup depicted as a schematic in Figure 3.1 was used for the measurements. The room temperature conditions ensured that the thermal effects listed in the first three points were avoided. Hanging the muffler from the ceiling on one side while connecting it with a pipe clamp on the other side ensured that the mounting conditions were fixed and known (Figure 3.3c). This loudspeaker, providing a white noise input, was mounted in the reverberation room adjoining the anechoic chamber (Figure 3.3g). The muffler under test was connected to the loudspeaker through a series of pipes, one of which contained three in-duct microphones. The presence of three in-duct microphones at the inlet ensured that the exact frequency content of the inlet velocity was known for the entire plane wave frequency region. They were also used to determine impedance conditions at the inlet using the two microphone technique detailed in the previous chapter (Figure 3.3h).

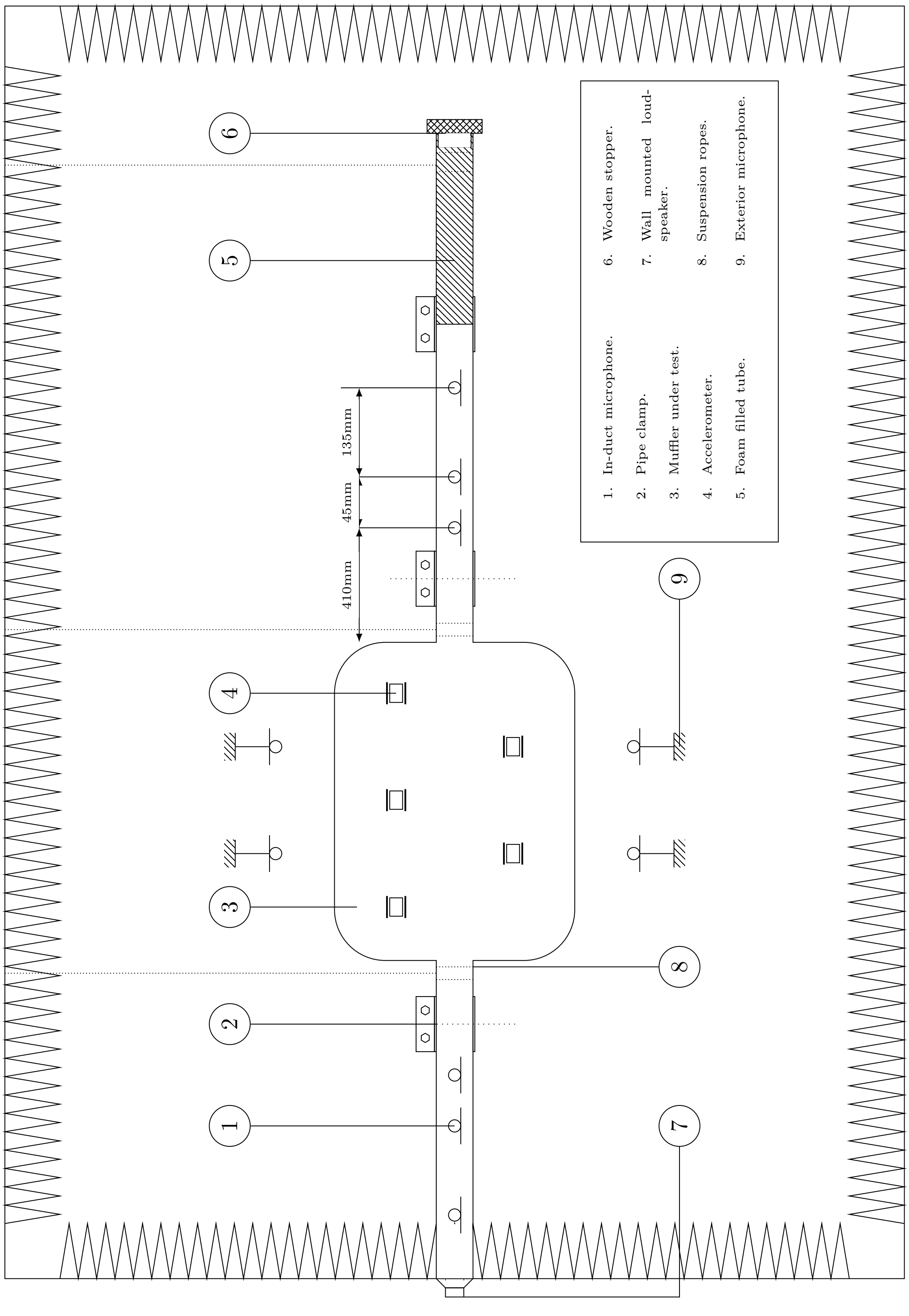

Figure 3.1.: Schematic of measurement setup-Foam plug termination.

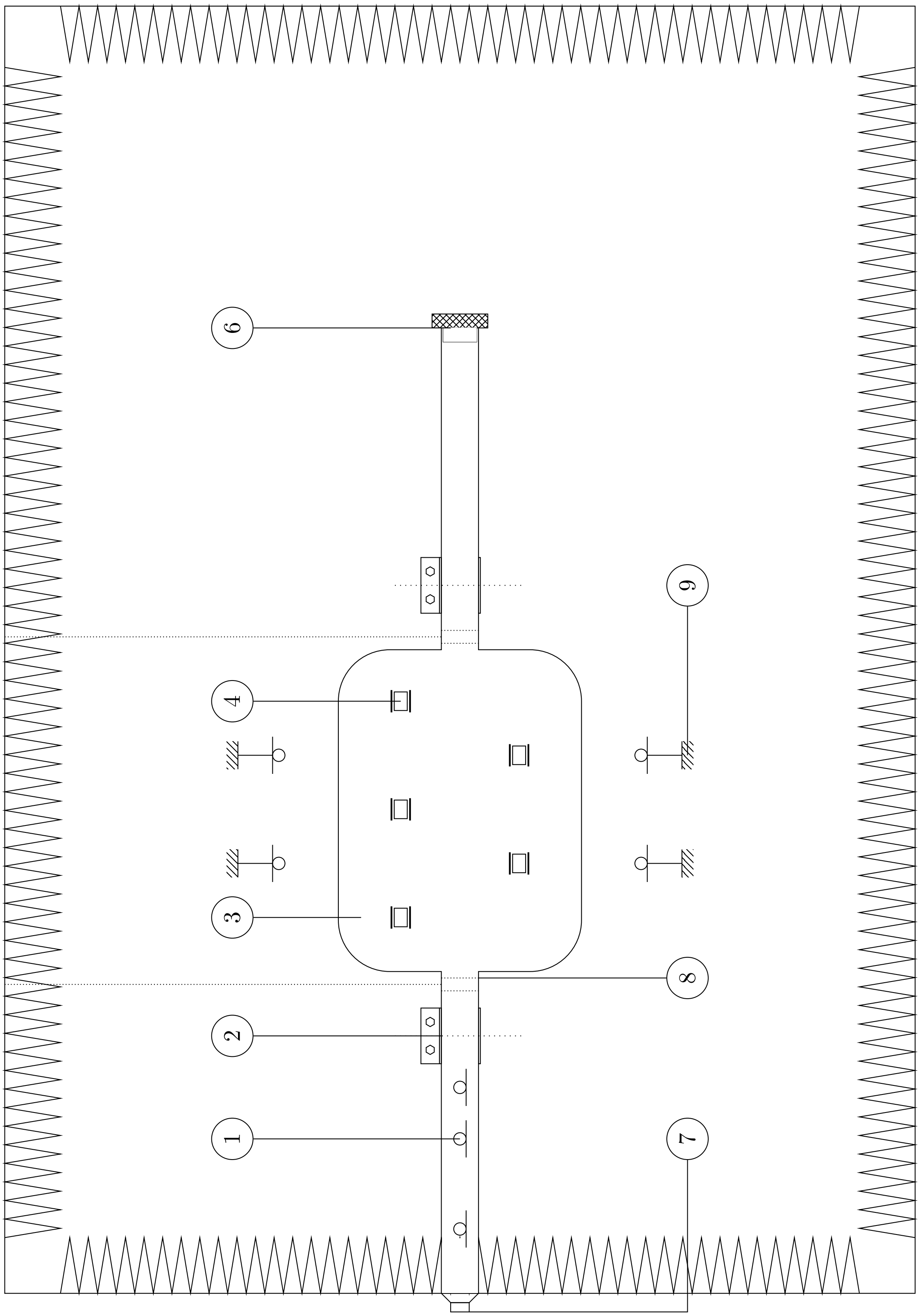

Figure 3.2.: Schematic of measurement setup-Rigid termination.

The foam filled tube or a foam plug with a rigid stopper at the end was connected to the outlet of the muffler. It provided an anechoic duct termination condition and ensured that the orifice noise was not radiated out as shown in Figure 3.3c where it is attached to the right side tailpipe. However, this anechoic termination is in practice not perfectly anechoic, i.e the normalized impedance is not unity, as seen in Figure 4.9 in the following chapter. The exact non-unity value of the normalized impedance at the outlet was therefore determined similar to the inlet section through the presence of three in-duct microphones at the outlet of the muffler in order to be applied to the simulation model. In addition to providing the exact outlet impedance, the wave decomposition procedure at the outlet was also used to measure the transmission loss of the muffler, as shown in 2.3.2.

An alternate way of dealing with this issue was by removing the foam plug altogether and sealing the exit of the muffler with a rigid wooden stopper so that all the outgoing waves were reflected back into the muffler, as shown in a schematic in Figure 3.2 and in practice in Figure 3.3f. In this measurement setup, however, the transmission loss cannot be computed. It must also be noted that the rigid wooden stopper was not sufficient to reflect back all frequencies entirely and partially transmitted some of them. Pictures of the final measurement setup for all the mufflers is shown in Figures 3.3a-3.3h.

As can be seen in the figures, the microphones were positioned at predetermined points from CAD, using welding rods taped to a wooden mounting structure. This proved to be an effective method given the scarcity of mounting points in a fully anechoic chamber. The foam pipe termination was clamped to only one tailpipe in case of the rear muffler.

3.1.2. Equipment

The measurements were conducted in the anechoic chamber at the Marcus Wallenberg Labroratory(MWL), KTH. All the measurement equipment were available in house and their details are listed below.

- 32 channels VXI frontend.
- Personal computer with data acquisition software B&K Pulse.
- $\frac{1}{4}$" Microphone set G.R.A.S. 40BD-S3/26CB.
- Sound Level Calibrator B&K type 4231, series number 2583525.

(a) Front muffler complete setup (b) Front muffler - Side view

(c) Rear muffler complete setup (d) Rear muffler - Bottom view

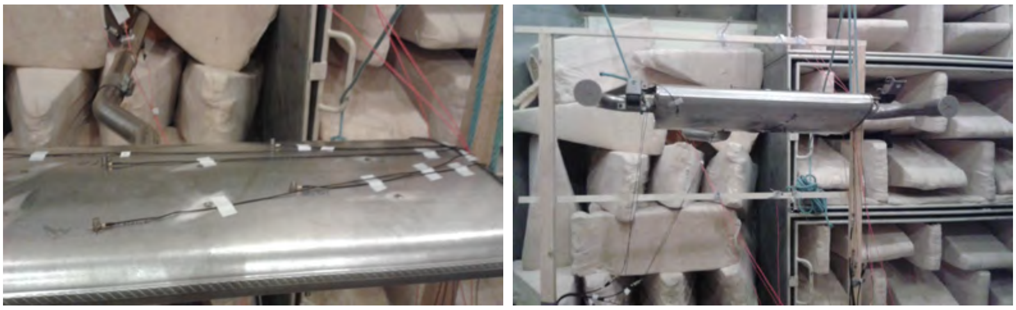

(e) Rear muffler - Top view (f) Rear muffler with an attached rigid stopper

(g) Loudspeaker mounted on a door. (h) Mounted in-duct microphones at the inlet.

Figure 3.3.: Measurement setup used at MWL, KTH.

3.1.3. Sensor location

While the positions of the inlet and outlet in-duct microphones were decided by existing apparatus available at MWL, the microphone positions in the radiated field and the accelerometer locations on the structure were chosen. The available equipment and number of channels limited the number of external microphones to six and the number of accelerometers to nine.

Microphone placement

The six microphone locations in the radiated sound field were chosen manually based on a rudimentary simulation. This simulation identified the regions significantly higher sound pressure levels and the microphones were distributed equally within these high pressure regions so as to capture all of them and maintain a high signal to noise ratio. The distance of these points from the muffler surface along the Z-axis were kept constant at 250 mm in order to locate the points more easily while preparing the measurement setup. Using these approximate guidelines, microphone positions for the front and the rear muffler were chosen and are shown in Figures 3.4-3.5.

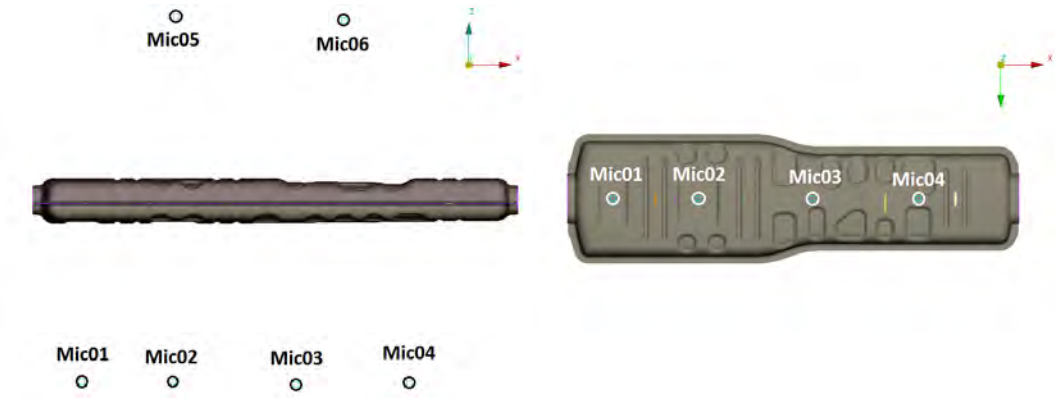

Figure 3.4.: Microphone locations around the front muffler.

Accelerometer placement

In order to determine the location of the nine acccelerometers, the Effective Independence Method developed by Kammer[12] and whose implementation is available as a part of a MATLAB script written by Abrahamsson[13], was used. In this method, a large number

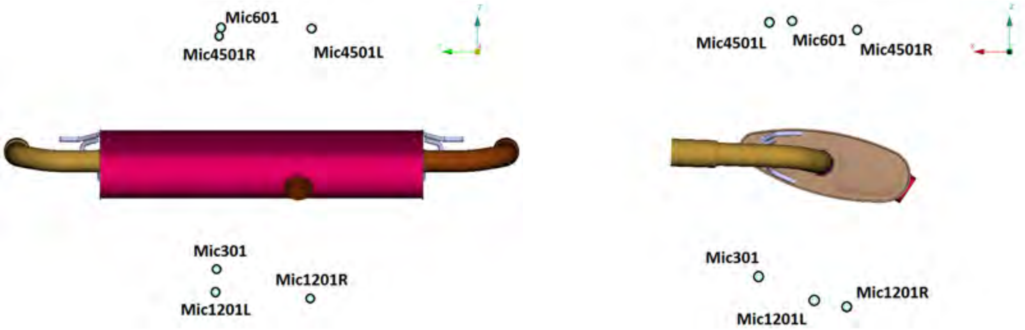

Figure 3.5.: Microphone locations around the rear muffler.

of candidate sensor locations were set up based on mounting considerations and other general guidelines. Then, the pool of the candidate sensor locations was narrowed down through an iterative process by deleting the DOFs of the modal matrix $\mathbf{\Phi}$ one by one until the number of DOFs in the modal matrix equaled the number of sensor locations desired. This modal matrix contained all modes upto around 800 Hz. Which DOF was removed depended on the determinant of the Fisher Information Matrix, defined as $\boldsymbol{F} = \Phi^T\Phi$, where Φ is the modal matrix left over after the DOF's removal. The removal of that DOF which maximised $\boldsymbol{F}$ was chosen and the DOF discarded and the procedure iterated. This procedure led to the distribution of accelerometers mounted on the front and rear mufflers shown in Figures 3.6-3.7.

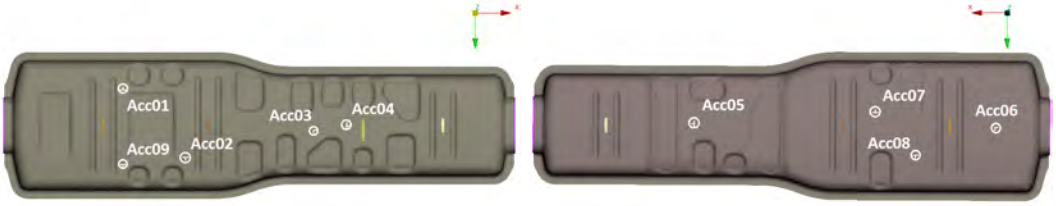

Figure 3.6.: Accelerometer locations on the front muffler.

3.1.4. Structural modal damping ratios

As shown in Section 2.3.3, the modal damping ratios for a structure can be determined from the measured acceleration spectrum at different accelerometer positions and then averaged. Shown in Figure 3.8a are the global damping ratio plots calculated by in-

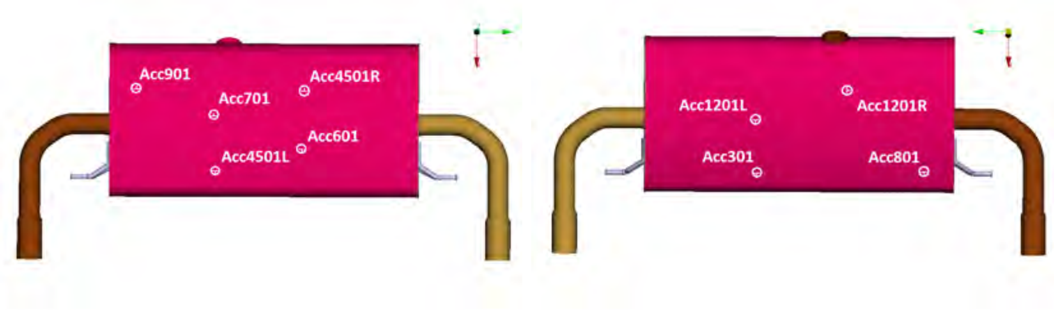

Figure 3.7.: Accelerometer locations on the rear muffler.

terpolating the modal damping ratios to all the intermediate frequencies between the modes. The modal damping ratios were calculated in turn according to the half power bandwidth method. In the process of calculating them, the modes with a damping ratio of more than 10% were capped off at 10% as they were assumed to be outliers. Modal damping ratios calculated by Junge et al[4] through an Experimental Modal Analysis have also been plotted alongside for comparison. The damping ratios obtained from literature can be seen to be considerably lower than the ones computed from the measurements. This can be attributed to the fact that the muffler used in the literature has no interior parts such as baffles and pipes. The crimps, welds, rolls and interference fits which are used to assemble all the internal parts along with the outer shell cause additional losses in the muffler system compared to when only the outer shell is considered. In addition, the mufflers in the measurements are also larger in size compared to the muffler used in literature. While the rear muffler shows acceptable damping ratio levels for a sheet metal structure, the front muffler shows higher than expected damping ratios which does not also have the smooth nature of the rear muffler's. This can be attributed to the influence of the porous glasswool material interacting with the muffler shell structure.

3.1.5. Fluid modal damping loss factors

The half power bandwidth method used for determining the structural damping ratios was also used for determining the damping losses in the air within the muffler. The damping loss factor was then averaged across the six in-duct microphones and a similar capping of outlying damping ratios was performed. The final damping loss spectrum is presented in Figure 3.8b. Similar to the structural modal damping ratios, the fluid damping loss factors for the front muffler are higher than those for the rear due to the influence of the porous glasswool material.

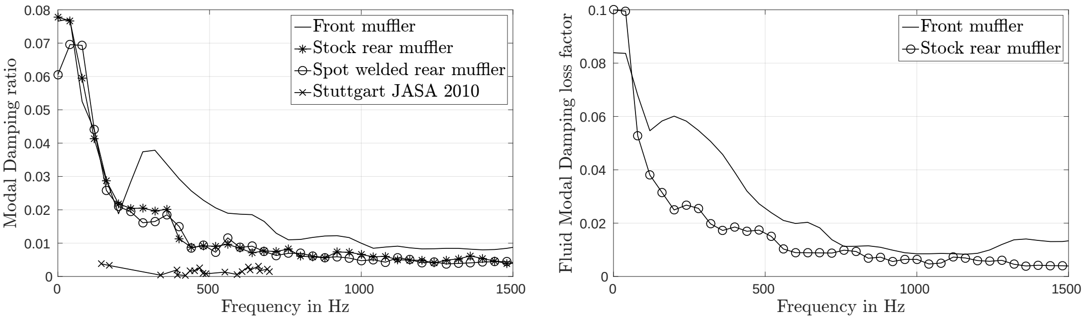

(a) Global structural damping ratio calculated from accelerometer spectra.

(b) Fluid damping loss factors calculated from microphone spectra.

Figure 3.8.: Damping ratio spectrum

3.2. Hot condition measurements

Measurements were conducted on the rear muffler when connected to the engine, which was in turn mounted on the car, under various operating conditions. As mentioned in the previous section, these measurements were intended to be used purely to study the vibration and radiation behaviour of the muffler shell rather than to explicitly validate the simulation model.

3.2.1. Measurement setup

All measurements were conducted inside a semi-anechoic chamber at VCC. The muffler in question was mounted on the car, a Volvo XC90. The car was operated on a chassis dynamometer test cell present inside the semi-anechoic chamber, as shown in Figures 3.9a-3.9f.

The car was held in position on the chassis dynamometer while an exhaust ventilator was used to route the exhaust gases coming out of the tailpipe out of the anechoic chamber. The car was driven in 2WD mode throughout the measurements with no power transferred to the rear wheels. This was done to minimize the noise sources close to the nearfield microphones which were placed beneath the rear muffler to measure radiated shell noise.

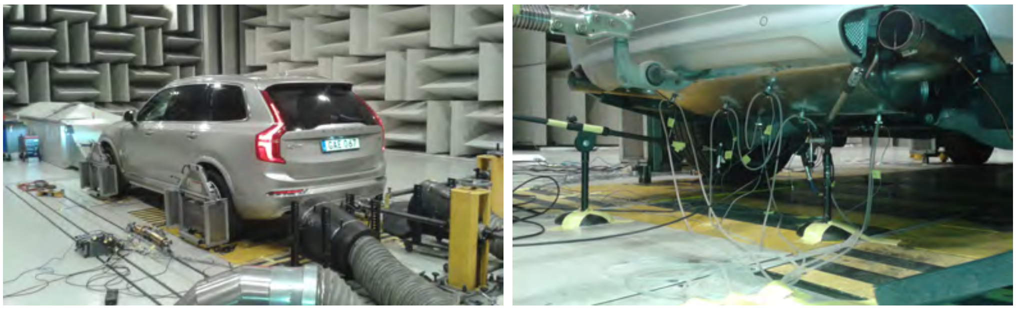

(a) Measurement car (b) Muffler with all sensors and attachments.

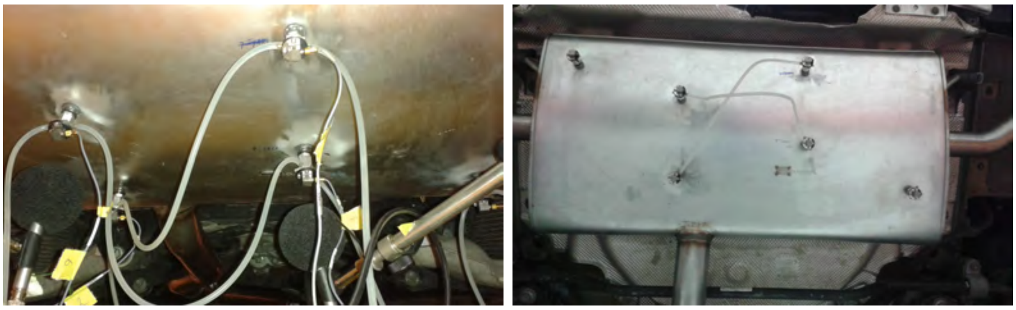

(c) One of the external microphones directly beneath an accelerometer. (d) Accelerometer mounting configuration without any attachments

(e) Close up of accelerometer mounting. (f) Coolant tank with submerged pump.

Figure 3.9.: Measurement setup used at VCC.

3.2.2. Accelerometer and microphone placement

Accelerometers were mounted only on the bottom facing side of the rear muffler due to mounting considerations. Six accelerometers were available, of which four were mounted in the same locations where the measurements under cold conditions were conducted. The remaining two were mounted at appropriate locations to cover the remaining uncovered inter-baffle areas to give a final configuration shown in Figure 3.10b. However, since the muffler surface was known to reach temperatures in excess of 800 K, the accelerometers could not be mounted directly on to the surface of the muffler. In order to circumvent this problem, the accelerometers were mounted on water-cooled aluminium adapters. The adapters of all the accelerometers were a part of a network connected to a coolant tank containing the pump. The effect of the noise originating from the water pump in the cooling tank was been minimized by covering the tank with a foam sheet. These threaded adapters were bolted on to the muffler using M8 bolts welded on the chosen accelerometer location points. This mounting arrangement is shown in Figure 3.9e

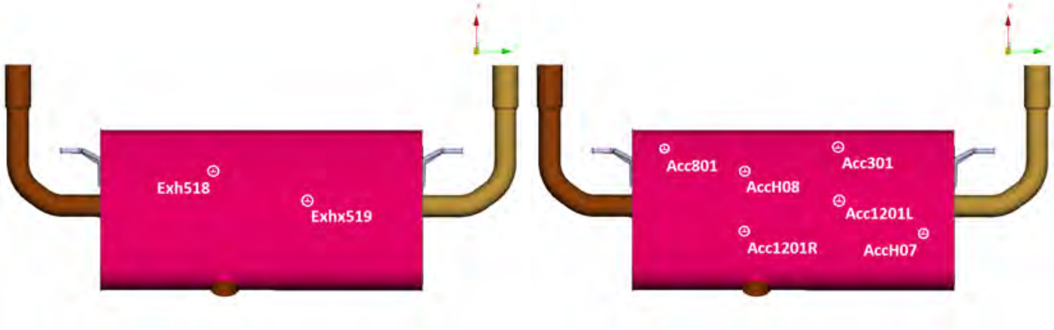

(a) Microphones

(b) Accelerometers

Figure 3.10.: Sensor locations for hot condition measurements.

Microphones to be placed in the nearfield were chosen to be two in number. Their quantity and location were constrained by the amount of space available, proximity to the orifice noise and the ground and number of channels available in the front end. Similar to the cold condition measurements, these microphones were placed vertically beneath chosen accelerometer positions as shown in Figure 3.10a. The vertical distance to the accelerometers was decreased from 250 mm in the cold condition measurements to 100 mm keeping in mind ground reflections and existing standards for nearfield microphone placement at VCC.

3.2.3. Engine operating conditions

The engine was operated under various loading conditions and RPM sweeps as shown in Table 3.1. The number of crosses indicate the number of trials performed for each case.

The traction force, controlled by throttle position, was maintained partially open (POT) at the one-third and two-thirds positions and a wide open position (WOT) which was found to generate a more variable range of traction force than the POT positions. The higher RPM range sweep between 4000 to 5000 RPM was not performed for the WOT

RPM / *Throttle*	*3000-4000 RPM*	*4000-5000 RPM*	*1250-5700 RPM*
1/3 *POT*	× × ×	× × × ×	× × × ×
2/3 *POT*	× × × ×	× × ×	× × × ×
WOT	× × ×	-	× × × ×

Table 3.1.: Engine operating conditions

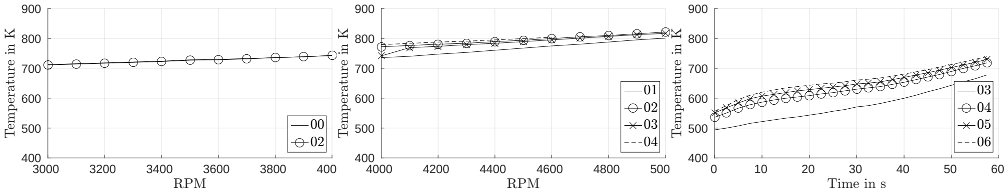

(a) 1/3 POT, 3000-4000 RPM (b) 1/3 POT, 4000-5000 RPM (c) 1/3 POT, 1250-5700 RPM

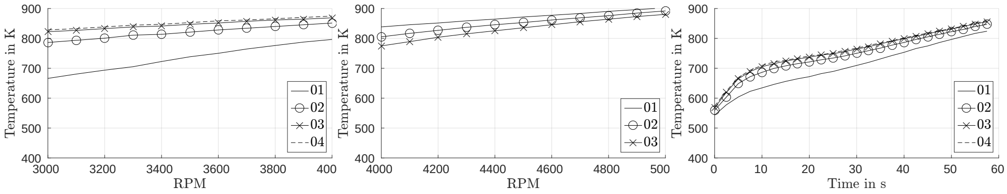

(d) 2/3 POT, 3000-4000 RPM (e) 2/3 POT, 4000-5000 RPM (f) 2/3 POT, 1250-5700 RPM

(g) WOT, 3000-4000 RPM (h) WOT, 1250-5700 RPM

Figure 3.11.: Exhaust temperature variation for different engine operating conditions. Trial numbers shown in the legend.

position as the muffler became very hot. This was due to the slow nature of the 1000 RPM sweep which maintained the engine at a higher RPM for much longer than the larger sweep range of 1250-5700 RPM.

In order to get a rudimentary estimate of the temperature changes associated with such widely varying engine operating conditions, a temperature sensor was placed at the right side exhaust orifice. The temperature plot corresponding to each trial shown in Table 3.1 is shown in Figure 3.11. The trials selected here are those for which there is another trial with a very similar temperature sweep profile as seen in Figure 3.11. This indicates that running conditions were stabilised to an extent. In the cases when no pairs of temperature profiles were similar to each other such as in Figure 3.11e, the trial with the median temperature profile was selected.

4. Simulation methodology

Any simulation procedure comprises of the following tasks:

- CAD model generation
- Meshing
- Setup physical model
- Apply boundary conditions
- Postprocessing
- Validation

The first four tasks of the simulation procedure will be dealt with in this chapter while the last two will be dealt with in the later chapters.

4.1. CAD model generation

Three dimensional solid CAD models of the mufflers and its pipe attachments were available at VCC. These models were used for the interior space enclosed by the muffler as well as the parts of the muffler in contact with the external air. As for the structure itself however, 3D shell models of the mufflers were required since the mufflers were made of sheet metal and a shell model is conducive for performing vibroacoustic analysis upon it. This transformation was done by extracting the middle surface skin from the mufflers using ANSA[14] as a preprocessor. Appropriate thicknesses for each part was also automatically assigned.

4.2. Meshing

Once the CAD models were ready, the interior of the muffler, the muffler itself and an external region around the muffler were meshed.

4.2.1. Muffler interior

A surface mesh along the interior facing parts of the muffler including the connection pipes was manually created with triangular elements of variable size. The perforated regions of the muffler were meshed finer than the remaining regions of the muffler interior. This generated cavity was meshed with tetrahedral elements of variable size with a maximum size of 40 mm which fulfilled six elements per wavelength up to around 1400 Hz. In the case of the front muffler, the muffler interior was meshed into two separate volumes; one for the region containing the porous material and the other without any, as shown in Figure 4.1.

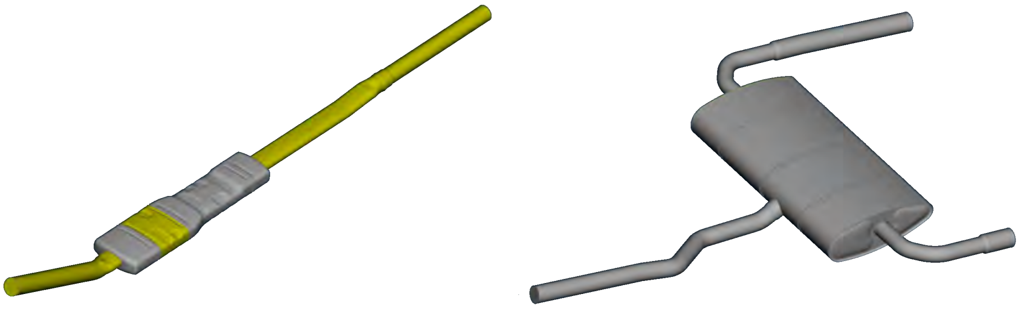

(a) Front muffler.

(b) Rear muffler.

Figure 4.1.: Interior fluid cavity mesh. All compartments not pink in color are the compartments containing the porous material.

4.2.2. Muffler exterior

Similar to the previous step, a closed wrap mesh of triangular elements was generated around the muffler, but this time using the externally facing parts of the muffler on the outer side. Since the total radiating area as well as the flat radiating area of the mufflers, both front and rear, were much greater than those of the pipes, the pipes were excluded from interacting with the exterior medium. This external wrap was therefore limited to cover only the muffler and projected outwards to create an annular cavity surrounding the muffler. This cavity was then meshed with an identical maximum element size as the muffler interior.

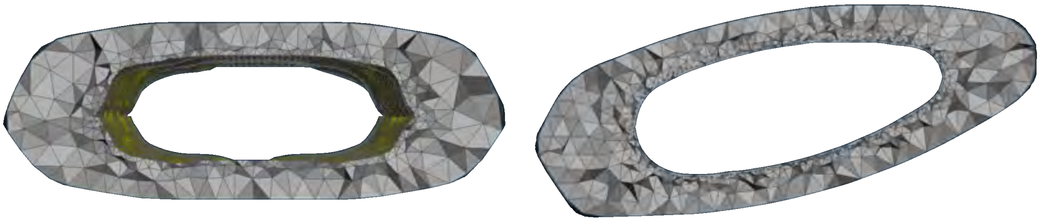

(a) Front muffler.

(b) Rear muffler.

Figure 4.2.: Exterior fluid mesh. The infinite element envelop surrounds the external wrap.

4.2.3. Muffler structure

The muffler shell structure, unlike the fluid cavity meshes, was meshed differently for different mufflers. The areas of the rear muffler connected to each other like the flanges and the perforated areas, which need to be resolved better, were meshed with finer quadrilateral elements than the rest of the structure. This kept it within the six elements per bending wavelength limit for the sheet metal material up to 2000 Hz. The different parts were assembled together with the help of various connections present in ANSA. With the exception of the baffle-outer shell connections on both mufflers, all the other connections between parts present in the shell model were modelled as Nastran RBE3[15] rigid body elements defined along a *Seamline* connection line available in ANSA. The nature of the baffle-outer shell connections on the other hand were not as well known, but whose influence on the radiated shell noise was seen to be significant. Therefore, different types of connections will be investigated and the results presented in the following chapter.

4.3. Setup physical model

A review of the available academic literature on shell radiated noise from mufflers conducted in the Chapter 1 revealed some of the common approaches to modelling the

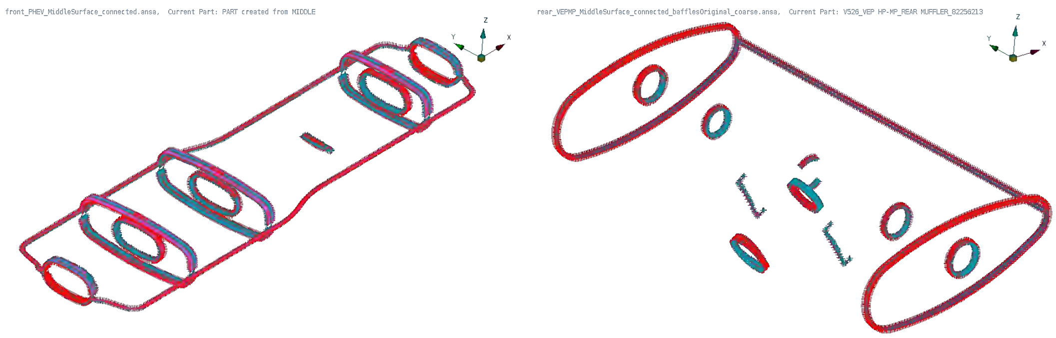

(a) Front muffler.

(b) Rear muffler.

Figure 4.3.: Connection curves and connection elements.

various components constituting a typical vibroacoustic system. Apart from the previously used approaches in modelling shell radiated noise, the primary factor guiding the choice of the modelling procedure for each of the above components was the commercial analysis software packages that were available at VCC. At the Noise and Vibration (N&V) Centre at VCC, MSC Nastran and MSC Actran were commonly used and therefore will also be used for all simulation purposes in the course of this thesis work. The domains pertaining to the components of a typical vibroacoustic system, particularly for the case of the automotive muffler are listed and the modelling procedures used for the same are described below.

(a) Front muffler.

(b) Rear muffler.

Figure 4.4.: Complete simulation setup. The points are the field points where acoustic quantities were evaluated. These points correspond to measurement locations.

4.3.1. Exterior acoustic domain

The exterior acoustic problem can be solved in many ways. Some of the commonly used approaches in academic literature are,

1. A BEM implementation using the structural displacements as velocity boundary conditions. This was found to be the most commonly used method.

2. SEA method[16].

However, FEM was chosen as the preferred modelling approach due to its prior tested worthiness at the N&V Centre at VCC where. Unlike in a BEM approach, the free field radiation condition must be modelled explicitly using an absorbing boundary condition. MSC Actran, which is a dedicated solver for acoustic problems was chosen to model the exterior acoustic radiation problem over the more generic FE solver MSC Nastran. It provides two ways of accomplishing this: Perfectly Matched Layers (PMLs) and infinite elements. In this thesis, infinite elements were chosen to model the non-reflecting acoustic or boundary conditions.

And for exterior acoustic radiation problems involving a stiff radiating surface and a light fluid, the assumption of a weak structure-acoustic coupling is standard practice[17]. With this assumption, the fluid-structure coupling term $\boldsymbol{Q}$ in the structural part of the (2.5) is ignored and the vibrations on the structure are independent of the exterior acoustic domain and simply become boundary conditions for the free field radiation problem. Since the muffler surface is made of stainless steel which is comparatively much stiffer than air, this assumption is valid and will be used further in the thesis. This was implemented using the *STAGGERED_SOLVER*[5] module on Actran. The weak coupling solution was compared to the strong coupling solution and verified to be a good approximation of the same (results not shown).

4.3.2. Structural domain

The structural domain of a vibroacoustic system was modelled using a conventional FEM approach. However, the MSC Nastran commercial software package was chosen for the structural analysis over MSC Actran for two main reasons. One of the reasons was the availability of a non-linear solver functionality, that was required to perform thermo-mechanical analyses on the muffler under hot operating conditions and to include surface contact connections between the baffles and the outer shell. The other reason was to perform a modal reduction of the structural model, ignoring all the eigenmodes above a chosen cutoff frequency, which was in this case, 2000 Hz. The mathematical formulation of this procedure is shown in Section 2.1.1. In order to perform a modal reduction, the eigenmode matrix, obtained from an eigenvalue analysis was required. Actran can perform a modal reduction procedure by using the eigenmode data from a Nastran *.op2* file, which has to be independently generated. Actran's *MODAL_ELASTIC* component module allowed the creation of a structural component in modal coordinates and to set the parameters for the modal reduction process. Thus the vibroacoustic analysis being performed will henceforth be referred to as the '*Hybrid*' approach where one of the two domains involved in a fluid-structure interaction problem is a modal model.

4.3.3. Acoustic-structure interaction

The acoustic-structure interaction was modelled using a FEM approach whose mathematical outline is described in Section 2.1. In Actran, the outer skin of the interior acoustic domain as well as the inner skin of the exterior acoustic domain were interfaced with the modal model of the structure using the *INTERFACE* component. This component was used to handle incompatible acoustic and structure boundary meshes. All the surfaces lying within a specified tolerance region around the surfaces, defined in the normal direction to the surfaces, were coupled. The following images show the quality of the mapping along the acoustic-structure interface, for the structure with both the exterior acoustic domain and the interior acoustic domain.

(a) Exterior acoustic domain interface

(b) Interior acoustic domain interface

The closer the index in the colorbar is to unity, the better is the projection in that region of the muffler. From Figures **??** and 4.5 it can be seen that the regions with poor coupling are only in the defilleted regions and constitute a small minority of the entire region involved in the acoustic-structure interaction and radiation. Therefore, the interface is assumed to be adequate.

4.3.4. Interior acoustic domain

The interior acoustic domain was modelled using the *ACOUSTIC* component available on Actran. In this component, damping was added in the form of a complex sound

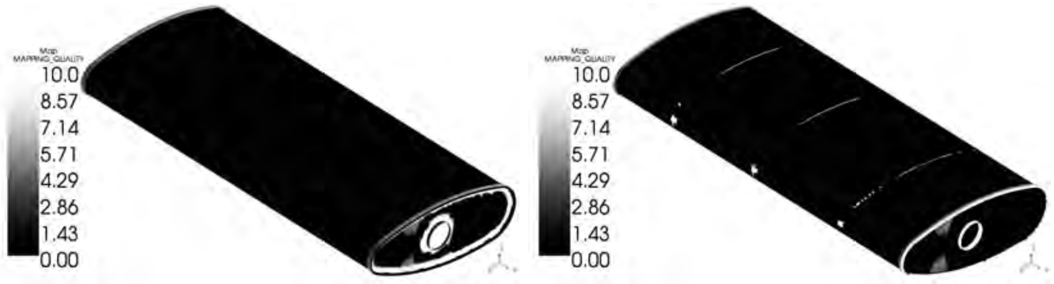

(a) Exterior acoustic domain interface (b) Interior acoustic domain interface

Figure 4.5.: Acoustic-Structure interface mapping quality - Rear Muffler.

speed and elevated average temperature conditions was added by specifying a mean sound of speed and a mean density of air. The damping loss in the air was obtained from the measurements as discussed earlier in Section 3.1.5. In case of the front muffler, the porous regions of the acoustic interior were modelled as equivalent fluids using the Actran component *DELANEY_BAZELEY*. The air and porous material domains can be seen clearly in Figures **??** and **??**. The porous material, is glass wool of uncertain material properties, the most influential property being Flow Resistivity.

In an alternative to the hybrid vibroacoustic model, the acoustic domain was also replaced with a modal model of the acoustic cavity using the *MODAL_ACOUSTIC* Actran component.

4.4. Apply boundary conditions

The application of accurate boundary conditions, that replicate the measurement setup, to the simulation model of the muffler system is an essential step towards validating it. Once the boundary conditions have been established within sufficient bounds of confidence, the influence of other model parameters on the system can be studied with greater certainty.

4.4.1. Structural boundary conditions

In the absence of an excitation on the structure, the boundary conditions on the muffler structure depend only on how the muffler has been mounted during the measurements. The mufflers, as seen in Chapter 3, were hung from the ceiling using ropes at some distance away from the muffler inlet and outlet. This implies that the structure as a whole including the pipes was freely suspended but the inlet pipe was fastened to the pipe coming from the loudspeaker. For the rear muffler, the bracket used to mount it on to the car was still welded to the endplates. This was accounted for by replacing the mount with a Nastran RBE2 multi-node element as shown in Figure 4.6a. The following figure shows the nodes on which Nastran Single Point Constraints (SPC1) have been imposed, corresponding to the inlet support location on the muffler.

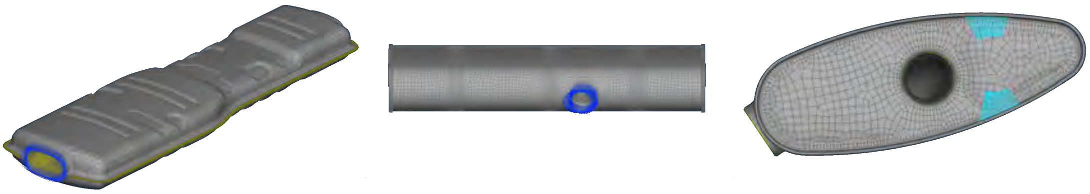
(a) Front muffler in- and outlet
(b) Rear muffler inlet pipe support
(c) Rear muffler hangar mount support

Figure 4.6.: Nodes on front and rear mufflers with prescribed displacement boundary conditions

4.4.2. Acoustic boundary conditions

The acoustic boundary conditions for the muffler's interior acoustic domain refers to radiation boundary conditions in the form of inlet impedance and outlet impedance along with the velocity of the incoming wave at the inlet. These quantities were applied at the locations shown in the following figures for the front and rear mufflers. These boundary conditions were applied in two ways to the simulation model.


(a) Inlet side
(b) Outlet side

Figure 4.7.: Application of radiation boundary conditions for the front muffler.

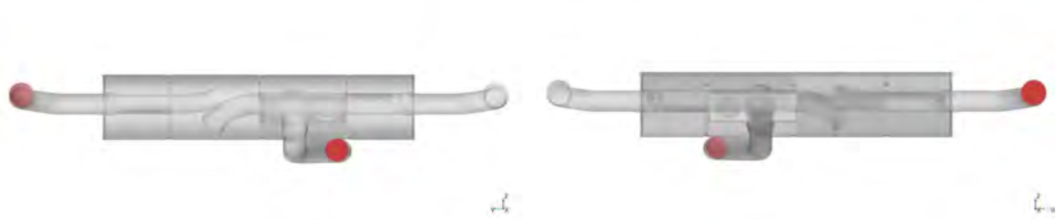

(a) Inlet side

(b) Outlet side

Figure 4.8.: Application of radiation boundary conditions for the rear muffler.

Boundary conditions obtained from measurements

Applying these to the simulation model allow a direct comparison with measurements. These quantities were derived from the measurements using the two microphone technique described in Section 2.3.2 and plotted below.

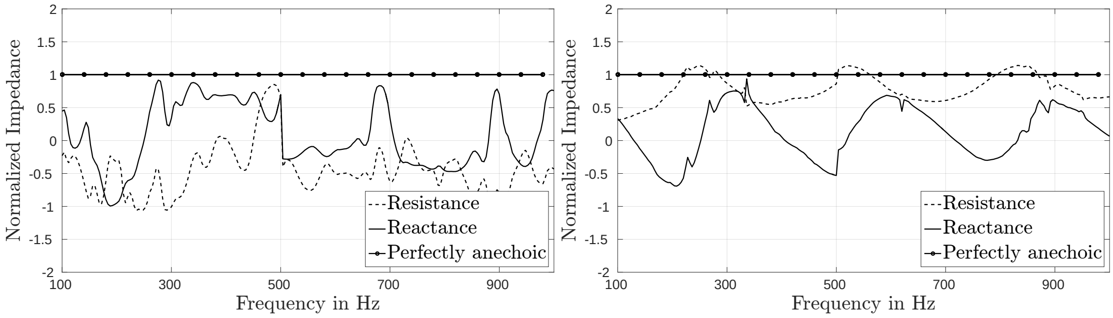

(a) Front muffler termination impedance

(b) Rear muffler

Figure 4.9.: Exit or termination impedance normalized w.r.t plane wave impedance.

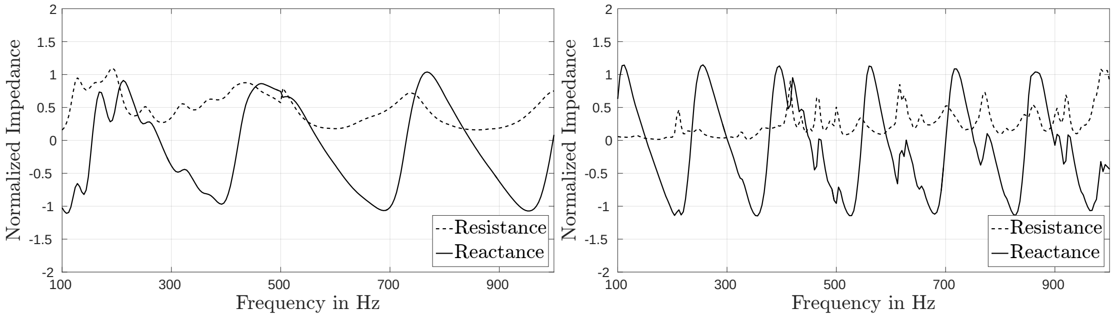

(a) Front muffler

(b) Rear muffler

Figure 4.10.: Inlet impedance normalized w.r.t plane wave impedance.

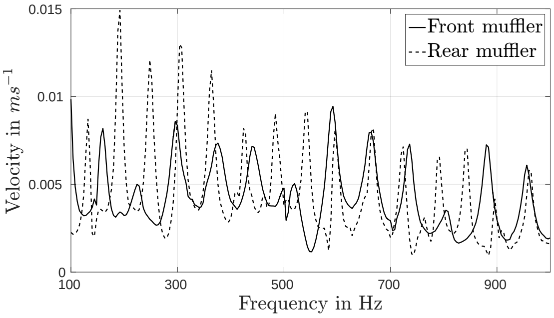

Figure 4.11.: Incoming wave velocity spectrum

Analytical boundary conditions

These boundary conditions were applied using Actran's duct mode coupling component, *MODAL_BASIS*. In this case, semi-infinite ducts were assumed to be attached to the muffler inlet and exit sections and a wave of unit amplitude was assumed to excite the system at the inlet. This formulation allowed the calculation of the true transmission loss value of the muffler in the presence of a perfectly anechoic termination. Since this boundary condition was independent of the measurements, it was used to verify the veracity of the measurements themselves.

In addition to *MODAL_BASIS* analytical boundary conditions, a unit velocity input was applied as the only boundary condition at the inlet during a modal coupling procedure.

4.4.3. Temperature conditions

The material properties of air inside the muffler cavity as well as ferritic steel of the muffler structure vary with temperature. Accounting for this variation became especially important in modelling the behaviour of the structure when the temperature change was significantly large across an RPM sweep, as seen in Figures 3.11. The variation can be adequately accounted for only when the spatial temperature distribution and temporal temperature variation for the entire system is available. For the measurements conducted at VCC however, the only temperature data that could be recorded was at the orifice of the tailpipe. This meant that the exact behaviour of the muffler system could not be accurately modelled and the ambient conditions present during the measurements cannot be replicated in the simulations. Therefore, an estimation of the actual temperature conditions and variation, based on prior measurements conducted at VCC was made and presented in Figure 4.13. The spatial temperature of the muffler shell is distributed

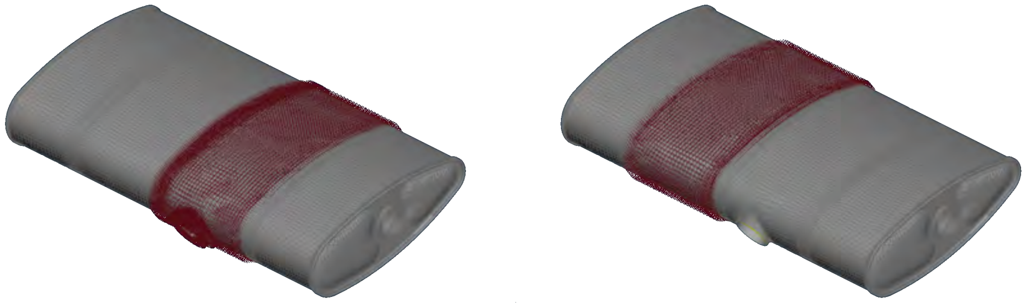

(a) Inlet chamber

(b) Middle chamber

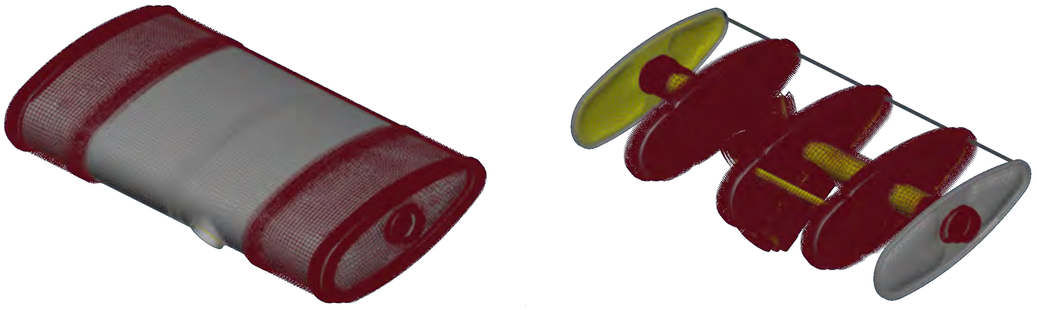

(c) Outer chamber

(d) Muffler interior

Figure 4.12.: Temperature distribution on the rear muffler shell.

in the manner shown in Figure 4.12. For this model, the air temperature was assumed to be uniform throughout the system and equal to the temperature at the orifice.

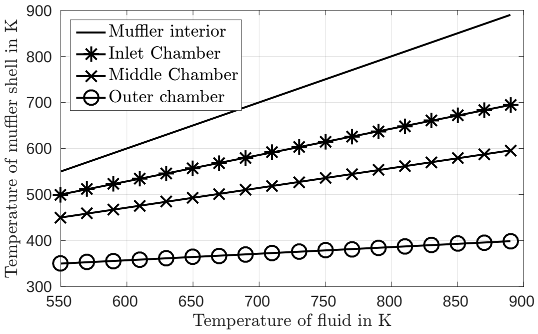

Figure 4.13.: Variation of temperature of various muffler shell regions with fluid temperature.

5. Simulation and measurement results and discussion

The results obtained from running the simulation model setup in Chapter 4 and the measurement setup in Chapter 3 are presented in this chapter. The following approaches have been used to investigate the shell noise characteristics of the mufflers, each with its own application:

1. **Experimental investigation - Loudspeaker input**
   The influence of the muffler outlet pipe termination on both mufflers and the influence of spot welding the baffles of the rear muffler on the radiated shell noise and surface vibrations are studied experimentally in this section. This establishes the data against which simulation models are validated.

2. **Fluid cavity model**
   The measured acoustic boundary conditions presented in Figures 4.9 and 4.10 are verified and the measured transmission loss are examined through a purely acoustic analysis of the fluid cavity of the muffler.

3. **Vibroacoustic model**
   Complete vibroacoustic analyses are performed for different models of the baffle-outer shell connections for the rear muffler and front muffler. In the case of the front muffler, the influence of a bracket previously installed specifically to reduce shell noise is studied. The simulation results are validated using measurement data presented in the preceding section.

4. **Modal coupling model**
   An alternative and simplified analysis approach, the modal coupling model allows viewing the shell noise problem from the perspective of the fluid cavity eigenmodes. The results are once again validated against measurement data from Section 5.1.

5. **Experimental investigation - Engine operating conditions**

Shell noise measurements and surface vibrations are performed on the muffler, which is mounted on the car, under controlled engine running conditions.

6. **Elevated temperature simulation models**
The validated simulation models from the preceding sections are used to simulate the effects of elevated temperature levels. These predictions are then compared to the measurement data obtained for engine operating conditions.

5.1. Experimental investigation - Loudspeaker input

5.1.1. Coherence

The coherence of the measured signals at a randomly selected accelerometer and external microphone position with respect to the reference signal is presented here to examine the validity of the measurements.

The coherence spectra for the rear muffler seen in Figure 5.1c and 5.1d is not smooth and has a lot of steep dips. This is typical for a highly resonant system such as a muffler free of any porous damping material. On the other hand, the coherence spectra for the front muffler in Figures 5.1a and 5.1b are smoother with fewer variations. It can also be seen from Figures 5.1b and 5.1d that, the coherence of the measured microphone signals for the frequency region between 100-300 Hz is noticeably worse than the rest of the frequency range for both the front and rear mufflers. One major reason for this behaviour could be the bad signal to noise ratio due to the low radiation efficiency of the sheet metal structure in this frequency region. It could also be attributed to the contribution of spurious reflections arising due to imperfect anechoic conditions around the microphones in the presence of extraneous reflecting surfaces.

5.1.2. Transfer functions

From the transfer functions (TFs) in Figures 5.2a and 5.2b, it is seen that a difference between a rigid and foam plug (anechoic) termination for the front muffler exists only below 500 Hz with respect to the external microphone and accelerometer spectra. The clear absence of peaks in the case of the foam plug termination is seen at around 420 Hz and a lower peak at 570 Hz. On the other hand, a sharp peak at around 200 Hz is seen only in the case of the foam plug termination.

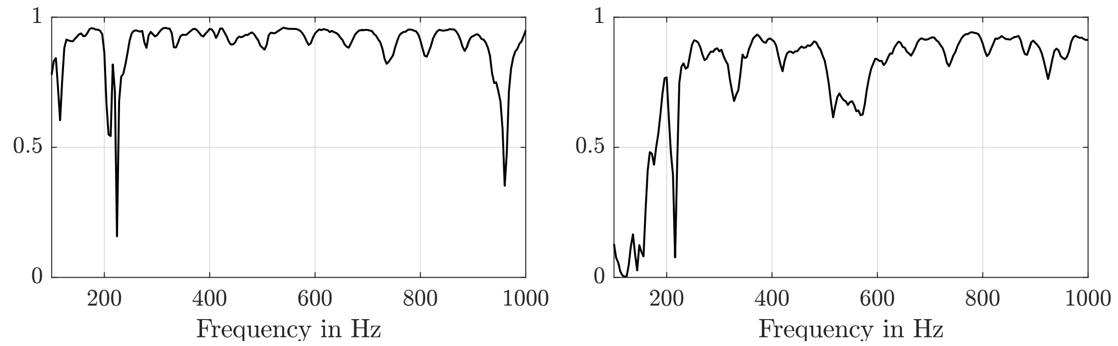

(a) Accelerometer - Front muffler

(b) Microphone - Front muffler

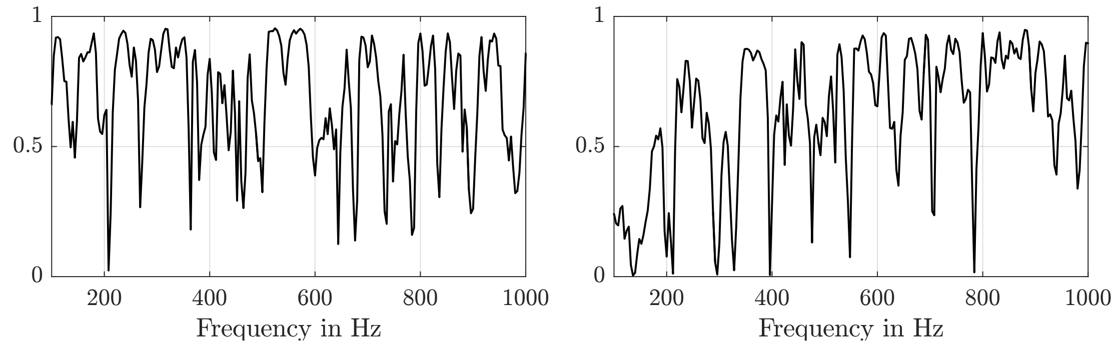

(c) Accelerometer - rear muffler

(d) Microphone - rear muffler

Figure 5.1.: Coherence spectrum for measured signals.

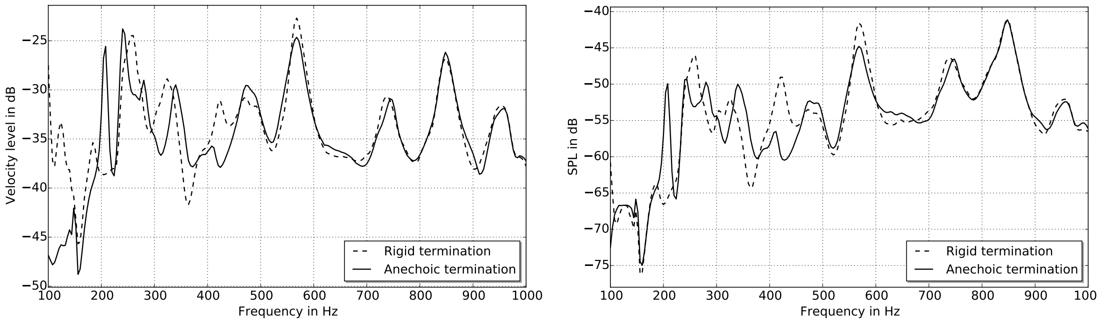

(a) Average of 9 accelerometers

(b) Average of 6 microphones

Figure 5.2.: Measured TFs for the front muffler.

As for the rear muffler, the anechoic and rigid terminations seem to influence the velocity and transfer functions plots only to a limited extend. The shell noise phenomenon is therefore not sensitive to the acoustic boundary conditions on the muffler, atleast for this particular muffler and measurement conditions. But in the case of the stock muffler,

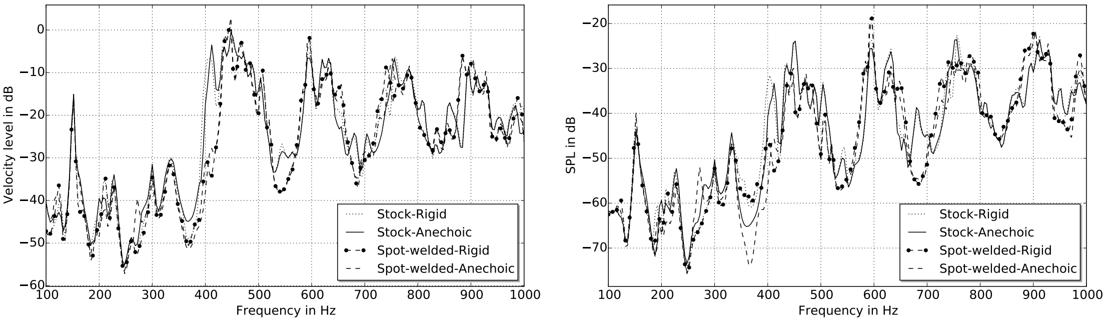

(a) Average of 9 accelerometers

(b) Average of 6 microphones

Figure 5.3.: Measured TFs for the rear muffler.

there is a significant peak at 410 Hz that is missing in the spot welded muffler's TF. From the individual sensor transfer function plots shown in Figure B.3 in the Appendix B.1, it is also seen that this peak does not occur at the two accelerometers mounted between a baffle and one of the endplates. The peak is therefore characteristic of the central regions of the muffler between the two outer baffles. The source of this peak will be investigated further in a later section using a simulation model. Finally, it can also be noted that the shape of the surface velocity level plots correspond very closely with the radiated SPL plots for all cases.

5.2. Fluid cavity model of muffler

5.2.1. Influence of acoustic boundary conditions

A fluid cavity model from Section 4.2.1 alone is considered and the following acoustic boundary conditions are applied to it:

1. Analytical boundary conditions at the in- and outlet of the muffler system. Coupling of semi-infinite ducts simulating non-reflecting conditions with an inlet pressure wave of unit amplitude.

2. Boundary conditions at the in- and outlet extracted from measurements through the two-microphone method. These include normalized radiation impedance boundary conditions at the inlet and outlet and inlet velocity boundary conditions.

3. A combination of the first boundary condition at the outlet and the second boundary condition at the inlet.

All the fluid cavity models are simulated under room temperature conditions to reflect the measurement conditions. The transmission loss of the front and rear mufflers are then computed under the influence of these boundary conditions. The obtained results are plotted below alongside the transmission loss computed directly from the measurements.

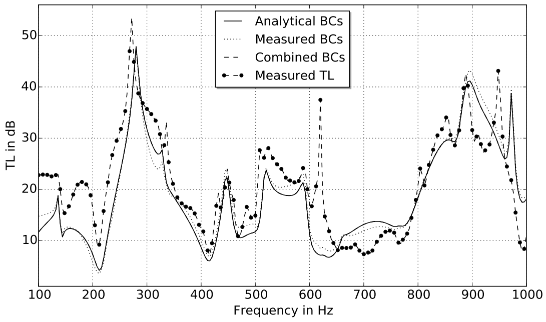

Figure 5.4.: Axial transmission loss for rear muffler

In Figure 5.4, the measured transmission loss spectrum closely follows the theoretical transmission loss spectrum. Furthermore, the change in boundary conditions at the inlet does not vary the computed transmission loss from the theoretical value by more than 3 dB. Here, the replacement of the analytical boundary condition with the measured boundary condition has not altered the transmission loss plot by much. This indicates that the anechoic nature of the foam plug termination for the rear muffler is accurate enough for use in further analyses.

A similar procedure performed for the front muffler however deliver similarly promising results. The transmission loss and the foam plug termination impedance calculated from the measurements for the front muffler turned out to be erroneous (not presented here). Therefore, all further simulations of the radiated shell noise for the front muffler are conducted for the case of a rigid outlet termination and compared with the rigid termination measurements.

5.2.2. Determination of flow resistivity

As mentioned earlier, the material properties of the glasswool inside the front muffler are unknown. However the Delany-Bazley model uses the flow resistivity of a porous material as the sole parameter. Therefore, the effect of flow resistivity on the transmission loss of the front muffler is presented in this section. The simulated transmission loss model employs semi-infinite ducts at the inlet and outlet. This simulated transmission loss plot acts as a regression model for the measured transmission loss. The fit between the regression curve (simulated transmission loss) and the measured transmission loss plot will be used to determine a nominal value of flow resistivity for future analyses. While the initial guess of the flow resistivity was 50000 Nsm^{-4}, the optimised value is found to be 68161 Nsm^{-4}. Using Equation (2.16), the frequency limits of validity for this model are found to be 563 Hz and 56.33 kHz.

5.2.3. Eigenvalue analysis

An eigenvalue analysis of the fluid cavity of the rear muffler is performed and the results are presented in this section. Here, the internal duct resonances are ignored and only the global eigenmodes are presented in Figure 5.5.

It can be observed from Figure 5.3 that the highest peaks in the TFs of the rear muffler each correspond to a distinct fluid cavity mode, i.e the modes at 417 Hz, 456 Hz, 618 Hz, 766 Hz and 893 Hz. This indicates that the shell noise characteristics are partly determined by fluid cavity modes at room temperature. The actual contribution of each of these modes to the shell noise is presented in a later section.

5.3. Vibroacoustic model

All the transfer functions shown in this section are averaged across all microphones and accelerometers and the results at the individual microphones and accelerometers are shown in Appendix B.

5.3.1. Rear muffler

In order to understand the baffle-outer shell connection behaviour, four different structural models are investigated for the vibroacoustic analyses of the rear muffler, each differing in the kind of connection between the baffles and the outer shell.

1. RBE3 Nastran force distribution elements all along the flange of the baffle. This analysis will be designated as '*RBE3*'. This is the most straightforward connection

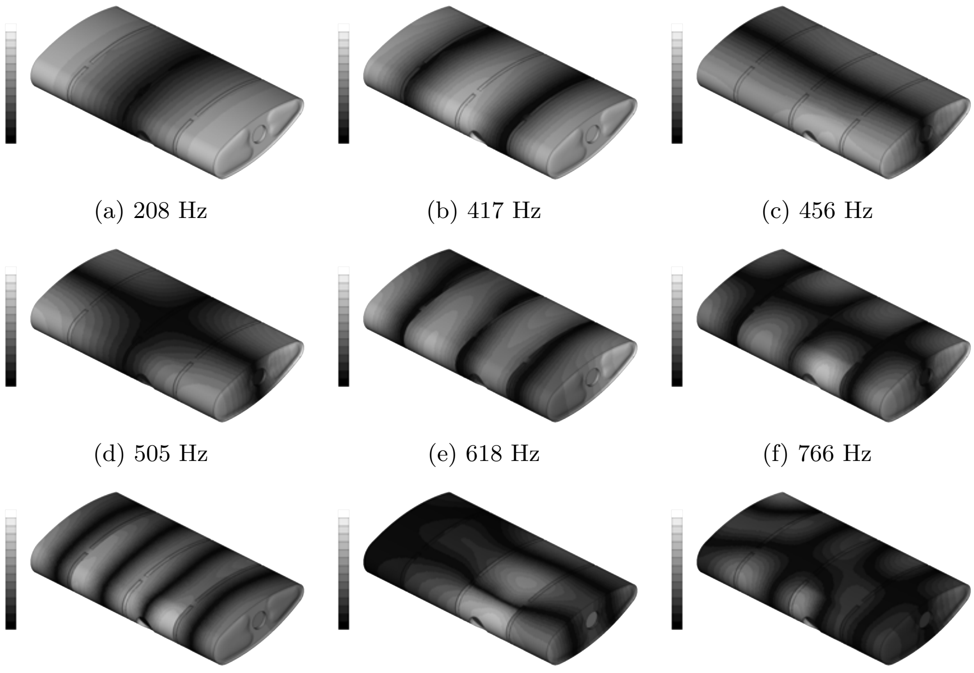

(a) 208 Hz (b) 417 Hz (c) 456 Hz

(d) 505 Hz (e) 618 Hz (f) 766 Hz

(g) 863 Hz (h) 893 Hz (i) 979 Hz

Figure 5.5.: Eigenmodes of rear muffler

for a rigid assembly of different components and will be used as a baseline comparison case for the following three models. In this model and the following one, the CAD data from the baffles have been modified to flatten the baffle flanges, as they are presumed to be once the assembly of the muffler is complete.

2. RBE3-CBUSH-RBE3 Nastran elements all along the flange of the baffle. This analysis will be designated as '*RBE-CBUSH-RBE3*'. The stiffnesses of the CBUSH elements are optimised for the best fit and found to be 50 kN/mm in the direction perpendicular to the shell and 20 kN/mm in the direction perpendicular to the baffles. These values depend on parameters such as the distribution of the CBUSH elements, width of the RBE3 elements, mesh size, etc. Among the three models used, this is the only one with easily tunable parameters and this feature is used to understand the nature of the baffle - outer shell connections better.

3. Automatically identified contact regions between the baffle and the muffler outer shell through the Sol 400 solution module. This analysis will be designated as '*Contact*'. The thus identified contact area can be seen in Figure 5.6. This model is the only one which uses the original CAD data of the baffles with the unmodified

flanges. The coupling between the baffle and the outer shell is generated organically from the solution to the contact problem unlike the previous two models. As such, this model is the closest to reality from a physical point of view and is used for all the thermomechanical analyses.

4. Finally, in the model designated as ‘*NoConn*’, the baffles are simply left unconnected to the outer shell.

Figure 5.6.: Contact region identified by Sol 400.

The transmission loss (TL) and the transfer functions (TF) of the surface velocity and radiated noise will be presented and compared in the following sections for the aforementioned analyses.

Transmission loss

The theoretical TL computed using a fluid cavity model is used as a baseline simulation alongside the measured TL in the following plots.

From Figures 5.7, it can be seen that the theoretical TL computed using a fluid cavity matches the measured TL better than the vibroacoustic models. The ‘*Contact*’ model

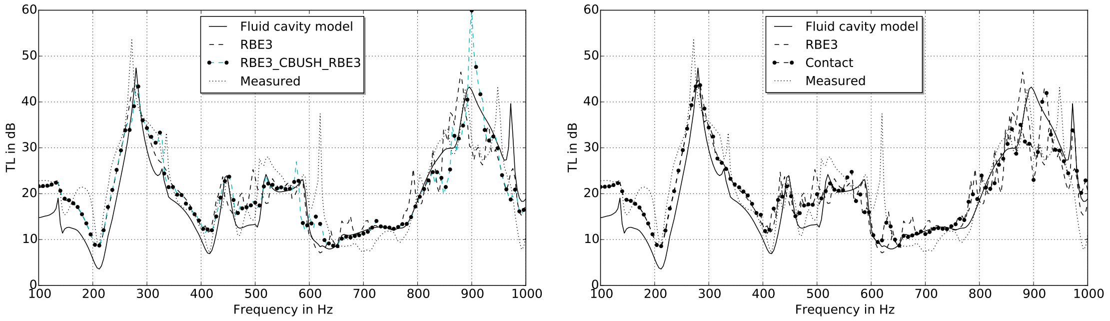

(a)

(b)

Figure 5.7.: Transmission loss comparison plots for the rear muffler.

comes closest to the measured TL and theoretical TL, especially above 800 Hz. The '*RBE3-CBUSH-RBE3*' model demonstrates slightly worse fit to the measured TL compared to the other models. The TL characteristics of the rear muffler are therefore dependent on the baffle-outer shell connections. The appropriate choice of this connection will be explored in greater detail in the following section.

Transfer functions

Similar to the measured TFs, the simulations too show a high correspondence between the surface velocity levels and radiated SPLs. Overall however, the fit to the measured TFs is acceptable within the frequency range.

From the Figures 5.8, it can be seen that both the '*RBE3-CBUSH-RBE3*' and '*Contact*' models fit the measured TFs better that the '*RBE3*' model, although all three models underestimate the response at frequencies below 400 Hz. This indicates that the '*RBE3*' connections are too stiff and the structure is actually more compliant in this frequency range. This is made even clearer from Figure 5.8a and 5.8b where the response of the model below 400 Hz is much closer to the measured response compared to the other models. However, the sharp increase in the levels of the TF plots seen at around 400 Hz is absent in the '*NoConn*' model and only moderately captured in the '*RBE3-CBUSH-RBE3*' model. Further, the fit with the measurement TFs worsen at other frequency ranges for the '*RBE3-CBUSH-RBE3*' and '*NoConn*' models compared to the other two models. Therefore, these two models are not considered for further analysis. But it can be concluded that the baffle-outer shell connections noticeably influence the overall shape and levels of the TF plots.

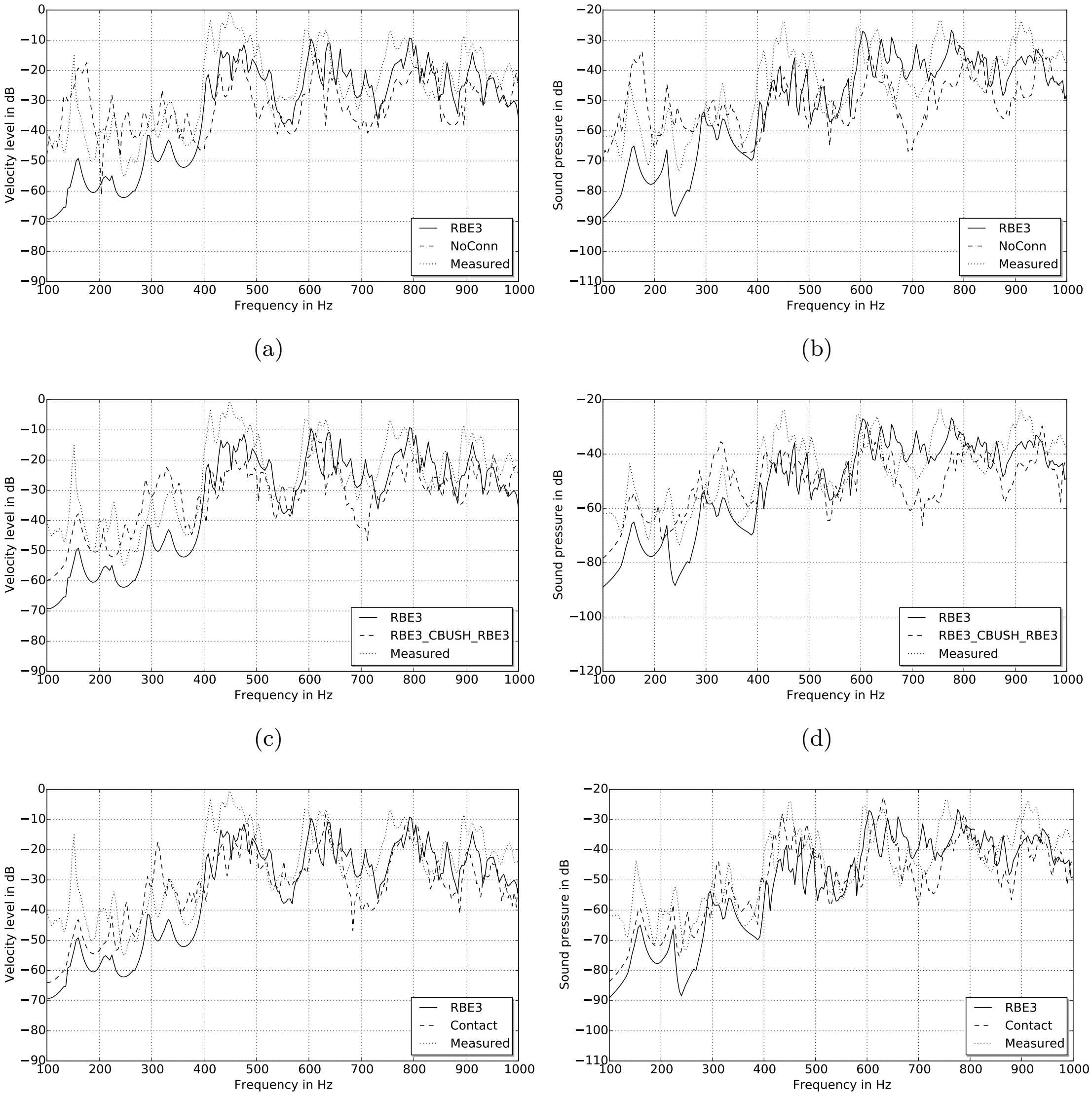

(a) (b)

(c) (d)

(e) (f)

Figure 5.8.: TF comparison plots for the stock rear muffler. SPL TFs are on the right and surface velocity TFs are on the left.

From Appendix B.2, it is seen that the difference between the '*RBE3*' and '*Contact*' models is not very noticeable for the accelerometer positions lying between the endplates and the outermost baffles. This strengthens the conclusion from Section 5.1 that the baffle-outer shell connections mostly affect the central portion of the muffler between the outermost baffles where the largest unsupported areas of the muffler are located. Finally, it can be seen that the '*Contact*' model fits the measured SPL TF between

400-500 Hz and 600-650 Hz better than the '*RBE3*' model but the same cannot be said for the surface velocity level TFs. A possible reason for this discrepancy is explored in the following section.

Structural eigenmodes

Figure 5.9 shows some of the modes in the 400-500 Hz frequency region for the two different structure models to examine what might be causing the discrepancy mentioned in the previous section. An animation of the modes presented here shows more clearly how the modes of the 'Contact' model have larger areas of the muffler shell vibrating in phase compared to the modes of the 'RBE3' model. Therefore these modes radiate more efficiently.

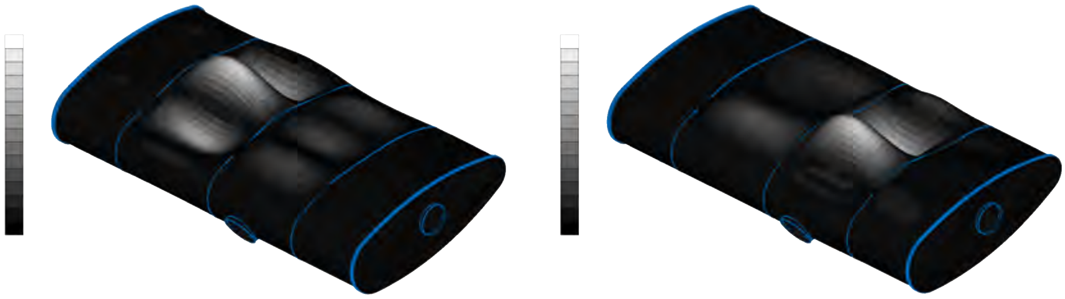

(a) '*RBE3*' model at 406 Hz (b) '*RBE3*' model at 470 Hz

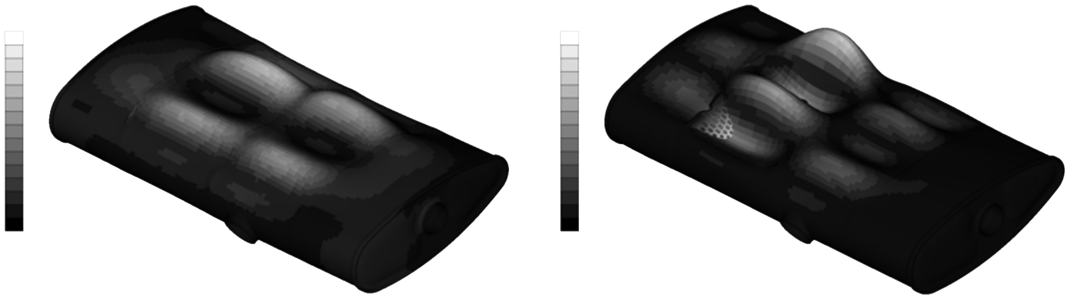

(c) '*Contact*' model at 435 Hz (d) '*Contact*' model at 460 Hz

Figure 5.9.: Structural eigenmodes of the rear muffler.

The mode shown in Figure 5.9a at 406 Hz is the first flexible body eigenmode of the outer shell. There is another mode with a similar modeshape but on the other side of the muffler at 407 Hz. The close proximity of these modes to each other and to the second fluid cavity mode at 417 Hz could explain the peak visible in the stock muffler at around 410 Hz discussed in Section 5.1. On the other hand, the eigenmodes of the

'Contact' model whose overall response, though similar to the 'RBE3' model, does not have similar modeshapes, many in number, near the fluid cavity mode. Thus, it can be concluded that the spot welds in the modified muffler modify the baffle-outer shell connection just enough to prevent the coupling of the first fluid cavity mode with the first flexible body mode to generate the peak.

5.3.2. Front muffler

Since the only termination considered for the front muffler is the rigid termination, a transmission loss is not defined and therefore only the surface level and SPL TFs will be studied. The following models for the front muffler are explored:

1. Fluid models. All fluid models are coupled with the '*Flange RBE3*' structural model for vibroacoustic analyses.
    a) Front muffler interior cavity filled with glasswool as it is in the measurement specimen. This model is designated as '*Glasswool*'.
    b) Front muffler interior cavity is devoid of the glasswool present in the measurement specimen. This model is designated as '*Empty*'.
2. Structural models. All structural models are coupled with the '*Glasswool*' fluid models for vibroacoustic analyses.
    a) RBE3 Nastran force distribution elements all along the flange of the baffle. This analysis will be designated as '*Flange RBE3*'.
    b) RBE3 Nastran force distribution elements at only the slots provided for weld connections between the baffle and the outer shell. This analysis will be designated as '*Slot RBE3*'.
    c) Muffler structure without a previously installed Z-bracket intended to cope with shell noise, whose baffle connections are as per the first model.

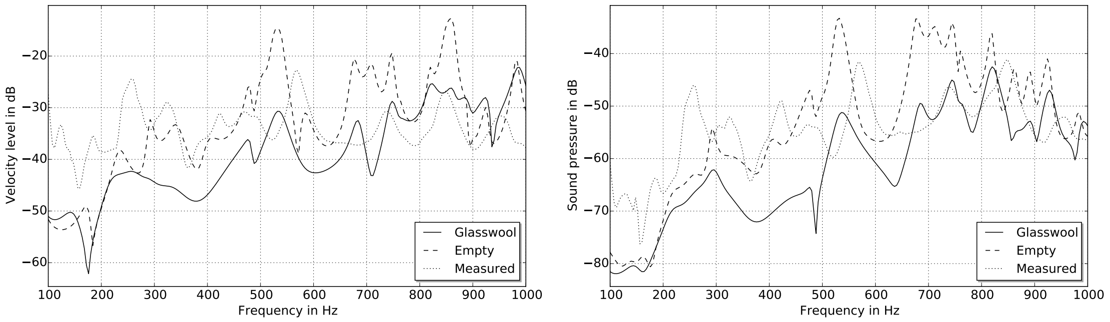

(a) Averaged surface velocity levels (b) Average SPL levels

Figure 5.10.: TFs of the front muffler - Influence of porous material.

Fluid models

From Figure 5.10, it can clearly be seen that the presence of the porous glasswool material in the muffler causes a significant effect on the surface velocity levels and the radiated SPL from the front muffler. The presence of glasswool reduces both quantities in the range of 10-20 dB depending on the frequency. However, it can be observed from Figure 5.10a that the behaviour of both models converge below a frequency of about 200 Hz and above a frequency of about 930 Hz. This observation is an indicator of the frequency region of the the porous material's influence with respect to shell noise TFs.

Structural models

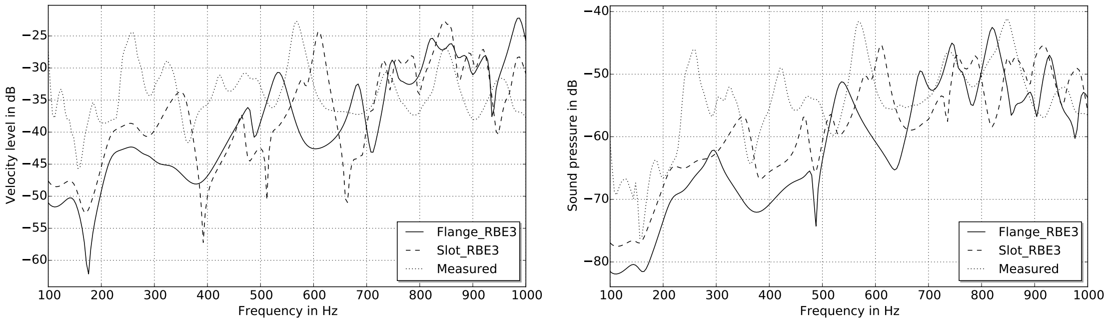

(a) Averaged surface velocity levels (b) Average SPL levels

Figure 5.11.: TFs of the front muffler - Influence of baffle connections.

From the Figures 5.11, it can be seen that the simulated transfer functions have a very poor fit to the measured transfer functions for both the '*Flange RBE3*' and '*Slot RBE3*' models. The fit however does improve above 700 Hz. To investigate the causes of the poor fit, the following attempts were made:

- Flow resistivity of the porous material was varied. A decrease in the flow resistivity lowers the lower frequency limit of validity of the Delany-Bazley equivalent model as calculated in Section 5.2.2.
- Gaps were introduced around the baffle to imitate leakages.
- Different models for simulating the porous material as an equivalent fluid were implemented.

However none of the attempted measures was found to be successful in improving the fit significantly. So, while the causes of this bad fit remain unknown, it can be reasonably attributed to one or more of the following reasons,

- The skeleton of the porous glasswool could be elastic and thus unaccounted for by the equivalent fluid models. This provides additional structure borne paths for the propagation of vibrations. An indication of this can be seen in the structural modal damping ratio plots and the fluid damping loss factor plots for the front and rear mufflers in Figures 3.8a and 3.8b. There, the damping curve shows a deviation from what is typical for a lightly damped sheet metal structure, exemplified by the rear muffler, between the frequencies 200-750 Hz. This matches well with the fact that the fit to the measured TFs improves slightly above 700 Hz, at which point the influence of skeleton-borne vibration is perhaps lower.
- Geometric and material anisotropy could be present in the porous glasswool. Given the constant heat expansion and contraction suffered by the porous glasswool throughout its working cycle, it is possible that the porous material is unevenly distributed or has air gaps or other such breaks in the isotropy of the simulation models.

As an additional investigation into the factors influencing shell noise in the front muffler, the effect of installing a Z-bracket between the inner perforated pipe and the outer shell is studied in Figures 5.12. In both cases, the entire flange of the baffle is modelled in Nastran to be connected to the outer shell ('*Flange RBE3*') and not just at the slots. It can be seen that the Z-bracket only influence the shell noise behaviour in the frequency range 400-600 Hz, shifting the peak in the TFs higher by about 80 Hz when it is installed. This corroborates well with previously done measurements at VCC and confirms that the shell noise model, though not effective at predicting the overall level and shape of

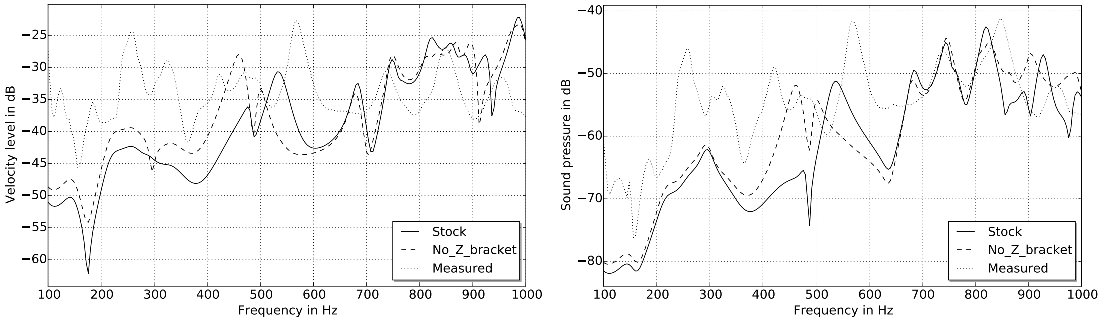

(a) Averaged surface velocity levels

(b) Average SPL levels

Figure 5.12.: TFs of the front muffler - Influence of Z-bracket.

the TFs, it can be used reliably to compare two different models.

5.4. Modal coupling model

The modal coupling model performs separate eigenvalue analyses on the structure and the fluid cavity and then couples the two modal models through a direct frequency response. Due to the correlation between the surface velocity and SPL plots, the free field radiation problem is not considered for this method. Since the acoustic boundary conditions are seen to only marginally affect the shell noise behaviour as seen in Figures 5.3, this method can be reasonably expected to fit the measured TFs. In this method, all the modes upto 2000 Hz in both the structure and fluid models have been included for the analysis. This model is intended to be used as a replacement for the hybrid vibroacoustic model to perform faster analyses. Since the ‘Contact’ model alone can accommodate the potential modification in the baffle-outer shell contact with changes in temperature, it is the only model considered for all further analyses.

The average of the velocity level transfer function computed at the 9 accelerometers using the modal coupling model is presented in Figure 5.13a alongside that computed using the hybrid vibroacoustic model for comparison. The structural model used for both the modal coupling and hybrid vibroacoustic models is the one where the baffle-outer shell contact is identified using the Nastran SOL 400 solution sequence.

From Figure 5.13a, it can be seen that the modal coupling model results match reasonably well with the results from the hybrid vibroacoustic model and can therefore be used as a replacement for the hybrid vibroacoustic model under room temperature conditions

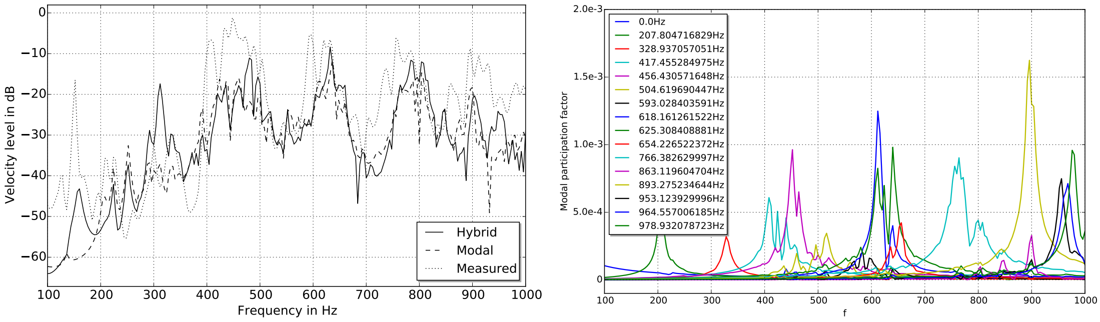

(a) Velocity level transfer function comparison plot.

(b) Contact-Fluid modes

Figure 5.13.: Modal coupling model results for the stock rear muffler.

with reliable results.

Modal participation coefficients (described in Chapter 2) for the fluid cavity can be visualised in a modal coupling model in addition to those of the structure model that can be extracted through a hybrid vibroacoustic model as well. The contribution of each fluid eigenmode to the overall response of the muffler is plotted in Figure 5.13b. As expected, the contribution of the fluid cavity modes is highest at around the peaks in the measured shell noise TFs. It can also be seen that though the fluid cavity modes above 850 Hz contribute significantly to the response, it is not reflected in the surface velocity TF seen in Figure 5.13a. This indicates that the structure modes at these frequencies have been insufficiently captured by the 'Contact' model leading to poor coupling with the fluid cavity modes. It is also possible that the model is overdamped in this frequency region as it was seen that the effect of damping starts to become significant only in this region.

5.5. Experimental investigation - Engine operating conditions

In this section, waterfall plots of the surface acceleration levels at accelerometers '*AccH08*' and '*Acc1201L*' and the radiated noise measured at microphones '*Exh518*' and '*Exh519*' at selected engine operating conditions are presented. The two microphones are each mounted 10 cm below the two accelerometers respectively. Based on the close correlation in the shape of the surface velocity and the radiated SPL TF plots reported in Section 5.1, a similar correlation is expected for the surface acceleration level and radiated SPL waterfall plots. Acceleration levels have been used instead of velocity levels used thus far, as the resonances are more clearly visible in the acceleration level plots due to the higher signal to noise ratio. The lower frequency limit in the following plots is set to be above the third and fourth engine orders.

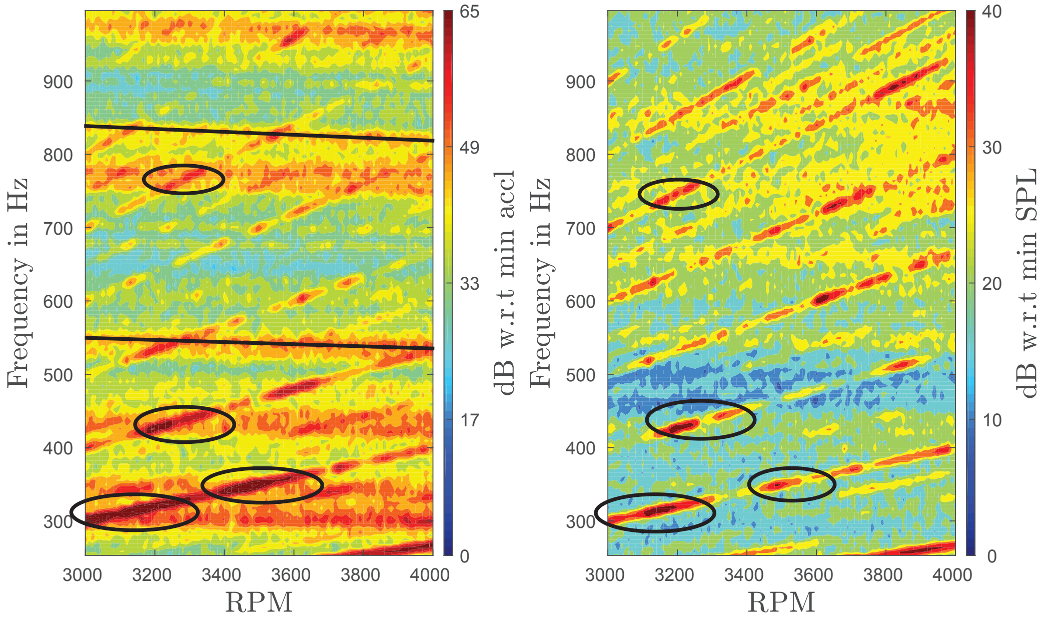

(a) Surface acceleration levels at AccH08

(b) Radiated noise levels at Exh518

Figure 5.14.: Engine operating conditions - ⅔ POT, 3000-4000 RPM sweep.

With an increase in temperature, the material properties of the fluid and the structure change, which is expected to cause a change in the eigenfrequency of both components. The eigenfrequencies of the structure are expected to decrease and the eigenfrequencies of the air cavity inside are expected to increase, with an increase in temperature. In Figure 5.14a, the black line sloping down gently from left to right is drawn over a typical resonance as the RPM sweep progresses. The resonance peaks can be characterised as straight line trends seen on the waterfall plots that do not correspond to the positively sloping trend of any of the engine orders. The temperature increases as the RPM sweep progresses which implies that the downward slope of the resonances with an increase in temperature is a consequence of the structural eigenfrequencies rather than the fluid ones. The change in these resonances with the change in temperature across an RPM sweep is seen to be approximately linearly varying with temperature. At certain points where it meets engine order peaks, the response is amplified as can be seen in the regions marked by the black ovals. Corresponding peaks in the SPL waterfall plot are also marked with black ovals in Figure 5.14b. This correlation, though not as high as that seen in the TF plots in Section 5.1 is nevertheless evidence for the presence of shell noise. A correlation is also present to a lesser degree between 750-800 Hz.

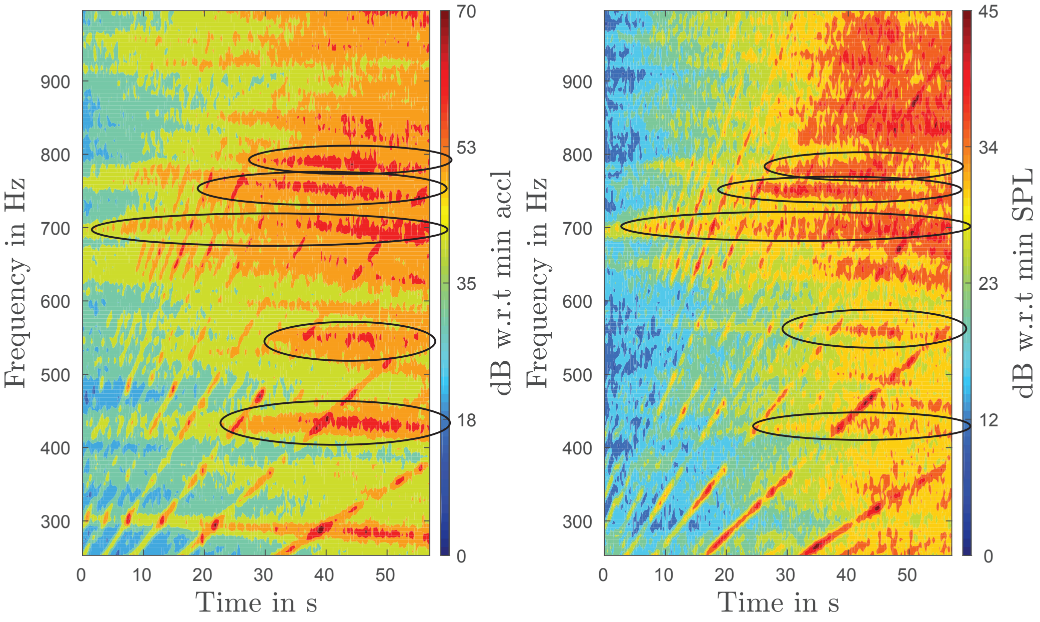

(a) Surface acceleration levels at Acc1201L

(b) Radiated noise levels at Exh519

Figure 5.15.: Engine operating conditions - WOT, 1250-5500 RPM sweep.

In Figures 5.15a and 5.15b however, the correlation is not just limited to the peaks in the waterfall plot but also to the temperature induced movement of the resonances themselves. The black ovals in Figure 5.15a indicate the movement of structural resonances which can be seen to correspond well with those in Figure 5.15b also marked by black ovals. However, these are seen to be not quite as straight as the resonance peak lines seen in the slower RPM sweeps from 3000-4000 RPM and 4000-5000 RPM. The resonance peak line is mostly flat until about 30 sec into the sweep as seen in Figure 5.15a before it starts to slope downwards. This can perhaps be attributed to a transient effect which is seemingly avoided in the case of the slower RPM sweeps from 3000-4000 RPM and 4000-5000 RPM.

Overall, the correlation between the measured surface acceleration levels and the radiated SPL is not as high as those in Section 5.1 because the microphone signals are contaminated by other noise sources. The most important amongst these sources could be flow noise from the tailpipe orifice, which is located closest to the nearfield microphones '*Exh518*' and '*Exh519*'. This effect seems to be restricted to the higher frequencies above

600 Hz when the engine is not under wide open throttle conditions like in Figure 5.14b. But it appears to become prominent across the whole frequency range under wide open throttle conditions seen in Figure 5.15b.

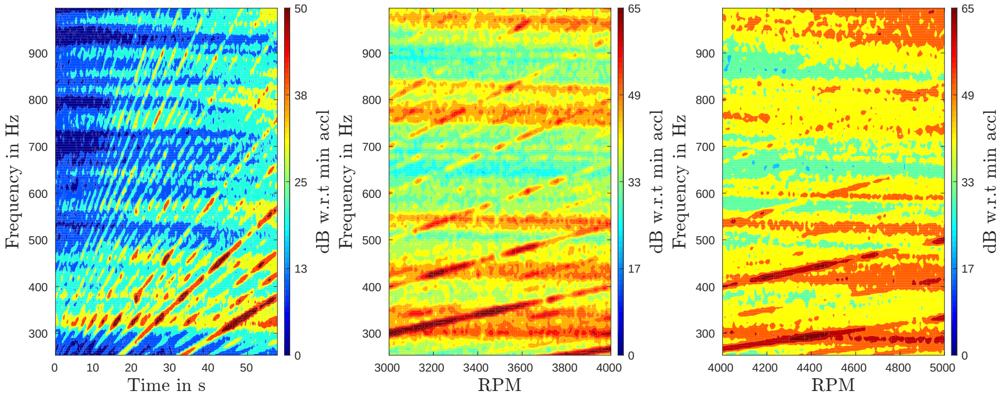

(a) ⅓ POT, 1250-5500 RPM (b) ⅔ POT, 3000-4000 RPM (c) ⅔ POT, 4000-5000 RPM

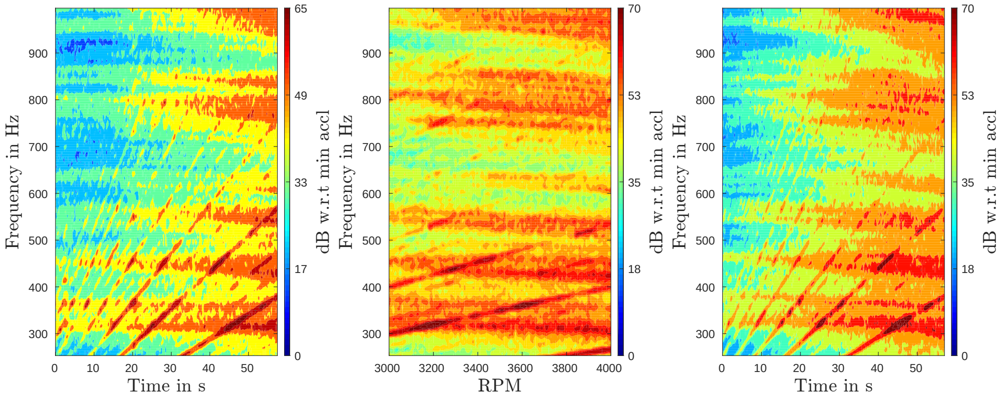

(d) ⅔ POT, 1250-5500 RPM (e) WOT, 3000-4000 RPM (f) WOT, 1250-5500 RPM

Figure 5.16.: Measured acceleration level plots at Accelerometer '*H08*'.

Finally, the variation of these resonances with temperature is seen to be small. This effect is seen, for instance, in Figure 5.16 which shows the measured acceleration levels at the accelerometer '*H08*'. The resonances of the structure most prominently seen at this sensor position are seen to be located more or less at similar positions along the frequency spectrum for all the trials, during which temperatures vary from 550 K to 900 K. Thus, the resonances are not very sensitive to the the fluid temperature for the operating range present during these measurements.

5.6. Elevated temperature simulation models

As discussed in the previous section, the variation of the resonance peak can be modelled as a linear regression for the slow RPM sweep measurements. At the same time, the temperature variation too can be modelled as a linear regression as seen in Figures 3.11. With these assumptions in place, the simulation model is set up and run only at the start and end temperatures. Therefore the trials for which the simulations are set up are limit to only the slow RPM sweeps with the exception of the 1/3 POT load case where the temperature change is seen to be too small for the resonance peak drop to be significant and is therefore excluded.

5.6.1. Vibroacoustic simulation

A vibroacoustic model was created and the acceleration at the accelerometers was computed through a direct frequency response analysis with a unit velocity boundary condition at the inlet of the muffler. This analysis was performed for all the selected trials and the transfer functions at the respective accelerometer positions were obtained and presented in Figure 5.17.

It can be seen from Figure 5.17 that all the TFs have a similar shape for the selected trials with a broad peak around 750 Hz and a narrower couple of peaks at around 500 Hz. These results support the observation from the previous section that within the operating range present during these measurements, that the air temperature does not significantly alter the vibroacoustic response of the muffler system.

However, it was found that this is not true at temperatures outside the operating range of the measurements. Figure 5.18 shows the similar quantities as in Figure 5.17, but whose start and end temperatures do not correspond to any measurement conditions. Instead, the fluid temperature has been elevated in steps of 100 K from room temperature and onwards. For the sake of comparison, the structure in these simulations was maintained at 290 K, i.e. room temperature to observe the effects of varying the fluid temperature alone.

It can be seen from Figures 5.18a-5.18b that the vibroacoustic response of the system does indeed vary significantly with the fluid temperature but below the lowest operating temperature of the measurements at 550 K. In Figure 5.18c however, the response of the system reverts back to that seen in Figures 5.17 where the 100 K rise in temperature from

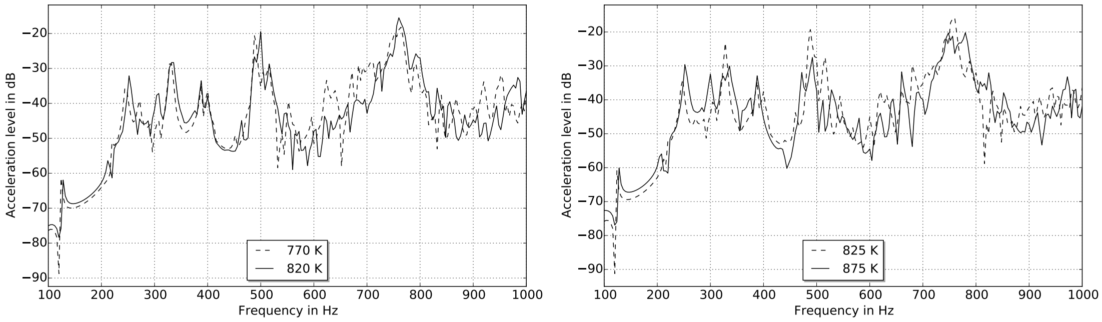

(a) ⅓ POT, 4000-5000 RPM, $\Delta T = 50$ K

(b) ⅔ POT, 3000-4000 RPM, $\Delta T = 50$ K

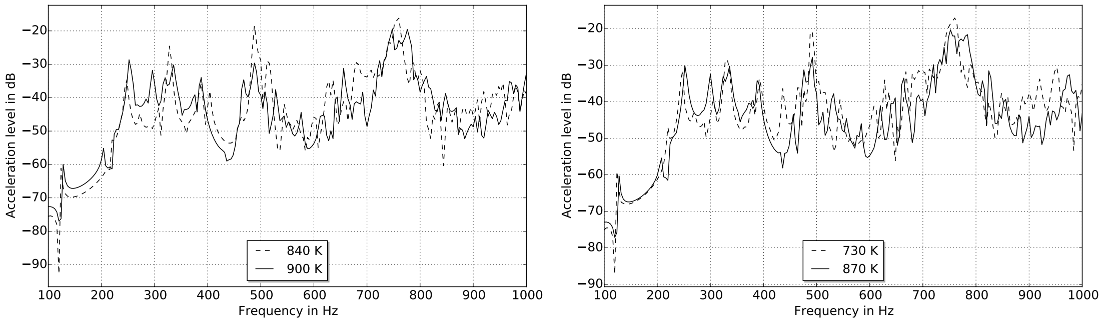

(c) ⅔ POT, 4000-5000 RPM, $\Delta T = 60$ K

(d) WOT, 3000-4000 RPM, $\Delta T = 140$ K

Figure 5.17.: Surface acceleration level TFs with respect to inlet averaged across all 6 accelerometers.

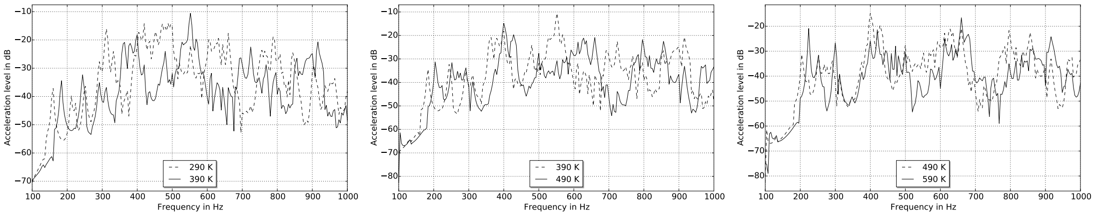

(a)

(b)

(c)

Figure 5.18.: Surface acceleration level TFs with respect to inlet averaged across all 6 accelerometers.

490 K to 590 K has not significantly affected the response. This indicates that the fluid modes dominate the surface vibrations and consequently the radiated shell noise only at temperatures close to room temperature. It can also be noted that there is a significant peak in the TF around 400 Hz at all temperatures indicating that the structure modes present in that frequency region are strongly radiating ones.

Finally, the resonance peaks predicted by this model in Figure 5.17, does not match those seen on the measured acceleration level waterfall plots in Figure 5.16 for any of the sensor positions. This can easily be attributed to the inaccurate spatial temperature distribution model used for the muffler shell. This conclusion can be derived by comparing the shapes of the TFs in Figures 5.17, which use the approximate temperature distribution model estimated from prior measurements at VCC, with those in Figures 5.18, which assigns the room temperature throughout the structure. In addition to the inaccurate spatial temperature distribution model applied on the structure, the fluid temperature distribution too is unaccounted for as a uniform temperature is assumed in these models.

5.6.2. Eigenvalue analysis of the structure

An eigenvalue analysis of the muffler structure was performed at the start and end temperatures for selected trials. The change in the eigenfrequencies between the start and end temperatures are averaged for all the frequencies in the range 100-1000 Hz and presented in Table 5.1 along with the corresponding change in eigenfrequencies seen in the measured waterfall plots. In addition, the eigenvalues of the fluid cavity, performed at the same temperatures corresponding to the selected trials, are presented for comparison. The measured average drop in eigenfrequencies is calculated through visual inspection, for clearly visible resonances or those with a well defined linear trend. This is done for all the six accelerometers and for the selected trials and is then averaged. The measured waterfall plots from which these averages have been computed are presented in Appendix B.3.

Trial	1/3 *POT, 4000-5000 RPM*	2/3 *POT, 3000-4000 RPM*	2/3 *POT, 4000-5000 RPM*	*WOT, 3000-4000 RPM*
Only structure	-8.85 Hz	-15.92 Hz	-20.10 Hz	-20.21 Hz
Measured resonances	-10.87 Hz	-10.63 Hz	-19.28 Hz	-23.5 Hz
Only fluid cavity	23.63 Hz	22.11 Hz	24.58 Hz	61.4 Hz

Table 5.1.: Mean eigenfrequency drop due to temperature elevation

The magnitude of the drop in eigenfrequencies of the structure with an increase in temperature can be seen to be fairly minimal, just like in the measurements. It can also be concluded that the change in the resonances seen in the measurements is primarily dominated by structural behaviour, unlike at room temperature, since the fluid cavity eigenvalues tend to go up as seen in Table 5.1. It can be seen that though the eigenfrequency drops for the FE model and the measurements do not match perfectly, they are comparable for all the trials. In addition to the mean value, the magnitude of the eigenfrequency drop is also seen to increase gradually with increasing frequency. This trend is also seen in the measured waterfall plots in Appendix B.3 where the eigenfrequencies below 500 Hz tend to fall marginally slower with an increase in temperature compared to those above 500 Hz.

The discrepancy between the structural eigenvalue analysis results and and measured resonance drops in Table 5.1 can be attributed to a few issues such as not all resonances being clearly distinguishable. Some tend to be broad peaks and therefore lie across a wide frequency band or do not exist across the entire sweep. This could be because resonance peaks lying close to each other on the frequency spectrum remain unresolved and instead get interpolated due to the low frequency resolution which is comparable to the actual drop in the eigenfrequencies themselves. So the sample from which the measurement eigenfrequency drops are calculated is small and the inaccuracies of a visual evaluation creep in to affect the validity of those values in Table 5.1.

6. Conclusions

6.1. Summary

The results of the thesis can be summarised as follows:

- Comprehensive shell noise measurements under room temperature conditions were carried out at MWL, KTH for three different mufflers: the front muffler, the rear muffler and the rear muffler with spot welded baffles. This included surface velocity level and radiated SPL TFs and transmission loss measured in a fully anechoic environment with a loudspeaker noise input. It is found that the acoustic termination boundary condition is not an important factor with respect to shell noise. It is also found that spot welding the baffles too does not greatly affect the shell noise except for a very small frequency band.

- An FE free field radiation model and different FE structure models using a hybrid vibroacoustic coupling were created and the results of these models were compared against measurements from the anechoic chamber. The results of the simulation model of the front muffler show a poor fit with the measured TFs. The results of all the simulation model of the rear muffler on the other hand matched reasonably well with the measurements above a certain frequency. Below this frequency, the '*Contact*' and '*RBE3-CBUSH-RBE3*' structure models displayed better fit compared to the '*RBE3*' model. The peaks in the measured and simulated TFs of the rear muffler corresponded with the eigenfrequencies of the standalone muffler cavity under room temperature conditions.

- A modal coupling model approach was created which enables much faster computation of surface level TFs in addition to giving an idea of the relative modal participation of each fluid mode. This model was compared with the hybrid vibroacoustic coupling model as well as the measured TFs and verified.

- Shell noise measurements were conducted on the rear muffler when it was mounted on the car in a semi-anechoic chamber equipped with a chassis dynamometer at VCC. Slow and fast RPM sweeps were conducted at different loads and the absolute surface acceleration levels on the underside of the muffler and radiated SPLs 10cm from the underside of the muffler were obtained for each trial. Radiated shell noise observed in the spectrograms were not prominent seen except in a few regions when the engine order met a resonance. Changing temperatures throughout the RPM sweep and across different trials, varying between 550-900 K were only seen to have a marginal effect on the vibroacoustic response of the rear muffler.

- Finally, a structural eigenvalue analysis and a hybrid vibroacoustic coupling analysis was performed at elevated temperature levels approximating the prevailing temperature conditions of the chassis dynamometer measurements. The surface acceleration transfer functions obtained from the hybrid vibroacoustic coupling analysis(Figure 5.17) do not correspond very well with the measured waterfall plots(Figure 5.16) at any of the sensor positions and trial cases. However, the change in the eigenfrequencies of the structure seen in the measurements roughly matches that of the simulation. Finally, the relative insensitivity of the vibroacoustic response of the system with respect to temperature seen earlier in the measurements, is reflected in the simulations as well. Furthermore, it is found that lowering the temperature of the system increases the significance of the temperature as a determining factor in surface vibration TFs.

6.2. Conclusions

- Equivalent fluid models, with flow resistivity as the characteristic property, were found to be insufficient to model the shell noise characteristics of mufflers filled with porous material such as the front muffler in this case. A more complete poroacoustic model which accounts for the elastic properties of the porous skeleton might improve the fit of the simulated results with measurements .
- Furthermore, material anisotropy and geometric inhomogenity in the porous skeleton may also have been present in the muffler specimen under testing and this must be accounted for. These inconsistencies can be investigated by physically dissecting a muffler specimen.
- The fact that shell noise characteristics are mostly insensitive to acoustic boundary conditions at the inlet and the outlet was used to convert the muffler interior into

a cavity and perform faster analysis using modal coupling. This method can be used for quick design iterations.

- The peaks in the shell noise TFs are determined by the fluid cavity eigenmodes which determine which structural eigenmodes are excited more than others to contribute most to shell noise. This behaviour is limited however to only room temperature.
- The nature of baffle-outer shell connections is most significant above a certain critical frequency, 400 Hz for the rear muffler under ambient conditions, above which the transfer function levels are tens of decibels higher. Below this frequency, it is as though the baffles are left unconnected. This frequency seems to correspond to the first flexible eigenmodes of the largest radiating surfaces in contact with the central baffle when all the baffles are rigidly connected with each other. This mode is seen to radiate well when sufficiently excited by a fluid mode.
- With elevation in temperature of the system from ambient conditions up to the levels seen under engine operating conditions, the fluid properties, and by consequence the fluid cavity modes, are seen to play a continuously diminishing role in the vibroacoustic response of the system. In other words, the vibroacoustic response per unit input of the system is more or less invariant to fluid temperature during engine running conditions.
- The elevated temperature simulation models have only been proven to be acceptable in comparative assessment but not in absolute assessment with the measurements primarily due to insufficient temperature profile data within the fluid as well as on the structure.

6.3. Recommendations

- The model developed for the front muffler can be used only for comparative assessment.
- From the point of view of modelling only the structure, baffle-outer shell connections' influence have to be taken into account only above a certain frequency.
- From the point of view of modelling only the fluid for shell noise simulation, acoustic boundary conditions are not very significant and therefore need not be priori-

tized.

- From the point of view of modelling shell noise as a fully coupled phenomenon, the temperature of the system must be taken into account in order to determine which resonances will actually be seen under engine operating conditions.

6.4. Future work

- A porous material model that accounts for the elastic properties of the porous skeleton can be used instead of the equivalent fluid models used in this thesis on the front muffler. This might improve the fit between simulated and measured surface velocity and radiated SPL transfer function plots. However, these models are expected to be computationally expensive as the number of degrees of freedom are now quadrupled in the porous material regions.

- The Nastran SOL 400 solution sequence contact parameter settings can be studied more in detail and perhapsn applied on the front muffler to identify areas in contact. The simulations can be performed again to examine its influence on shell noise.

- More accurate temperature distribution data across the entire system, both fluid and structure, can be obtained through CFD simulations and/or measurements. This enables not only comparative assessment between two simulation models at different temperatures, but the simulated resonances can now more directly compared to the resonances seen in the measurements.

- Source data from the engine can be used in the vibroacoustic simulations to obtain results in absolute values. This can subsequently be compared directly with measurements obtained under engine operating conditions, when transfer function measurements are not possible. An added benefit of this method is to examine which of the resonances in the structure are actually affected.

A. Appendix - Derivations

A.1. Wave propagation in circular ducts.

The 3-dimensional homogeneous wave equation can be expressed in cylindrical coordinates as follows, for the case of a duct in ambient room temperature with zero mean flow.

$$\frac{1}{c_0^2}\frac{\partial^2 p}{\partial t^2} = \frac{\partial^2 p}{\partial r^2} + \frac{1}{r}\frac{\partial^2 p}{\partial r} + \frac{1}{r^2}\frac{\partial^2 p}{\partial \phi^2} + \frac{\partial^2 p}{\partial x^2} \tag{A.1}$$

Here, t is the time, r is the radial coordinate, ϕ the circumferential coordinate and x is the axial coordinate. c_0 is the speed of sound which is constant in this case and p is the acoustic pressure fluctuations. PDEs such as the wave equation is known to be conducive to solution by the method of separation of variables. With this in mind, the acoustic pressure fluctuations can therefore be modelled as per the following ansatz[18].

$$p(r, \phi, x, t) = p_r(r)p_\phi(\phi)p_x(x)p_t(t) \tag{A.2}$$

Substituting this ansatz into the wave equation in (A.1) and rearranging, the following equation is obtained,

$$\frac{1}{c_0^2}\frac{p_t''}{p_t} = \left(p_r'' + \frac{1}{r}p_r\right)\frac{1}{p_r} + \frac{1}{r^2}\frac{p_\phi''}{p_\phi} + \frac{p_x''}{p_x} \tag{A.3}$$

where p' represents the first derivative of p.Since the RHS of the above equation is independent of t, the term on the LHS must be a constant, say $-k^2$, where k is called the wavenumber. This gives the following equation,

$$\frac{1}{c_0^2}\frac{p_t''}{p_t} = -k^2 \implies p_t'' + \omega^2 p_t = 0 \tag{A.4}$$

Here, $\omega = kc_0$ is the angular frequency of the pressure wave. The solution of this equation is known to be, for a causal event for which $t > 0$,

$$p_t(t) = p_{t0}e^{i\omega t} \tag{A.5}$$

Substituting the solution (A.4) in (A.3) and rearranging it gives,

$$-k^2 - \frac{p_x''}{p_x} = \left(p_r'' + \frac{1}{r}p_r\right)\frac{1}{p_r} + \frac{1}{r^2}\frac{p_\phi''}{p_\phi} \tag{A.6}$$

Similar to the previous separation operation, the LHS can be equated to a constant say $-a^2$.

$$-k^2 - \frac{p_x''}{p_x} = -a^2 \implies p_x'' + (k^2 - a^2)p_x = 0 \tag{A.7}$$

Again, similar to the time harmonic solution,

$$p_x(x) = p_{x0}e^{\pm i\sqrt{k^2-a^2}x} \tag{A.8}$$

Substituting the solution (A.7) in (A.6) and rearranging it gives,

$$-\frac{p_\phi''}{p_\phi} = \left(p_r'' + \frac{1}{r}p_r\right)\frac{r^2}{p_r} + r^2a^2 \tag{A.9}$$

Again, similar to the previous separation operation, the LHS can be equated to a constant say m^2.

$$-\frac{p_\phi''}{p_\phi} = m^2 \implies p_\phi'' + m^2 p_\phi = 0 \tag{A.10}$$

Once again, similar to the time harmonic solution,

$$p_\phi(\phi) = p_{\phi 0}e^{\pm im\phi} \tag{A.11}$$

From the above equation, it is clear that m, referred to the azimuthal mode number, should be an integer since $p_\phi(0) = p_\phi(2\pi)$ for any closed pipe. Substituting the solution (A.10) in (A.9) and rearranging it gives,

$$\frac{m^2}{r^2} - a^2 = \left(p_r'' + \frac{1}{r}p_r\right)\frac{1}{p_r} \tag{A.12}$$

Introducing a variable transformation, $s = ar$, the chain rule can be implemented to give (A.13) after some simplification.

$$s^2 p_r''(s) + s p_r'(s) + (s^2 - m^2)p_r = 0 \tag{A.13}$$

This is the standard form of Bessel's equation whose solution is given by a Bessel function of the first kind,

$$p_r(r) = J_m(s) = J_m(ar) \tag{A.14}$$

However, this radial solution is subject to the boundary condition given by the Euler equation,

$$\left.\frac{\partial v}{\partial t}\right|_{r=R} = \left.\frac{1}{\rho_0}\frac{\partial p_r}{\partial r}\right|_{r=R} = 0 \tag{A.15}$$

Here v is the local velocity of the air and rho_0 is the density of air. Assuming that the wall is hard as an approximation, the local velocity and therefore the radial pressure gradient must be zero. Thus, from (A.14), the following is true,

$$J'(aR) = 0 \tag{A.16}$$

The first derivative of Bessel's equation is known to have infinite zeros and so the μ^{th} positive zero for the above equation can therefore be denoted as,

$$j'_{m\mu} = a_{m\mu}R \implies a_{m\mu} = \frac{1}{R}j'_{m\mu} \tag{A.17}$$

Substituting the expression for $a_{m\mu}$ in (A.8), we obtain the following equation for the complex amplitude of the axially propagating wave.

$$p_x(x) = p_{x0}e^{\pm ik_x x} \tag{A.18}$$

Where the axial wavenumber is given by,

$$k_x = \sqrt{k^2 - \left(\frac{j'_{m\mu}}{R}\right)^2} \tag{A.19}$$

A.2. Experimental determination of boundary conditions.

A.2.1. Inlet velocity

The origin can be arbitrarily assumed to be at the point where the desired inlet velocity and impedance is to be known. Equation (2.19) can then be applied to the two microphone positions at x_0 and $x_0 + \Delta x$, shown in the figure, to give the following expressions.

$$p_{x_0} = p^+e^{-ikx_0} + p^-e^{ikx_0} \tag{A.20}$$

$$p_{x_0+\Delta x} = p^+e^{-ik(x_0+\Delta x)} + p^-e^{ik(x_0+\Delta x)} \tag{A.21}$$

This equation can be rearranged to give an expression for the forward and backward travelling wave amplitudes.

$$\begin{Bmatrix} p^+ \\ p^- \end{Bmatrix} = \frac{1}{e^{ik\Delta x} - e^{-ik\Delta x}} \begin{bmatrix} e^{ik(x_0+\Delta x)} & -e^{ikx_0} \\ -e^{-ik(x_0+\Delta x)} & e^{-ikx_0} \end{bmatrix} \begin{Bmatrix} p_{x_0} \\ p_{x_0+\Delta x} \end{Bmatrix} \tag{A.22}$$

However, since only the phase difference in the signal between the microphone positions is known, x_0 is put to zero to simplify the above equation. This means that the phase at the first microphone position is assumed to be zero and the at the second is, say $\Delta\varphi = \angle H_2 - \angle H_1$.

A.2.2. Impedance

In order to determine the impedance from measured transfer function data, one can define the following auto-spectrums and cross-spectrums.

$$S_{11} = H_1.H_1^* \qquad S_{22} = H_2.H_2^* \qquad S_{12} = H_1.H_2^* \tag{A.23}$$

$$S_{p^+p^+} = H_{p^+}.H_{p^+}^* \qquad S_{p^-p^-} = H_{p^-}.H_{p^-}^* \qquad S_{p^+p^-} = {H_p}^+.{H_p}^{-*} \tag{A.24}$$

Where S_{11} is the auto-spectrum of the transfer function at the first microphone position, S_{22} is the auto-spectrum of the transfer function at the second microphone position, S_{12} is the cross-spectrum of the transfer function between the first and second microphone positions, $S_{p^+p^+}$ is the auto-spectrum of the transfer function of the forward travelling wave, $S_{p^-p^-}$ is the auto-spectrum of the transfer function of the backward travelling wave and $S_{p^+p^-}$ is the cross-spectrum of the transfer functions between the forward and backward travelling wave.

The measured transfer functions also satisfy equation (A.20) as all the pressure signals are normalized by the same reference signal. With this in mind, the terms in Equation (A.20) can be substituted into the expressions in Equation (A.23) to result in the following matrix equation.

$$\begin{Bmatrix} S_{p^+p^+} \\ S_{p^-p^-} \\ S_{p^+p^-} \end{Bmatrix} = \begin{bmatrix} 1 & 1 & e^{-2ikx_0} + e^{2ikx_0} \\ 1 & 1 & e^{-2ik(x_0+\Delta x)} + e^{2ik(x_0+\Delta x)} \\ e^{ik\Delta x} & e^{-ik\Delta x} & e^{-ik(2x_0+\Delta x)} + e^{ik(2x_0+\Delta x)} \end{bmatrix}^{-1} \begin{Bmatrix} S_{11} \\ S_{22} \\ S_{12} \end{Bmatrix} \tag{A.25}$$

The auto-spectrum of the velocity at a section, S_{vv} and the cross-spectrum between the pressure and velocity at the same section, S_{pv}, used to redefine impedance as shown in Equation (2.22), can be defined as follows,

$$S_{v_0v_0} = v_0.v_0^* \qquad S_{p_0v_0} = p_0.v_0^* \tag{A.26}$$

Where p_0 is the complex pressure at the origin (inlet/outlet) and v_0 is the complex velocity. p_0 and v_0 can be obtained from Equation (A.20) as follows,

$$p_0 = p_+ + p_- \tag{A.27}$$

$$v_0 = v_+ + v_- = \frac{p_+}{Z_0} + \left(\frac{-p_-}{Z_0}\right) \tag{A.28}$$

Substituting the above expressions in Equation (2.22), the following equation is obtained.

$$Z\bigg|_{x=0} = \frac{(p_+ + p_-)(p_+^* + p_-^*)}{(p_+ - p_-)(p_+^* - p_-^*)} = \frac{p_+.p_+^* - p_-.p_-^* - (p_+.p_-^* - p_-.p_+^*)}{p_+.p_+^* + p_-.p_-^* - (p_+.p_-^* + p_-.p_+^*)} \tag{A.29}$$

Then, using the definitions of $S_{p^+p^+}$, $S_{p^-p^-}$ and $S_{p^+p^-}$ from Equation (A.23), the above equation can be rewritten as shown in Equation (2.23).

A.3. Finite Element Model of Acoustic-Structure interaction.

A.3.1. FE model - Structure

Consider a damped structure interacting with the acoustic medium, whose behaviour follows the standard dynamic equation can be expressed as shown below,

$$\boldsymbol{M}_s \ddot{\overrightarrow{u}} + \boldsymbol{C}_s \dot{\overrightarrow{u}} + \boldsymbol{K}_s \overrightarrow{u} + \overrightarrow{h}_{0s} + \overrightarrow{h}_a = 0 \tag{A.30}$$

$\overrightarrow{u}$ is the nodal parameter vector whose length is equal to the number of structural DOFs in the FE model, n_s, and is related to the structural displacement field $\overrightarrow{w}$ through the structural shape functions $\boldsymbol{N}_s$,

$$\overrightarrow{w} = \boldsymbol{N}_s \overrightarrow{u} \tag{A.31}$$

$\boldsymbol{K}_s$, $\boldsymbol{M}_s$, $\boldsymbol{C}_s$ are the global stiffness, mass and damping matrices for the structure. $\overrightarrow{h}_{0s}$ is the prescribed boundary condition vector which for the muffler structure corresponds to the muffler mounting conditions such simply supported, free or spring mounted. $\overrightarrow{h}_a$ is the Neumann boundary condition vector which for the muffler corresponds to the acoustic interaction force acting at the acoustic structure interface. For the acoustic-structure interface, Γ_s, this force can be represented as the acoustic pressure field, p at the area $d\Gamma_i$, multiplied by the normal component of the area itself, neglecting the tangential force due to the fluid[4].

$$\overrightarrow{h}_a = \sum_{(e)} \int_{\Gamma_s} \boldsymbol{N}_{s,i}^T \overrightarrow{n}_i p \, \mathrm{d}\Gamma_{s,i} \tag{A.32}$$

Where $\overrightarrow{n}$ is the unit area normal vector and $\sum_{(e)}$ indicates the FE assembly operation.

A.3.2. FE model - Fluid

The three-dimensional homogeneous wave equation for a quiescent medium under thermal equilibrium at room temperature can be represented in vector notation as follows,

$$\nabla^2 p - \frac{1}{c_0^2} \frac{\partial^2 p}{\partial t^2} = 0 \tag{A.33}$$

This strong form of the equation can be converted to the weak form by multiplying it by an arbitrary weighing function δp and integrated throughout the acoustic domain, Ω_a, to result in the following expression.

$$\int_{\Omega_a} \delta p \nabla^2 p \, \mathrm{d}\Omega - \int_{\Omega_a} \frac{\delta p}{c_0^2} \frac{\partial^2 p}{\partial t^2} \, \mathrm{d}\Omega = 0 \tag{A.34}$$

Using the property of the gradient operator, $\boldsymbol{\nabla}.(\varphi \boldsymbol{f}) = \varphi(\boldsymbol{\nabla}.\boldsymbol{f}) + (\nabla\varphi).\boldsymbol{f}$, the above equation can be rewritten as,

$$\int\limits_{\Omega_a} \nabla(\delta p \nabla p)\ \mathrm{d}\Omega - \int\limits_{\Omega_a} \nabla(\delta p)\nabla p\ \mathrm{d}\Omega - \int\limits_{\Omega_a} \frac{\delta p}{c_0^2}\frac{\partial^2 p}{\partial t^2}\ \mathrm{d}\Omega = 0 \tag{A.35}$$

Using the divergence theorem, the above equation can be rewritten as,

$$\int\limits_{\Gamma} \delta p(\nabla p.\overrightarrow{n})\ \mathrm{d}\Gamma - \int\limits_{\Omega_a} \nabla(\delta p)\nabla p\ \mathrm{d}\Omega - \int\limits_{\Omega_a} \frac{\delta p}{c_0^2}\frac{\partial^2 p}{\partial t^2}\ \mathrm{d}\Omega = 0 \tag{A.36}$$

Where Γ is the boudary of the acoustic fluid and includes Γ_a, the structure-acoustic interface, Γ_r, the radiation boundary which in the case of this muffler is the inlet and exhaust and Γ_v, the boundary over which the inlet velocity is defined. The pressure field can now be discretized through the fluid shape functions $\boldsymbol{N}_a$ as follows,

$$p = \boldsymbol{N}_a \overrightarrow{\mathrm{p}} \tag{A.37}$$

Where $\overrightarrow{\mathrm{p}}$ is the nodal parameter vector whose length is equal to the number of acoustic DOFs in the FE model, n_a. At the same time the Galerkin method can be applied on the arbitrary weighing function to express it in piecewise form as follows,

$$\delta p = \boldsymbol{N}_a^T \delta \mathrm{p} \tag{A.38}$$

Subtituting the expressions from (A.37) and (A.38) into (A.36), and subsequently eliminating $\delta\mathrm{p}$, the following expression is obtained,

$$\int\limits_{\Gamma} \delta p(\nabla p.\overrightarrow{n})\ \mathrm{d}\Gamma - \int\limits_{\Omega_a} \left(\nabla \boldsymbol{N}_{a,i}^T \nabla \boldsymbol{N}_{a,i}\mathrm{p} - \frac{1}{c_0^2}\boldsymbol{N}_{a,i}^T \boldsymbol{N}_{a,i}\frac{\partial^2 p}{\partial t^2}\right)\ \mathrm{d}\Omega = 0 \tag{A.39}$$

The boundary of the fluid, τ can be subdivided into the following regions,

$$\tau = \tau_a + \tau_r + \tau_v \tag{A.40}$$

Where τ_a which is the part of the fluid boundary interacting with the structure, τ_r is the part of the fluid boundary on which radiation impedance conditions are imposed and τ_v is the part of the fluid boundary on which a velocity boundary condition is imposed.

Euler's momentum equation relates the normal pressure gradient at the structure-acoustic interface to the normal component of the fluid displacement field at the corresponding location as follows,

$$\nabla p.\overrightarrow{n}\Big|_{\Gamma_a} = -\rho_0 \frac{\partial^2 \overrightarrow{w}}{\partial t^2}.\overrightarrow{n} \tag{A.41}$$

Here, $\overrightarrow{w}$ is in fact the structural displacement field which has to be equal to the fluid displacement field at the boundary to satisfy continuity. In addition to the structure-acoustic interaction boundary condition just discussed, radiation boundary conditions must be imposed on the acoustic fluid at the muffler inlet and exhaust. This can be done by specifying the acoustic impedances at the inlet and exhaust, computed through measurements. The acoustic impedance, Z_a, over the radiation boundary condition area, can be defined as follows,

$$p = Z_a \left(\frac{\partial w}{\partial t} . n \right) \tag{A.42}$$

Differentiating this equation with respect to time and substituting from (A.41) gives the radiation boundary condition,

$$\nabla p . \overrightarrow{n} \Big|_{\Gamma_r} = - \frac{\rho_0}{Z_a} \frac{\partial p}{\partial t} \tag{A.43}$$

Finally, the pressure gradient over the inlet velocity region, Γ_v, can be defined directly through (A.41) as follows,

$$\nabla p . \overrightarrow{n} \Big|_{\Gamma_v} = -\rho_0 \frac{\partial \overrightarrow{v}_{in}}{\partial t} . \overrightarrow{n} \tag{A.44}$$

Discretizing the equations (A.43) and (A.41) using (A.37) and subsequently substituting in (A.39) along with (A.44) and Galerkin weighing, gives rise to the following discretized form of the 3D acoustic wave equation.

$$\boldsymbol{M}_a \ddot{\overrightarrow{\mathrm{p}}} + \boldsymbol{C}_a \dot{\overrightarrow{\mathrm{p}}} + \boldsymbol{K}_a \overrightarrow{\mathrm{p}} + \overrightarrow{h}_s + \overrightarrow{h}_{0a} = 0 \tag{A.45}$$

Where,

$$\boldsymbol{M}_a = \sum_{(e)} \frac{1}{c_0^2} \int_{\Omega_{a,i}} \boldsymbol{N}_{a,i}^T \boldsymbol{N}_{a,i} \, \mathrm{d}\Omega \qquad \boldsymbol{C}_a = \sum_{(e)} \frac{\rho_0}{Z_f} \int_{\Gamma_{r,i}} \boldsymbol{N}_{a,i}^T \boldsymbol{N}_{a,i} \, \mathrm{d}\Gamma_{r,i} \tag{A.46}$$

$$\boldsymbol{K}_a = \sum_{(e)} \int_{\Omega_{a,i}} \nabla \boldsymbol{N}_{a,i}^T \nabla \boldsymbol{N}_{a,i} \, \mathrm{d}\Omega \tag{A.47}$$

h_s represents the acoustic-structure interaction given by,

$$h_s = \sum_{(e)} \int_{\Gamma_{a,i}} \rho_0 \boldsymbol{N}_{a,i}^T (\ddot{\overrightarrow{w}}^T . \overrightarrow{n}_i) \, \mathrm{d}\Gamma_{a,i} \tag{A.48}$$

And h_{0a} represents the prescribed boundary conditions corresponding to the velocity at the inlet, v_{in} given by,

$$h_{0a} = \sum_{(e)} \int_{\Gamma_{v,i}} -\rho_0 \frac{\partial \overrightarrow{v}_{in,i}}{\partial t} . \overrightarrow{n}_i \, \mathrm{d}\Gamma_{v,i} \tag{A.49}$$

A.4. Modal damping in structures

The modal damping model assumes that even the damping matrix can be diagonalized to result in n uncoupled single-DOF system when the displacement vector is transformed as in equation (2.7). The r^{th} diagonal element of the diagonalized mass, stiffness and damping matrices representing the r^{th} uncoupled single-DOF system can be expressed in an equation from (2.8) as follows[19],

$$m_r\ddot{\eta}_r + c_r\dot{\eta}_r + k_r\eta_r = f_r e^{i\omega t} \tag{A.50}$$

Where f_r is the modal forcing amplitude due to the acoustic excitation. The particular solution of this equation is therefore expected to be harmonic as follows,

$$\eta_r(t) = \eta_{r0}e^{i\omega t} \tag{A.51}$$

ϕ can be eliminated from equations (A.51) and (A.50) to result in the following relation for the complex modal amplitude η.

$$\eta_r = \frac{f_r}{(k_r - m_r\omega^2) + i\omega c_r} \tag{A.52}$$

The following quantities can then be defined.

$$\omega_r = \sqrt{\frac{k_r}{m_r}} \qquad \delta_s = \frac{f_r}{k} \qquad \zeta_r = \frac{\omega}{\omega_r} \tag{A.53}$$

$$c_{cr} = 2\sqrt{k_r m_r} \qquad \xi_r = \frac{c_r}{c_{cr}} \tag{A.54}$$

Here, ω_r, δ_s, ζ_r, ξ_r and c_{cr} are the resonant frequency, static deflection, frequency ratio, damping ratio and critical damping of the r^{th} mode. Substituting the above quantities into (A.52) and rearranging a bit, one obtains the frequency response function for the complex modal amplitude, $H(i\omega)$.

$$H(i\omega) = \frac{\eta_r}{\delta_s} = \frac{1}{(1-\zeta_r^2) + i(2\zeta_r\xi_r)} \tag{A.55}$$

Let the power dissipated through the damper at the resonance frequency be $W_{diss}(i\omega_r)$. Since this is the peak power dissipation, half of the maximum power is dissipated at two different frequencies, one above and one below the resonance frequency, say ω_{2r} and ω_{1r} respectively. The power dissipated at these frequencies is then, $W_{diss}(i\omega_{2r})$ and $W_{diss}(i\omega_{1r})$ respectively. Now, it is known that the power dissipated through the damper is proportional to the square of the amplitude or in this case, the amplitude normalized by the static deflection, i.e $W_{diss} \propto H.H^*$. Then, we get the following relation,

$$\frac{W_{diss}(i\omega_r)}{W_{diss}(i\omega_{1r,2r})} = \frac{H(i\omega_r)H^*(i\omega_r)}{H(i\omega_{1r,2r})H^*(i\omega_{1r,2r})} = 2 \implies \frac{(1-\zeta_r^2)^2 + (2\zeta_r\xi_r)^2}{(1-\zeta_{rr}^2)^2 + (2\zeta_{rr}\xi_r)^2} = 2 \tag{A.56}$$

Since, by definition, $\zeta_{rr} = 1$, the above expression simplifies to,

$$\zeta_r^4 - \zeta_r^2(2 - 4\xi_r^2) + (1 - 8\xi_r^2) = 0 \tag{A.57}$$

The roots of this equation are,

$$\zeta_{1r,2r}^2 = 1 - 2\xi_r^2 \pm 2\xi_r\sqrt{1 + \xi^2} \tag{A.58}$$

For a highly underdamped system, which an object created through sheet metal operations such as a muffler can be expected to be, the damping ratio is very close to zero, i.e $\xi_r \approx 0$. With this simplification and after substituting for the frequency ratio from (A.53), the above zeros fro the frequency ratio at the half power bandwidth points simplify to the following,

$$\left(\frac{\omega_{1r}}{\omega_r}\right)^2 = 1 - 2\xi_r \qquad \left(\frac{\omega_{2r}}{\omega_r}\right)^2 = 1 + 2\xi_r \tag{A.59}$$

The above expressions can be combined to give,

$$\frac{\Delta\omega(\omega_{1r} + \omega_{2r})}{\omega_r^2} = 4\xi_r \tag{A.60}$$

Where $\Delta\omega = (\omega_{2r} - \omega_{1r})$ is the half power bandwidth. For a highly underdamped system, the approximation $\omega_{1r} + \omega_{2r} = 2\omega_r$ is used to obtain the final relation for the damping ratio, ξ_r for the r^{th} mode in terms of the half power bandwidth and the resonant frequency,

$$\xi_r = \frac{\Delta\omega}{2\omega_r} \tag{A.61}$$

B. Appendix - Sensorwise results

B.1. Loudspeaker input measurement results.

B.1.1. Sound pressure level transfer functions

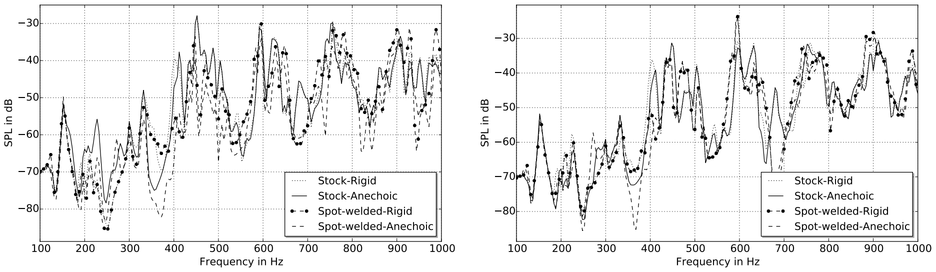

(a) Mic301 (b) Mic601

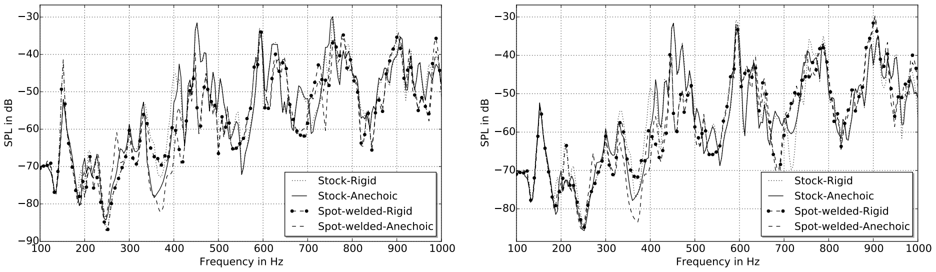

(c) Mic1201L (d) Mic1201R

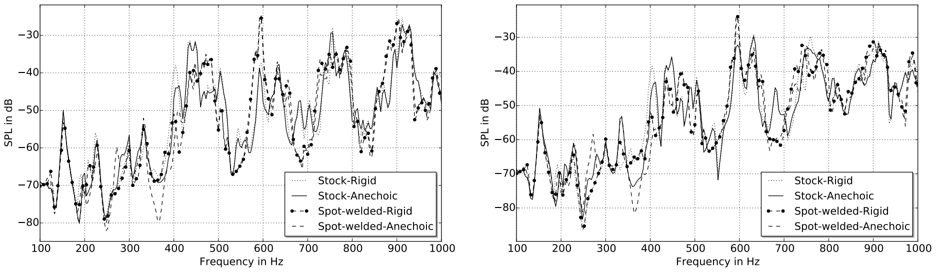

(e) Mic4501L (f) Mic4501R

Figure B.1.: Measured SPL transfer function comparison plots for the rear muffler.

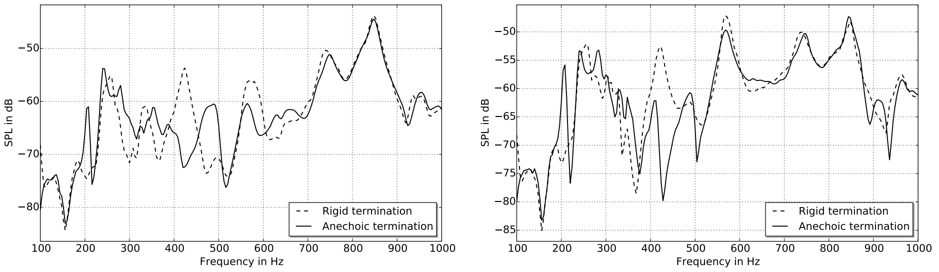

(a) Mic01 (b) Mic02

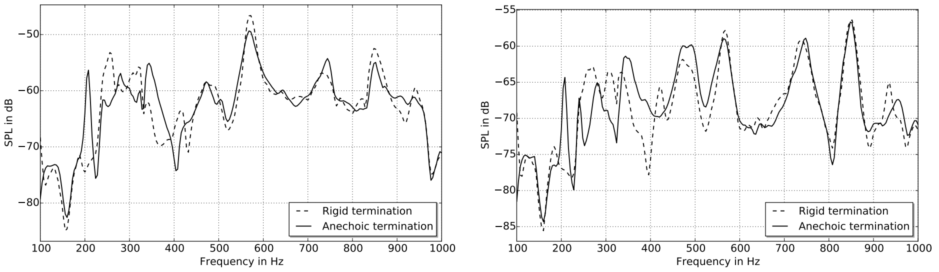

(c) Mic03 (d) Mic04

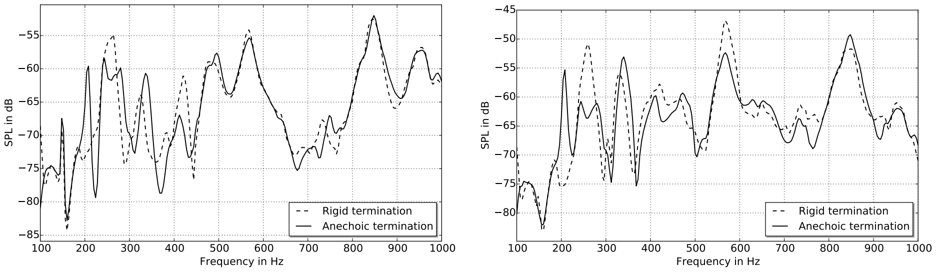

(e) Mic05 (f) Mic06

Figure B.2.: Measured SPL transfer function comparison plots for the front muffler.

B.1.2. Velocity level transfer functions

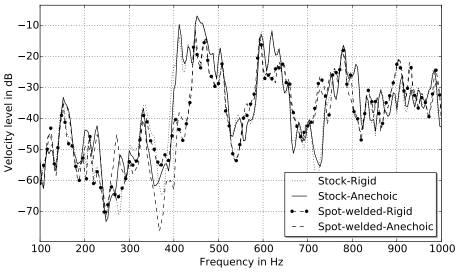

(a) Acc301

(b) Acc701

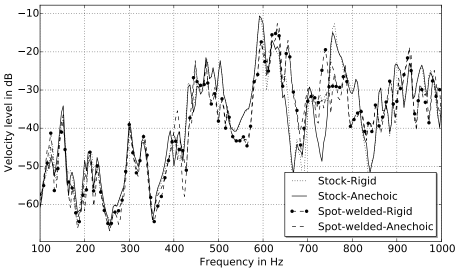

(c) Acc801

(d) Acc901

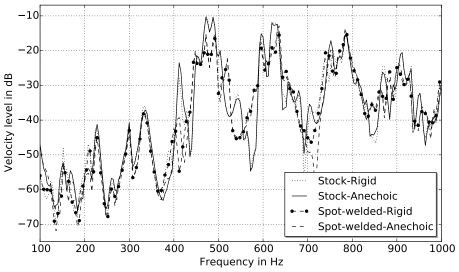

(e) Acc1201R

(f) Acc1201L

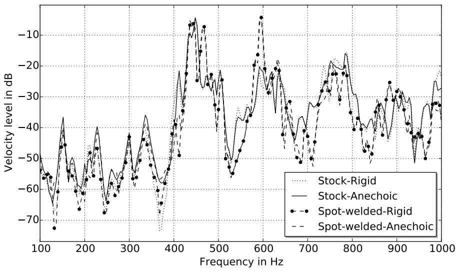

(g) Acc4501R

(h) Acc4501L

Figure B.3.: Measured velocity level comparison plots for the rear muffler.

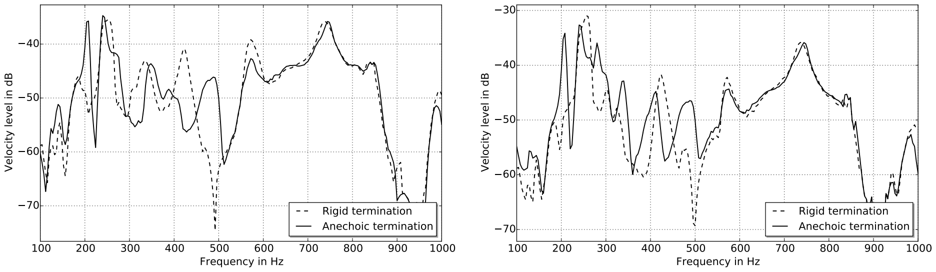

(a) Acc01 (b) Acc02

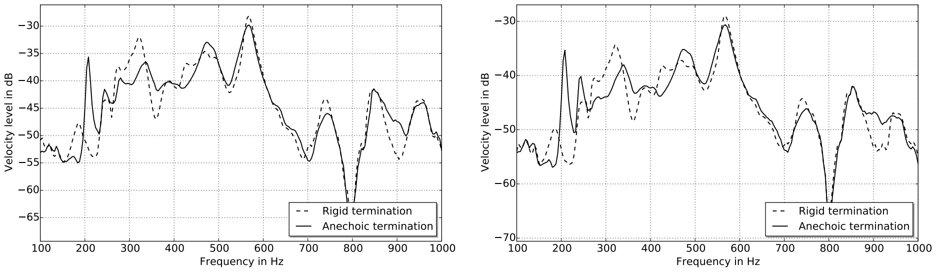

(c) Acc03 (d) Acc04

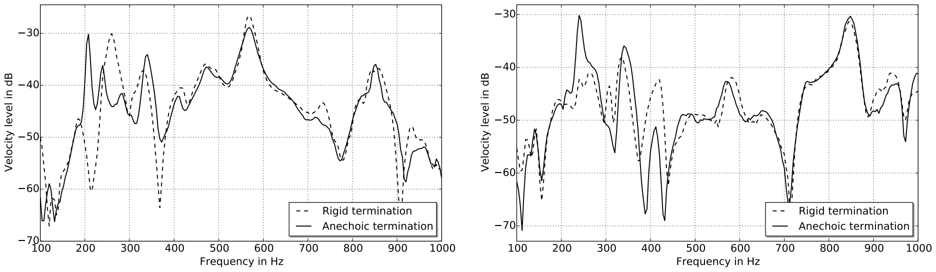

(e) Acc05 (f) Acc06

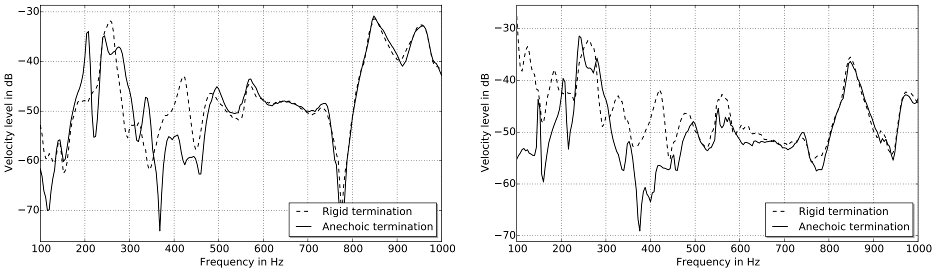

(g) Acc07 (h) Acc08

Figure B.4.: Measured velocity level comparison plots for the front muffler.

B.2. Simulation results

B.2.1. Sound pressure level transfer functions

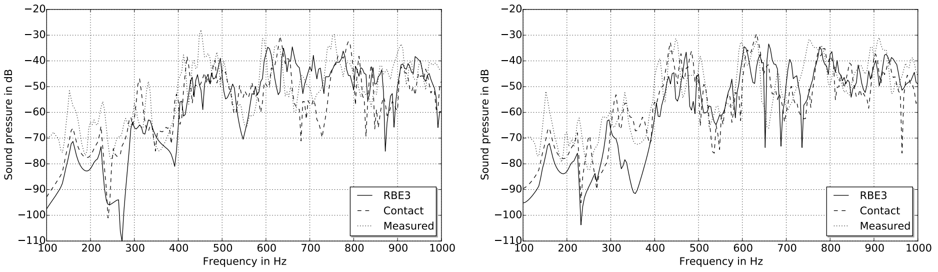

(a) Mic301 (b) Mic601

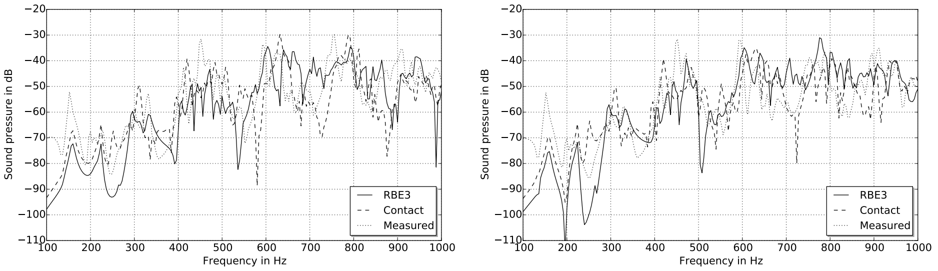

(c) Mic1201L (d) Mic1201R

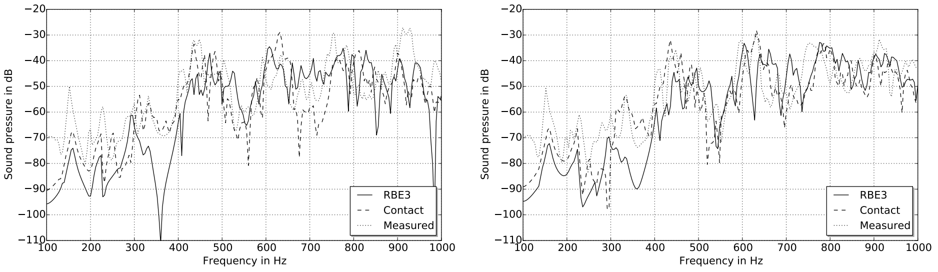

(e) Mic4501L (f) Mic4501R

Figure B.5.: SPL comparison plots for the rear muffler for all microphones.

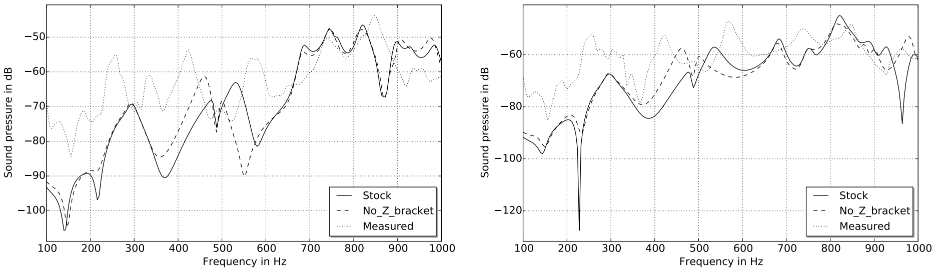

(a) Mic01 (b) Mic02

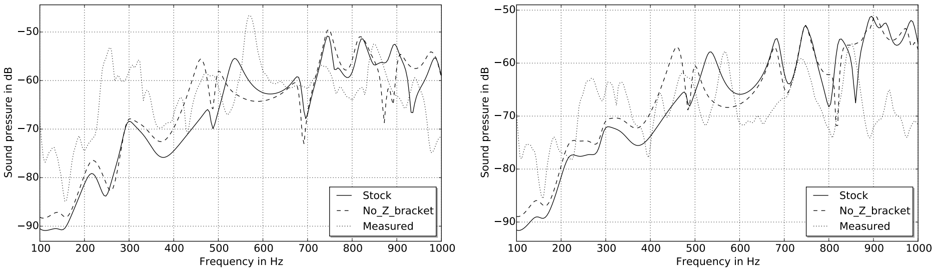

(c) Mic03 (d) Mic04

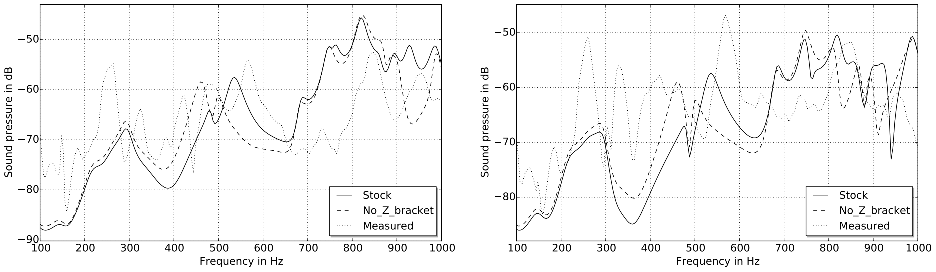

(e) Mic05 (f) Mic06

Figure B.6.: SPL comparison plots for the front muffler for all microphones.

B.2.2. Velocity level transfer functions

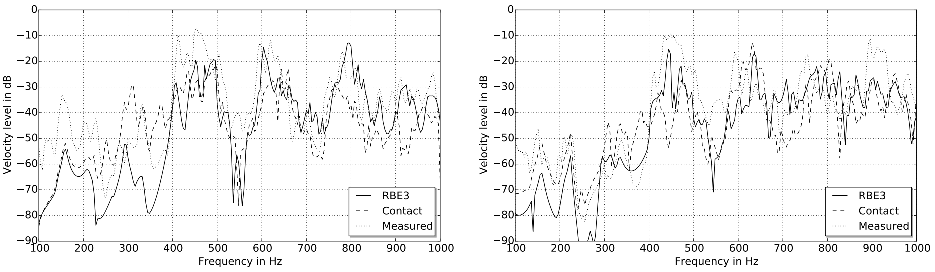

(a) Acc301 (b) Acc701

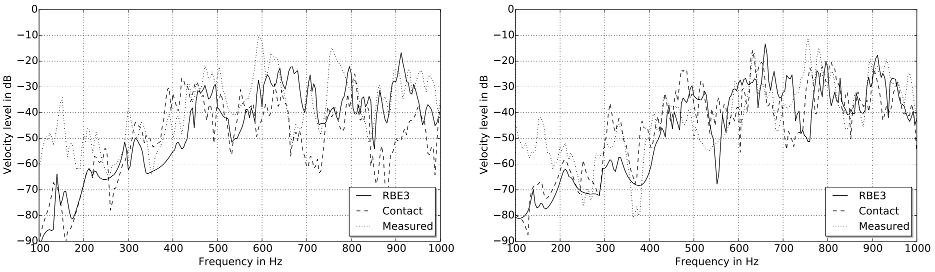

(c) Acc801 (d) Acc901

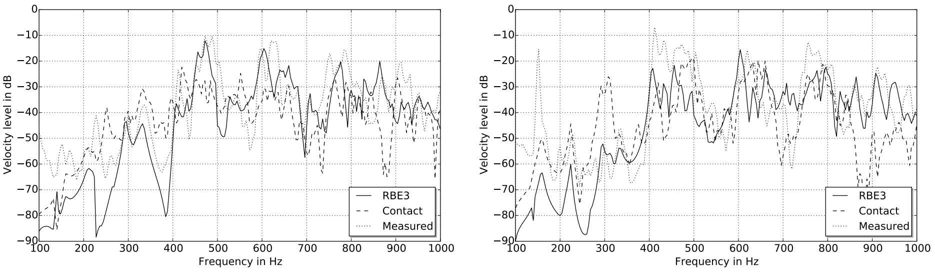

(e) Acc1201R (f) Acc1201L

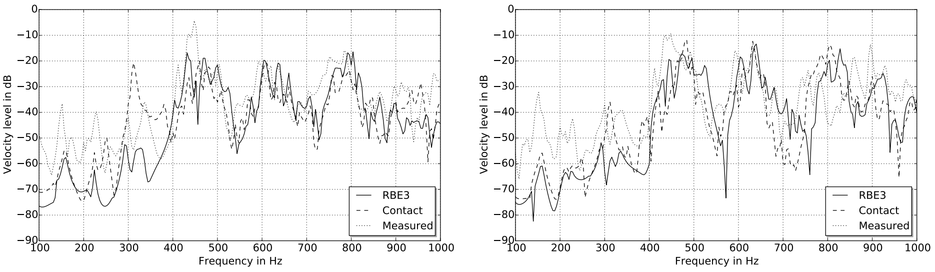

(g) Acc4501R (h) Acc4501L

Figure B.7.: Velocity level transfer function comparison plots for the rear muffler for all accelerometers.

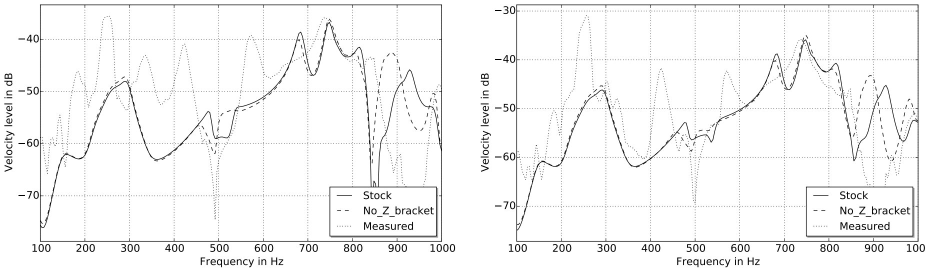

(a) Acc01 (b) Acc02

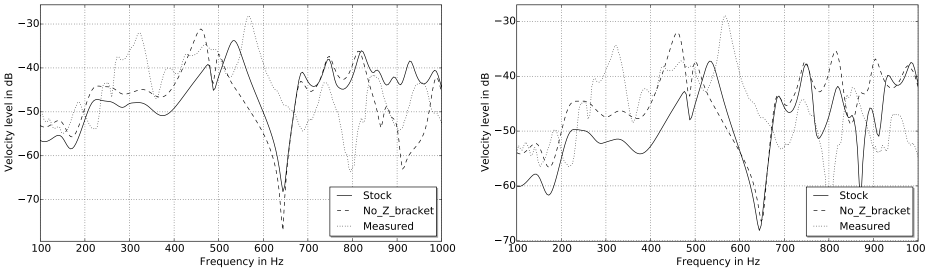

(c) Acc03 (d) Acc04

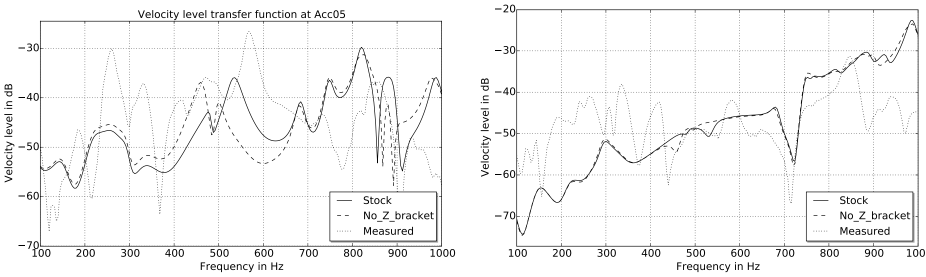

(e) Acc05 (f) Acc06

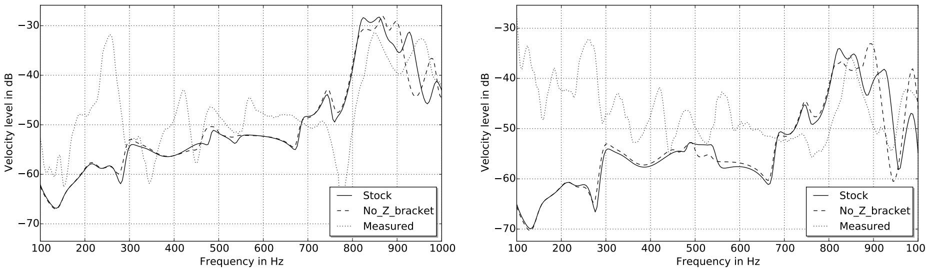

(g) Acc07 (h) Acc08

Figure B.8.: Velocity level transfer function comparison plots for the front muffler for all accelerometers.

B.3. Engine running condition measurement results

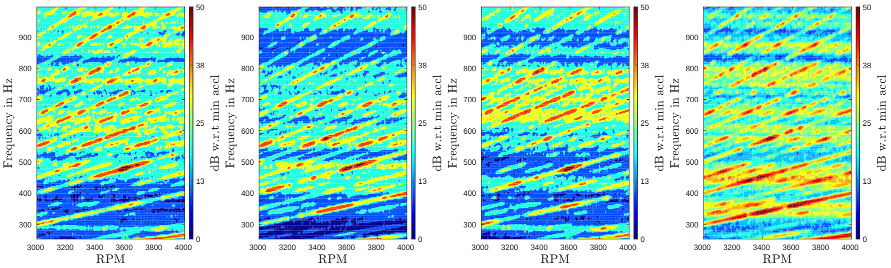

(a) Acc301 (b) Acc801 (c) Acc1201L (d) Acc1201R

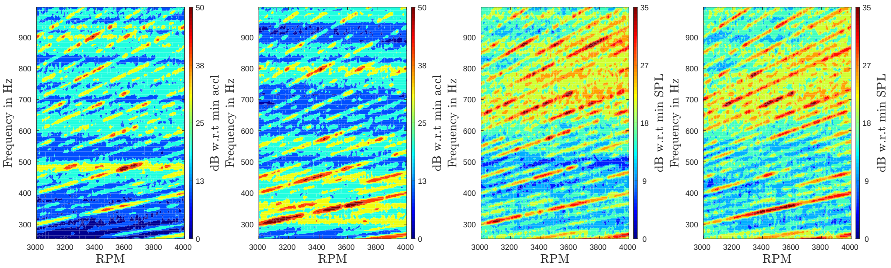

(e) AccH07 (f) AccH08 (g) Exh518 (h) Exh519

Figure B.9.: 1/3 POT, 3000-4000 RPM

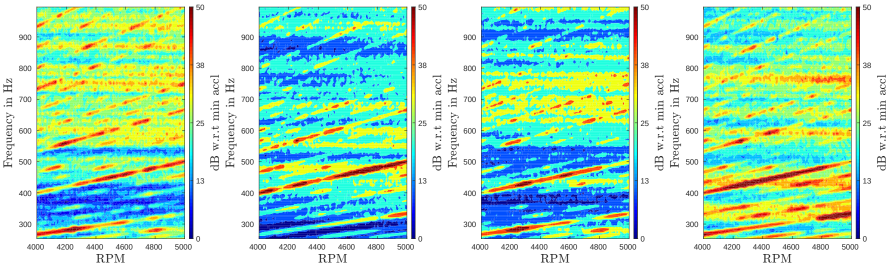

(a) Acc301 (b) Acc801 (c) Acc1201L (d) Acc1201R

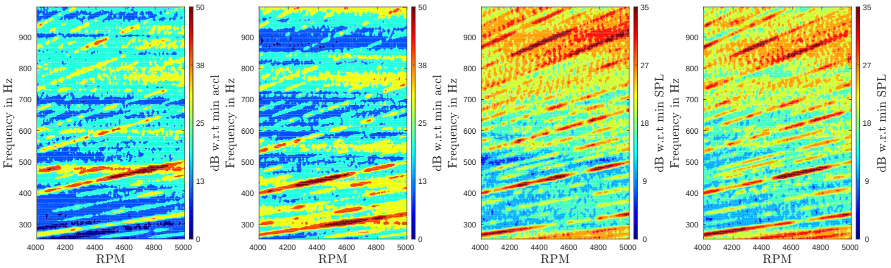

(e) AccH07 (f) AccH08 (g) Exh518 (h) Exh519

Figure B.10.: 1/3 POT, 4000-5000 RPM

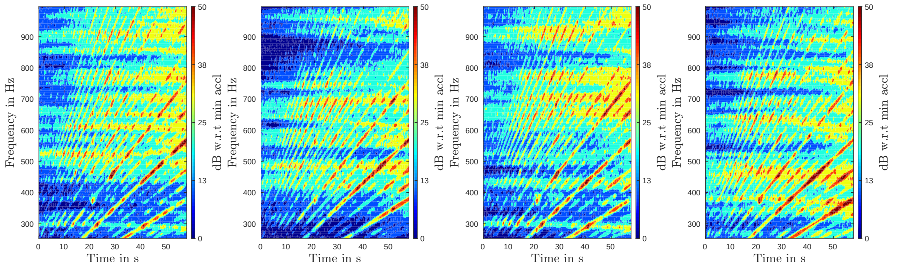

(a) Acc301 (b) Acc801 (c) Acc1201L (d) Acc1201R

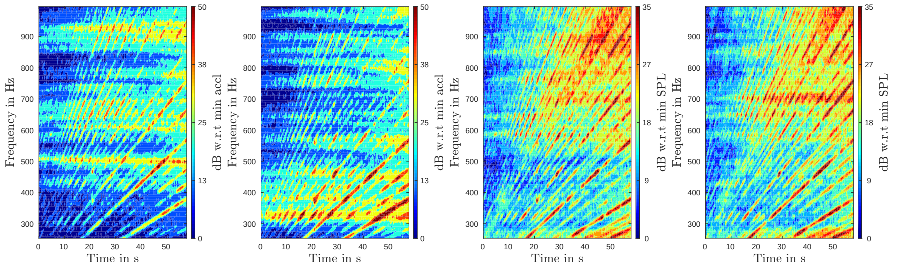

(e) AccH07 (f) AccH08 (g) Exh518 (h) Exh519

Figure B.11.: 1/3 POT, Full RPM

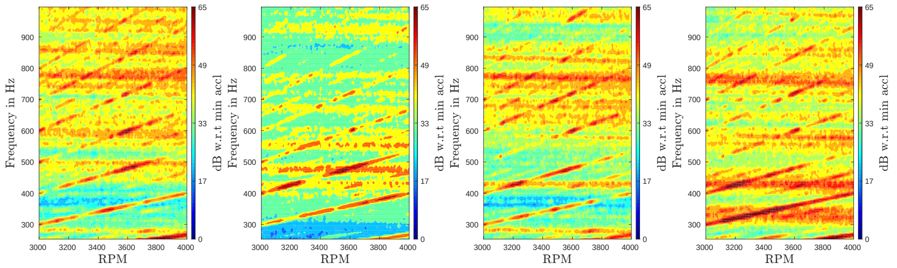

(a) Acc301 (b) Acc801 (c) Acc1201L (d) Acc1201R

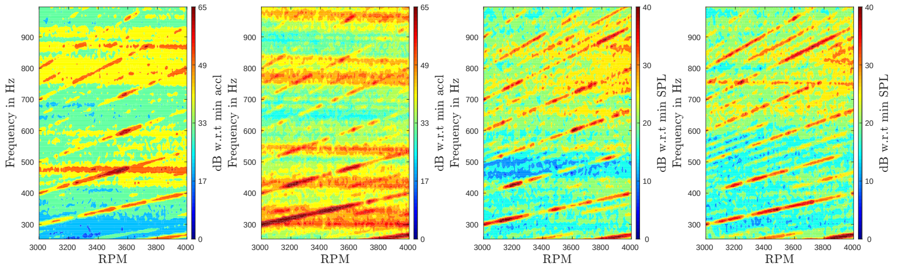

(e) AccH07 (f) AccH08 (g) Exh518 (h) Exh519

Figure B.12.: 2/3 POT, 3000-4000 RPM

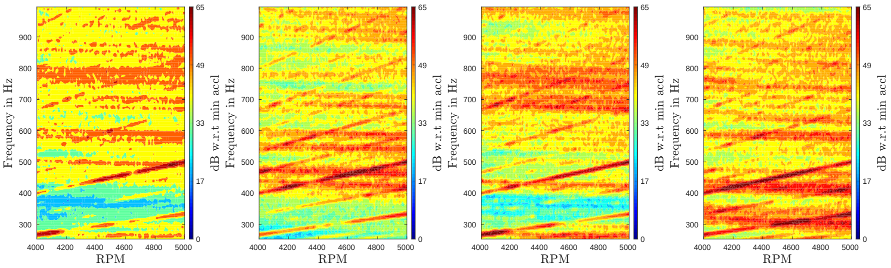

(a) Acc301 (b) Acc801 (c) Acc1201L (d) Acc1201R

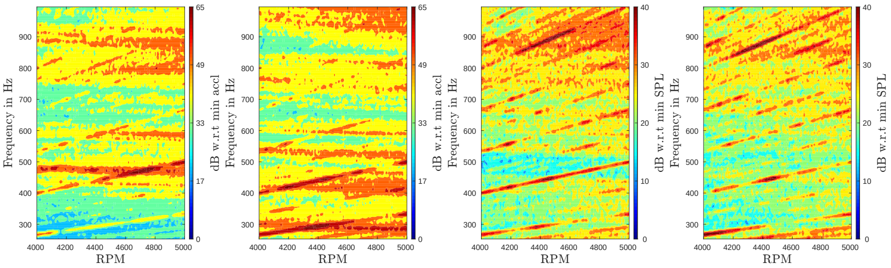

(e) AccH07 (f) AccH08 (g) Exh518 (h) Exh519

Figure B.13.: $^{2}/_{3}$ POT, 4000-5000 RPM

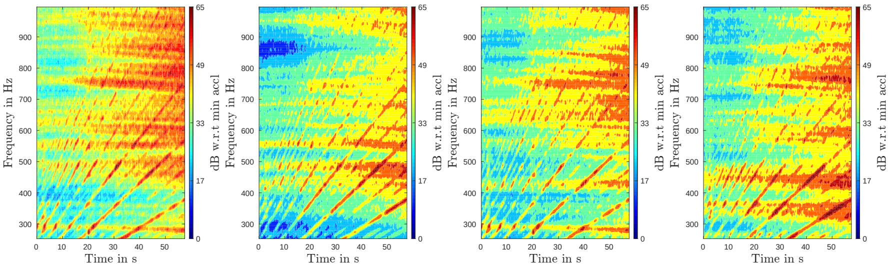

(a) Acc301 (b) Acc801 (c) Acc1201L (d) Acc1201R

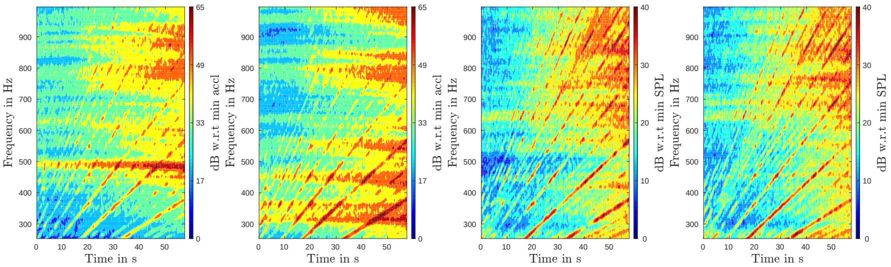

(e) AccH07 (f) AccH08 (g) Exh518 (h) Exh519

Figure B.14.: $^{2}/_{3}$ POT, Full RPM

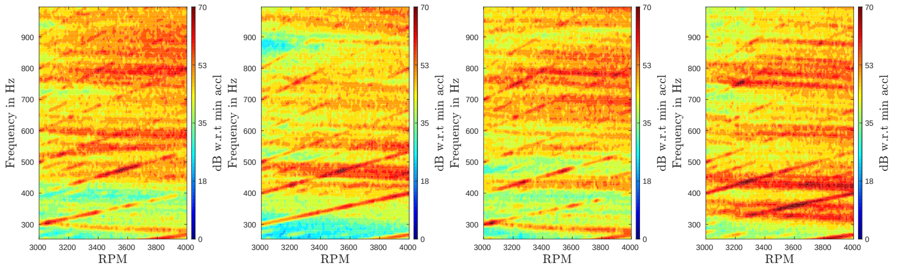

(a) Acc301 (b) Acc801 (c) Acc1201L (d) Acc1201R

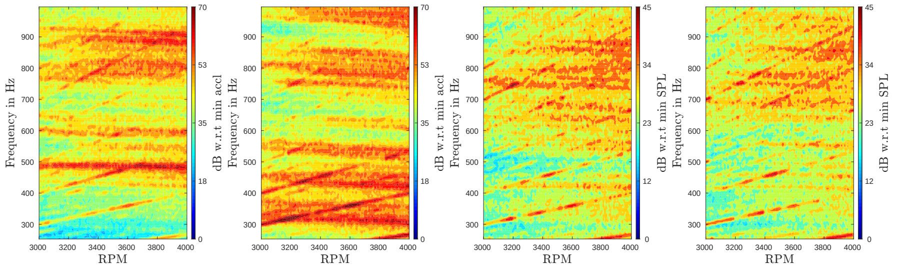

(e) AccH07 (f) AccH08 (g) Exh518 (h) Exh519

Figure B.15.: WOT, 3000-4000 RPM

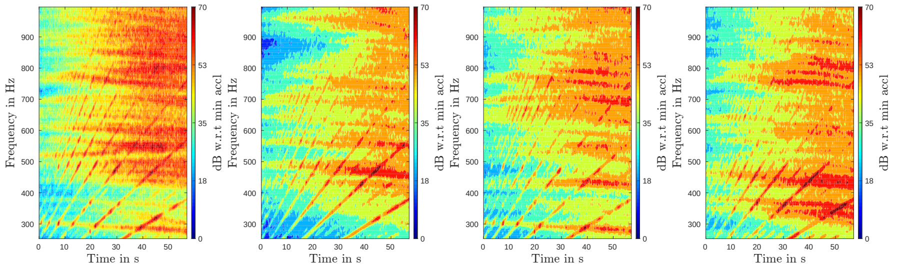

(a) Acc301 (b) Acc801 (c) Acc1201L (d) Acc1201R

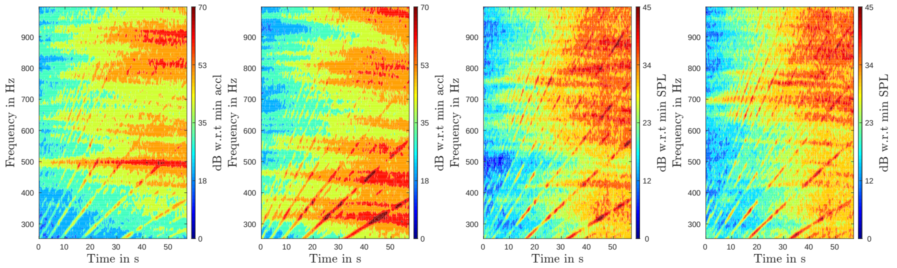

(e) AccH07 (f) AccH08 (g) Exh518 (h) Exh519

Figure B.16.: WOT, Full RPM

Bibliography

[1] J. Brand, P. Garcia, and D. Wiemeler. Surface radiated noise of exhaust systems - calculation and optimization with cae. *SAE Technical Paper*, 2004. doi: 10.4271/2004-01-0407.

[2] T. Narayana and M. Munjal. Computational prediction and measurement of break-out noise of mufflers. *SAE Technical Paper*, 2007. doi: 10.4271/2007-26-040.

[3] C. Yang, J. George, T. Wahl, and H. Jin. Predicting shell vibration and implosion issues in automotive muffler design. *SAE Technical Paper*, 2009. doi: 10.4271/2009-01-2038.

[4] M. Junge, D. Brunner, N. Walz, and L. Gaul. Simulative and experimental investigations on pressure-induced structural vibrations of a rear muffler. *The Journal of the Acoustical Society of America*, 128:2782–2791, 2010. doi: 10.1121/1.3466874.

[5] *Actran 16 Users Guide - Volume 1. Installation, Operations, Theory and Utilities.* Free Field Technologies, a division of MSC Software, Belgium, October 2015.

[6] *CALFEM, A Finite Element Toolbox.* Division of Structural Mechanics, LTH, Lund, Sweden, 3.4 edition, October 2004. URL `github.com/CALFEM/calfem-matlab`.

[7] G. Sandberg and R. Ohayon. *Computational Aspects of Structural Acoustics and Vibration*, volume 505 of *CISM Courses and Lectures.* Springer, Wien and New York, 2009. doi: 10.1007/978-3-211-89651-8.

[8] J.F. Allard. *Propagation of Sound in Porous Media: Modelling Sound Absorbing Materials.* Elsevier Applied Science. Elsevier Science Publishers, London and New York, 1993. doi: 10.1007/978-94-011-1866-8.

[9] A. F. Seybert and D. F. Ross. Experimental determination of acoustic properties using a two-microphone random-excitation technique. *The Journal of the Acoustical Society of America*, 61:1362–1370, 1977. doi: 10.1121/1.381403.

[10] H. Bodén and M. Åbom. Influence of errors on the two-microphone method for measuring acoustic properties in ducts. *The Journal of the Acoustical Society of America*, 79:541–549, 1986. doi: 10.1121/1.393542.

[11] J.H Lee, J. Kim, and V. Kothamasu. Analysis and experimental study of the mean flow effect on the sound transmission through a cylindrical shell of an automobile muffler. *SAE Technical Paper*, 2001. doi: 10.4271/2001-01-1517.

[12] D. Kammer. Optimal sensor placement for modal identification using system-realization methods. *Journal of Guidance, Control, and Dynamics*, 19(3):729–731, 1996. doi: 10.2514/3.21688.

[13] T. Abrahamsson. Calibration of fe models using parametrized models and test data, 2013. URL `se.mathworks.com/matlabcentral/fileexchange/44317-femcali`.

[14] *ANSA Users Guide.* BETA CAE Systems, Thessaloniki, Greece.

[15] *MSC Nastran 2016 - Quick Reference Guide.* MSC Software, Newport Beach, California, April 2016.

[16] S. Mattson, D. Labyak, J. Pruetz, and T. Connelly. Prediction of Muffler Insertion Loss by a Hybrid FE Acoustic-SEA model. *SAE Int. J. Passeng. Cars-Mech. Syst.*, 2(1):1323–1329, 2009. doi: 10.4271/2009-01-2042.

[17] S. Marburg and B. Nolte. *Computational Acoustics of Noise Propagation in Fluids - Finite and Boundary Element Methods.* Springer, Verlag Berlin Heidelberg, 1st edition, 2008. doi: 10.1007/978-3-540-77448-8.

[18] D.M Riffe. Separation of variables in cylindrical coordinates. Lecture Notes in Wave Phenomena, Physics 3750, Utah State University, March 2013.

[19] S.S. Rao. *Mechanical Vibrations.* Prentice Hall, Upper Saddle River, NJ 07458, 5th edition, 2011.